Parameter Estimation for Physics-Based Electrochemical Model Parameterization and Degradation Tracking

Karthik Subbu Mayilvahanan

Submitted in partial fulfillment of the
requirements for the degree of
Doctor of Philosophy
under the Executive Committee
of the Graduate School of Arts and Sciences

COLUMBIA UNIVERSITY

2022

Abstract

Parameter Estimation for Physics-Based Electrochemical Model Parameterization and Degradation Tracking

Karthik Subbu Mayilvahanan

Physics-based electrochemical models are useful tools for optimizing battery cell and material design, managing battery use, and understanding physical phenomena, all of which are key in enabling adoption of batteries to electrify transportation, grid storage, and other high carbon emission industries. Fitting these models to experiments can be a useful approach to determine missing parameters that may be difficult to identify experimentally. In this dissertation, two use cases of this approach — model parameterization and degradation tracking — are explored.

An introduction to the need for batteries and an overview of challenges in the field is presented in Chapter 1. Of these challenges, those that can be addressed by battery modeling solutions are discussed in further detail. An overview of continuum level physics-based electrochemical models is provided, and the case is made for the utility of parameter estimation.

In Chapter 2, an extension of a published model for lithium trivandate cathodes for lithium-ion batteries is outlined. While the original model described (de)lithiation and phase change in the cathode, the new model describes simultaneous lithiation of the original phase, lithiation of the newly formed phase, and phase change. Parameters associated with the thermodynamics and kinetics of charge transfer and lithium transport in the second phase are estimated directly from experimental data. This study serves as an example of using the model fitting approach to determine model parameters that would be difficult to isolate and measure experimentally.

Chapter 3 explores a similar concept of model parameterization, this time focusing on the electrode tortuosity. Tortuosity is a hard to quantify parameter that describes how tortuous of a path lithium ions must travel through an electrode or separator. Because there are several experimental measurement techniques suggested in the literature that do not always provide consistent results, an approach to fit the tortuosity to a standard rate capability experiment is introduced. The Bayesian approach returns uncertainties in tortuosity estimates, which can be used to predict a range of

outcomes for high-rate performance. Covariance between parameters in the model and their impact on uncertainties in tortuosity is also discussed.

Beyond model parameterization, parameter estimation can also be useful in the context of tracking degradation by fitting a physics-based model over the course of cycling and interpreting the evolution of the parameter estimates. In Chapter 4, this idea is explored by fitting the model developed in Chapter 2 to cycling of an LVO cell. Parameter estimates are interpreted in conjunction with traditional tear down and electrochemical analysis to identify root causes of degradation for this cell.

Depending on the number of parameters being simultaneously estimated, it can become an onerous task to fit model parameters, especially if the physics-based model cannot easily be enclosed in an efficient optimization algorithm. To this end, machine learning (ML) can be useful. If a ML model is trained offline on synthetic data generated by a battery model to map the observable electrochemical data to parameters in the battery model, the ML model can be deployed to estimate parameters from experiment. These models can be referred to as inverse ML models, since they perform the inverse task of a "forward" physics based model.

The procedure described above is implemented in Chapter 5. Interpretable ML models are trained on published synthetic data generated by equivalent circuit models. Pseudo-OCV (slow charge, C/25) full cell voltage curves are passed into the inverse ML models to estimate degradation modes in lithium ion batteries and classify which electrode limits cell capacity. These models are useful in diagnosing the state of the battery at any given time. Accuracies of the inverse ML models are evaluated on independent test sets also composed of synthetic data and are published to benchmark future diagnostic studies. The insights derived from the trained ML models in terms of which features in the full cell voltage curves are predictive of the degradation modes are compared to expert insights.

In chapter 6, the robustness of the inverse ML approach towards model-experiment disagreement is probed. If the experiment does not directly map onto the protocol used to generate the synthetic training data for the ML model, or if the model itself is inherently a poor descriptor of experiment, the inverse ML model will inevitably return inaccurate estimates. In this chapter, a feed forward neural network (NN) is employed as the inverse ML model. In two case studies of model-experiment disagreement, the NN returns biased parameter estimates. A simple data augmentation procedure is introduced to mitigate these biases.

Chapter 7 ties together the understanding developed in the previous chapters by applying more robust neural networks to estimate parameters for LVO cells cycled at different rates. This study demonstrates how to interpret parameter estimates in conjunction with cycling data to gain mechanistic insight into degradation. A complex map of coupled degradation hypotheses is reduced to a smaller subset of possible mechanisms for two exemplary LVO cells, and parameter estimates for a larger set of LVO cells are discussed. The framework presented in this study synergistically combines experiment, physics-based modeling, and machine learning to better understand degradation phenomena.

Table of Contents

List of Figures

List of Tables

Acknowledgements

First and foremost, I'd like to thank my adviser Dr. Alan West. Dr. West struck the perfect balance between structure and freedom in my PhD. In the first year, when I lacked experience and was in the dog days of model development, Dr. West guided me through the process until I was able to handle it myself. As the years went on and I built my own confidence not only in modeling but also in thinking about where I could make a contribution to the field, Dr. West afforded me the space to explore new techniques and integrate them into my work. My passing interest in machine learning in my second year became a core part of my thesis due to his open mindedness.

Next, I'd like to thank my colleagues in the West group and the 10th floor office. Dr. Nick Brady developed some of the original models that I built on and used throughout my PhD, helped train me in my first year, and instilled the value of automating work flows that paid dividends later in my PhD. I also owe so much to Dr. Zeyu Hui. From talking through ideas to debugging models to rederiving dilute and concentrated solution theory, learning from and alongside you sharpened my understanding of the field and made me a better scientist. I'd like to thank other group members, especially Jon, John, Kedi, and Jwal for the discussions and collaboration. To the rest of the battery researchers in the 10th floor office, it was a privilege to sit next to you and learn about your approach to critical challenges in our field.

I owe a great deal to the collaborators whom I had the opportunity to work with over the past couple of years. Dr. Amy Marschilok, Dr. Esther Takeuchi, and Dr. Lei Wang were always a pleasure to work with, and I learned so much from our discussions. The nexus of modeling and experiment is where some of the most interesting and impactful work can happen, and I had the privilege of operating in that space for my entire PhD.

I want to also thank our department staff, especially Kathy, Ariel, and Serxhio for making sure I was on track and helping me get the resources I needed to proceed with both academics and research.

Outside of my professional life at Columbia, I want to extend the sincerest thank you to all the friends that made my time here unforgettable. To Neal, Emma, Do Young, and Richard, you are

the best and I feel very lucky to have joined the program with you all. I will miss the lunches, happy hours, mid-week trivia, gym sessions, and nights out dearly. To my friends in the office, both those who are there currently (Drew, Will, Daniela, Chris, Hansen, Kevin) and those who were there previously (Will, Ryan, Alison, Han, Mateo, Rob), thanks for making that office a fun place to come to work (or not work) every day. To Shiva, thanks for serving as a bit of home away from home. To Akila, Ram, and Rajiv, thanks for keeping the group chat active and giving me a laugh, sometimes when I needed it the most. To Jenn, Maya, and Chris, I'm thankful I got to bring some familiarity with me across the country. I appreciate your friendship and support over the years. Here's to four doctors, only one of whom can actually help people.

Finally, I want to acknowledge my family and the role they have played in preparing me for success. To my brother Sarvesh, a humongous thank you. Despite being younger, Sarvesh helped me take my peripheral interest in machine learning and actually apply it in a useful way to my research. I very literally could not have completed this PhD without you. Thanks for your help and support, but more importantly your friendship and companionship. I want to shout out my dad, to whom I credit a natural curiosity and a feeling of responsibility to be well informed, both of which were essential to my success in graduate school. Thanks Appa for showing me the value of engaging outside of work, and the importance of laughter amidst the chaos. Lastly, I need to credit my mom for passing on to me a fraction of her unrelenting work ethic and mental toughness. These attributes are what allowed me to put my head down and push through when things weren't going as smoothly as I would have liked. Thanks Amma. This dissertation is dedicated to the three of you.

Chapter 1

Introduction to Batteries and Physics-based Battery Models

1.1 Batteries: Motivation and Challenges

As global energy usage increases amidst a pressing need to curtail global temperature increase and avoid the consequent climate effects, the need to transition energy consumption from high carbon emission sources to clean, renewable sources is more important than ever. Though energy consumption from renewable sources has reduced the United States' dependence on coal, petroleum and natural gas remain the dominate energy sources.[1] According to the Energy Information Agency's 2022 Annual Energy Outlook, the three largest energy consuming sectors in the United States in 2021 were the electric power, transportation, and industrial sectors at 37, 25, and 22 quadrillion Btus respectively. Though the transportation sector was the second highest in energy consumption, it was the largest sector in carbon dioxide emissions, emitting 1.75 billion metric tons of carbon dioxide annually.[1]

The transition towards renewable energy sources like wind and solar does not come without challenges. One notable challenge is their intermittency, or their inability to reliably produce energy at all times. To this end, they must be paired with energy storage solutions to become more widely adopted. A range of technologies exist for energy storage, but lithium ion batteries have experienced the most market penetration due to rapidly falling system-level costs.[2]

Though grid storage is and will increasingly become a target market for batteries, the demand for batteries is currently being driven by the transportation sector.[2] The EIA projects a tripling of electric vehicle sales in the United States by 2050.[1] Batteries for electric vehicles have different requirements than those for grid storage applications, including energy density (which translates to vehicle range), cost, safety, ability to fast charge, power capability, and extended lifetime.[3,4]

Li-ion batteries consist of a graphite anode, a liquid electrolyte, and a range of cathode materials, including lithium cobalt oxide (LCO), lithium nickel manganese cobalt oxide (NMC), lithium nickel cobalt aluminum oxide (NCA), lithium manganese oxide (LMO), and lithium iron phosphate (LFP).[4–6] These chemistries correspond to different trade offs in energy density, power density, safety, cost, and lifetime.

For more mature Li-ion batteries, while some optimization can still be done to improve energy and power density and reduce cost on the cell and pack levels, performance and cost appear to be plateuing.[2,4] An outstanding challenge and active area of research and development for Li-ion batteries is the diagnosis and prognosis of degradation. The ability to accurately estimate the state of a battery, predict its lifetime, and manage its use to extend its lifetime is of great interest to automotive manufacturers especially, since it can be difficult to reproduce the wide range of long-time stresses that electric vehicle batteries experience in the lab.[7]

In terms of advancing the materials systems for batteries, in the near term, there is a push towards removing cobalt from cathodes in favor of nickel for both performance and materials availability related reasons.[3,4] For batteries with these cathodes, optimizing the trade off between energy density and lifetime is the critical challenge. In a further outlook, advanced anodes like silicon or lithium metal and advanced cathodes like sulfur can help achieve step changes in energy density.[6,8–10] Advanced electrolytes like solid state electrolytes have the potential to resolve major safety issues in current lithium ion batteries.[4,5,11] In an even further outlook, beyond-lithium systems like sodium ion batteries could become critical if and when the global lithium supply chain is strained.[9,12] For all of these systems, fundamental understanding of materials and interfaces and their evolution over use are necessary to realize their full potential.

1.2 Battery Modeling

Models used for battery research and development span length scales from angstroms to meters. At the smallest length scale, atomistic models that employ density functional theory are useful in understanding the relationship between molecular structure and material properties. On the other end of the spectrum, technoeconomic models are useful in comparing candidate technologies on a systems level.[13] The models of interest in this dissertation are continuum level models that describe physics on the particle and cell level.

1.2.1 Continuum Level Physics-Based Electrochemical Models

The two most commonly used continuum level physics-based models are the pseudo-2D (P2D) model and the single particle model (SPM). The P2D model represents each electrode as a one dimensional array of active material particles on the axis passing through the cell stack (through-plane). The model can simulate evolution of concentration and potential profiles in the solid and the electrolyte along this axis, sometimes referred to as the "electrode scale". Intercalated lithium concentration distributions within each of the representative particles ("particle scale") are solved for simultaneously. The two length scales are coupled via local electrochemical reaction rates.[14] The single particle model simplifies the P2D model by assuming that there are no electrode scale concentration and potential gradients, which means each electrode need only be represented by one particle.[15,16] Modifications have been made to the SPM to include an analytical solution to the electrolyte dynamics that are decoupled from the particle scale, referred to in the literature as SPMe.[17–19]

In reality, the P2D model itself is a simplification of complex heterogeneity in cells in both the through plane and in plane directions. Strategies exist to account for in plane heterogeneity. The P2D or SPMe models can be extended to solve the 1D problem at multiple locations in the plane of the current collectors.[18] Alternatively, these equations can be solved in more realistic representations of the electrodes derived from x-ray tomography at a much higher computational cost.[20,21] These methods will not be of interest in this work. At the moderately high charging and discharging currents that are of relevance to electric vehicles (and therefore used in most of this study), heterogeneity due to concentration distributions in the through plane direction should dominate the effects of any in plane heterogeneity that exists in the cells. Much of this work focuses on estimating parameters from data as well. Since parameters in continuum models represent effective properties, in many cases the effects of in plane heterogeneity can be lumped into effective properties. Finally, it was determined that more complex representations of the electrodes were not worth the computational cost required.

1.2.2 Use cases for Physics-based Electrochemical Models

Fundamentally, physics-based models are useful tools to explore different hypotheses for the governing physics of a materials or electrochemical system. Many have extended the original P2D and SPM models to couple the electrochemical model to thermal[16,22,23] and mechanical behavior,[17,23,24] both of which are known to affect single-cycle performance as well as battery lifetime.

Perhaps the most obvious application of a validated model is to optimize battery design, either on the material or cell level. Several studies, including Chapter 2 in this dissertation, have explored optimizing porosity, thickness, and loading of an electrode to maximize a performance metric like energy or power density[14,25–33] Others have explored optimizing advanced electrode architectures like aligned channels or graded porosity electrodes.[34,35]

Battery models are also useful in control and management. While most onboard control applications use equivalent circuit models as simplified representations of batteries, there has been increasing interest in management strategies that incorporate physics-based electrochemical models as "digital twins".[36–39] For instance, many have used electrochemical models to optimize charging times to achieve extreme fast charge in Li-ion batteries.[38,40,41] Insights from physics-based models can be used to predict the onset of Li plating and thus avoid this phenomena, which is known to be detrimental to the lifetime of the battery. In less applied but more fundamental studies where experimental resources may be limited, these models can similarly be used to design experiments for the most efficient use of resources.[42,43]

Finally, many have explored simulating degradation phenomena in batteries.[44–49] Physics-based degradation models range from implementations of single degradation mechanisms assumed to be dominant under a specific set of conditions to highly coupled implementations that attempt to incorporate feedback loops between mechanisms. Mechanisms are added to P2D or SPM type models, sometimes coupled with thermal and/or mechanical descriptions as well. These models can explore how stress factors like time, temperature, current, and voltage affect the degradation trajectory of a cell. The largest challenge in the use of degradation models that explicitly define mechanisms is parameterizing the rates of the different mechanisms and properly defining the coupling between them.

1.2.3 Parameterizing Physics-based Electrochemical Models

Parameterization of physics-based models can be challenging. Geometric parameters like thicknesses are typically easy to measure, and some chemical properties like compositions and densities are known beforehand. The remaining parameters, some of which may be modeled as dependent on the electrode state of charge, must be measured or estimated.

For some properties there is consensus in the community on the measurement technique. For example, the electrode open-circuit potentials as functions of state of charge are typically measured with a very slow charge or discharge, or via a galvanostatic intermittent titration technique (GITT).[50] On the other hand, for some parameters, there are a variety of experimental procedures in the literature. For instance, several procedures have been explored to estimate the electrode tortuosity (described in further detail in Chapter 3). Even if there is agreement in the community on an experimental measurement procedure, the parameters extracted from independent experiments are not necessarily predictive of electrochemical performance. This could indicate either the independently measured parameter is wrong, or that the model structure itself is incorrect.

In this dissertation, an alternative perspective on parameterization of physics-based electrochemical models is adopted. For parameters that are difficult to measure independently, are not predictive when measured independently, or are not identifiable, we opt to fit the parameters directly to electrochemical data. Models fit to electrochemical data are validated on independent measurements, and tend to be more reliably predictive. Throughout the dissertation, special attention is given to quantifying uncertainty in parameter estimates as well. Uncertainties in parameters allow for model parameterization while acknowledging the model may be inherently imperfect and can be used to predict a range of outcomes instead of a single prediction. Examples are provided of the interpretation of these parameter estimates and how they can be used to better characterize electrodes to optimize performance and understand degradation phenomena.

Chapter 2

Design Principles to Govern Electrode Fabrication for the Lithium Trivanadate Cathode*

---

*This chapter has been published: Karthik S. Mayilvahanan, Nicholas W. Brady, Alison H. McCarthy, Lei Wang, Kenneth J. Takeuchi, Amy C. Marschilok, Esther S. Takeuchi, Alan C. West, "Design Principles to Govern Electrode Fabrication for the Lithium Trivanadate Cathode," *Journal of the Electrochemical Society.*, vol. 167, no. 10, p. 100503, May. 2020.
The thesis writer's contribution was physics-based model analysis, based off of contributions from Nicholas Brady, and writing. The electrochemical observations were provided by Alison McCarthy from the Marschilok-Takeuchi Research Group at Stony Brook University.

2.1 Introduction

Lithium ion batteries (LIBs) have generated great interest as energy storage solutions for high power density and high energy density applications, such as portable electronics and electric vehicles.[9] Vanadium based materials are appealing active materials for a cathode in a lithium based battery due to the ability for multiple electron transfers within a desirable voltage range.[51] Lithium trivanadate ($Li_xV_3O_8$) garners interest as a candidate for a mid-voltage cathode in lithium ion batteries because of its high theoretical capacity (362 mAh/g), its good rate capability, and the abundance of its raw materials.[52–54]

The synthesized $Li_{1.1}V_3O_8$ is composed of layers of V_3O_8 sheets separated by Li ions in the interlayer positions.[55] The cathode begins in this layered α-phase ($Li_{1.1}V_3O_8$) and is lithiated up to $Li_{2.5}V_3O_8$, at which point the α-phase is saturated and phase change occurs to form the rock-salt like β-phase ($Li_4V_3O_8$).[52,56] This phase change corresponds to the extended plateau at 2.5 V. At lower potentials, at the end of discharge, the β-phase can be lithiated up to $Li_5V_3O_8$, at which point the potential drops off to the cutoff voltage.[57,58]

Since the structural stability of $Li_{1.1}V_3O_8$ plays an important role in the resulting electrochemistry, the understanding of the structural evolution and reaction mechanisms has been a goal of many prior reports on this topic.[55,58,59] Controlling the synthesis of $Li_{1.1}V_3O_8$ has proved promising in improving electrochemical performance of an electrode. Specifically, sol-gel-based syntheses have delivered higher capacities at different annealing temperatures than those achieved by analogue materials derived from hydrothermal synthesis.[55,60,61] With respect to the annealing temperatures, although higher initial capacities were delivered by the materials annealed at lower temperatures (300 °C), more stable capacities were maintained over extended cycling using materials annealed at higher temperature (500 °C).[59,62] To probe the phase changes and reaction mechanisms of $Li_{1.1}V_3O_8$ as a cathode material, many different techniques have been implemented. Recently, in situ angle dispersive X-ray diffraction (ADXRD) was able to discern differences in β-phase formation between different synthesis techniques.[58] X-ray and neutron refinement have been performed on chemically lithiated samples to determine the Li-rich α-phase along with the defected rock salt β-phase at $Li_{2.7}V_3O_8$ and $Li_{4.8}V_3O_8$, respectively.[63] In situ XRD coupled with DFT calculations have also been used to further understand the structural evolution of the material throughout (dis)charge processes.[55] Synchrotron based energy dispersive X-ray diffraction (EDXRD) was used to investigate the spatial phase distribution of the (de)lithiation in situ and operando.[62] To gain greater insights into the phase evolution of $Li_{1.1}V_3O_8$, continuum modeling of the $Li_{1.1}V_3O_8$ cathode has been utilized in this study, based on experimental data from different electrode fabrication techniques.

A coupled electrode-scale and crystal-scale continuum model for the trivanadate cathode has been reported.[64] The model includes a single-phase insertion and phase change, assuming dominant transport in the [001] direction based on the crystal dimensions.16 This model shows good agreement for the first discharge of a trivanadate cathode down to 2.4 V, but cannot simulate the physics at lower voltages because lithiation of the β-phase is neglected. The contribution of lithiation of the β-phase is not negligible, especially at slower specific currents.8 In addition, comparison of the voltage profiles over the course of cycling show that lithiation of the β-phase appears to become increasingly important over the course of cycling.9 Here, the previously published model has been extended to include insertion of lithium into the second phase, enabling electrochemical behavior of the cathode for the full depth of discharge to be simulated.

The extended model is used in conjunction with published operando Energy-Dispersive X-ray Diffraction (EDXRD) measurements and electrochemical measurements to understand electrode-scale transport resistances in a thick electrode.[42] The operando EDXRD measurements collect diffraction patterns in 20 μm increments along the length of the cathode as the cell is (dis)charged. By tracking peak locations at different depths of discharge, the lithiation of the cathode has been confirmed to initiate closer to the Li anode and then propagate through the electrode, while the delithiation appears to be a homogeneous phase transition throughout the cathode.[42,62] Simulated profiles for the volume fraction of the β-phase are validated by comparing the simulated and experimental propagation of the phase change front across the length of the electrode during its full depth of discharge.

Building on the increasingly thorough understanding of the multi-scale physics of the lithium trivanadate cathode, there is an interest in developing fabrication methods to further increase performance. The electrode is optimized for cell volumetric energy ($Wh\ L^{-1}$) and cell areal energy density (Wh m-2), with the intention that results can guide electrode fabrication of lithium trivanadate cathodes. While the cell volumetric energy density is important for space-limited applications like portable electronics and electric vehicles,[6,10] the areal energy density could be more relevant for cost-driven applications where balance of cell components like current collectors, separators, and casings make up a significant portion of the cost,[65,66] and is therefore considered alongside the volumetric energy density. Newman and collaborators have demonstrated the utility of mathematical models to optimize specific power and specific energy by tuning electrode thicknesses and porosities.[14,25–27] While these studies involved changing one design parameter at a time and assessing the impact on performance, Subramanian et. al. performed simultaneous optimization of anode and cathode thicknesses and porosities to improve energy density.[29] Subsequent model-based studies have optimized electrode thickness and porosity for a range of cathodes, including LiMn2O4,[14] LiNiMnCoO2,[30] LiNiCoAlO2,[67] and LiFePO4.[27,28] Yet others have considered optimal distributions of porosity in thick electrodes.[34]

In all of the aforementioned optimization studies, the focus is on optimizing design parameters for ionic transport, and sufficient electronic conductivity is assumed. Here, in addition to extending the published model to account for lithiation of the β-phase, a functional dependence of the electronic conductivity on the volume fraction of conductive additive in the electrode is modeled. Previously published models that have included a more detailed dependence of electronic conductivity include potential dependent conductivity for a semiconducting polymeric binder used with LiFePO4,[68] and conductivity that accounts for spherical particle to particle interactions between LiCoO2 and carbon black.[69] In this study, the electronic conductivity of electrodes with multi-walled nanotubes (MWNTs) as conductive additives is modeled based on percolation theory, and a three-parameter optimization is performed, considering porosity and thickness of the cathode, as well as the volume fraction of the conductive additive. This analysis leverages porous electrode theory, considering both ionic and electronic transport, with the goal of establishing a quantitative understanding of the tradeoffs between the two in the context of the lithium trivanadate cathode. Efforts are also made to describe the sensitivity of performance to the three design parameters. Finally, because formation of the β-phase has been shown to contribute to capacity fade,[58,70] an optimization is conducted with the constraint of avoiding phase transition in the electrode.

2.2 Experimental

Lithium Vanadate (LiV_3O_8) was synthesized through a previously reported sol-gel approach.9 Briefly, V2O5 and LiOH·H2O in a stoichiometric ratio of Li:V = 1.1:3 were stirred under nitrogen atmosphere in aqueous solution at 50°C for 24 h. The resultant material was dried and annealed at 500°C to achieve the final product. To prepare the pellet electrodes for EDXRD measurements, the LiV3O8 material was mixed with carbon and graphite in a ratio of 90:5:5. The mixture was then pressed into a pellet with a thickness of 500-600μm. The 3D porous electrodes for galvanostatic rate capability test were comprised of carbon nanotubes (CNTs) and LiV3O8, in a mass ratio of 3:7. The resulting porous electrodes had thicknesses ranging from 250 to 500 μm, with a corresponding LVO loading mass of 5 to 16 mg/cm^2. Thicknesses were additionally reduced for certain electrodes by pressing at 6000 psi. In an argon-filled glove box, coin type cells were constructed with the prepared electrodes as the cathode, Li metal as the anode, and polypropylene separator. For both electrode configurations 1 M LiPF6 in ethylene carbonate/ dimethyl carbonate (at a 3:7 volume ratio) was used as the electrolyte. The pellet electrode cells were discharged at a current rate of C/18 on a Maccor Cycler while performing operando EDXRD measurements conducted at the Advanced Photon Light Source at Argon National Laboratory on Beamline 6-BM-B. This discharge rate was chosen to minimize evolution of the system during an EDXRD scan. Galvanostatic cycling at various rates were tested on a Maccor Cycler for the 3-dimensional porous electrode cells.

2.3 Methods

Models are fit to experiments as outlined by the parameter estimation procedure published by Brady et. al.[71] Different combinations of the unknown parameters are sampled from a uniform multivariate distribution, where the range of the distribution for each parameter is chosen to be sufficiently wide to encapsulate physically reasonable values of the parameters. The goodness of fit of each simulation is quantified by a residual sum of squares between the simulation and the experiment.

Since the physical model can simulate the results of electrochemical measurements as well as the spatial variation at different length scales, the model can be fit to both sets of data. This is done by combining the normalized error from fitting simulations to electrochemical measurements $e_{Voltage}$ with the normalized error from fitting to EDXRD measurements e_{EDXRD} to form a new objective function (Equation 2.1) and including an additional fitting parameter λ that weights the relative importance of the two measurements.

$$e_{total} = \lambda e_{Voltage} + (1 - \lambda) e_{EDXRD} \tag{2.1}$$

For these two sets of data, λ was chosen to range between 0 and 1, where the former corresponds to effectively fitting to only the electrochemical measurements and the latter corresponds to effectively fitting to only the EDXRD measurements.

2.4 Theory

2.4.1 Lithiation of β-phase in lithium trivanadate

A crystal-scale model of a single-phase insertion and phase change, and a coupled electrode-scale and crystal-scale model of a porous $Li_xV_3O_8$ cathode have been published by Brady et. al.[42,64] The model developed here builds on the coupled multiscale model by including physics for lithium insertion into the β-phase of $Li_xV_3O_8$.

Insertion of lithium into the β-phase is given by the simple reaction

$$Li^{+} + e^{-} + \Gamma_{\beta} \longrightarrow Li\Gamma_{\beta} \tag{2.2}$$

where Γ_{β} is an unoccupied site for insertion of lithium in the β-phase. The reversible potential for this reaction is given by

$$U_{\beta} = U_{ref,\beta} + \frac{RT}{F} ln \left[\left(\frac{c_0}{c_{bulk}} \right) \left(\frac{(1 - \overline{c_{\beta}})}{\overline{c_{\beta}}} \right) \right] \tag{2.3}$$

$$\overline{c_{\beta}} = \frac{c_{\beta} - c_{\beta 0}}{c_{\beta,max} - c_{\beta,0}} \tag{2.4}$$

where $\overline{c_{\beta}}$ is a dimensionless form of the concentration of lithium in the β-phase. The lithium ion concentration in the bulk electrolyte is given by c_{bulk} and c_0 is the local lithium ion concentration at different positions along the depth of the electrode.

The charge transfer kinetics are modeled using the Butler-Volmer equation:

$$i_{in,\beta} = \theta_{\beta} i_{0,\beta} \left(exp(\alpha_a \frac{F\eta_{\beta}}{RT}) - exp(-\alpha_c \frac{F\eta_{\beta}}{RT}) \right) \tag{2.5}$$

$$i_{0,\beta} = F k_{rxn,\beta} c_0^{\alpha_a} (c_{\beta} - c_{\beta 0})^{\alpha_c} (c_{\beta,max} - c_{\beta})^{\alpha_a} \tag{2.6}$$

The charge transfer overpotential for this reaction η_{β} is the difference between the potential in the solid state and in solution, and the reversible potential:

$$\eta_{\beta} = \Phi_1 - \Phi_2 - U_{\beta} \tag{2.7}$$

The governing equations for the crystal scale model are given by an overall lithium balance on the crystal, a lithium balance on the β-phase, and the rate of β-phase formation, given in Table 2.1. At the crystal edge, the flux of lithium into each phase is set equal to the local current density from the charge transfer kinetics for each reaction. The three dependent variables, concentration of lithium in the α-phase (c_α), concentration of lithium in the β-phase (c_β), and the volume fraction of the β-phase (θ_β) are solved for simultaneously.

Table 2.1: Governing equations and boundary conditions for mathematical model of lithium trivanadate crystal on the crystal scale.

	Governing Equation	Particle Center	Particle Edge
Overall Li Balance	$\frac{\partial(c_\alpha\theta_\alpha + c_\beta\theta_\beta)}{\partial t} = \theta_\alpha D_\alpha \nabla^2 c_\alpha + \theta_\beta D_\beta \nabla^2 c_\beta$	$\nabla c_\alpha = 0$	$-\theta_\alpha D_\alpha \nabla c_\alpha = \theta_\alpha \frac{i_{in,\alpha}}{F}$
Li balance in β-phase	$\frac{\partial(c_\beta\theta_\beta)}{\partial t} = \theta_\beta D_\beta \nabla^2 c_\beta + c_{\beta 0} R_\beta$	$\nabla c_\beta = 0$	$-\theta_\beta D_\beta \nabla c_\beta = \theta_\beta \frac{i_{in,\beta}}{F}$
Rate of β-phase formation	$R_\beta = \frac{\partial \theta_\beta}{\partial t} = k_\beta (c_\alpha - c_{\alpha,sat}) \theta_\beta^m (1 - \theta_\beta)^p$	Lithiation: m=0, p=1	Delithiation: m=1, p=0

2.4.2 Porous Electrode Model

The coupling between the electrode scale and the crystal scale is at the crystal edge boundary condition. The local reaction current densities $i_{in,\alpha}$ and $i_{in,\beta}$ are computed spatially across the length of the electrode based on the varying concentration of lithium in the electrolyte (c_0), solid state potential (Φ_1), and solution potential (Φ_2), the three dependent variables on the electrode scale. The spatial variation on the electrode scale are due to the fact that the electrode is porous, so there are transport limitations across its length. The governing equations and boundary conditions for the electrode-scale equations (Table 2.2) are consistent with the previously reported model, other than the inclusion of a second electrochemical reaction.

2.4.3 Ionic Transport

The effective diffusion coefficient $D_{0,eff}$ is defined as

$$D_{0,eff} = \frac{\epsilon D_0}{\tau} \tag{2.8}$$

where D_0 is the diffusion coefficient of lithium ions in the bulk electrolyte, ϵ is the porosity,

Table 2.2: Governing equations and boundary conditions for electrode-scale model.

	Governing Equations	Separator	Current Collector
Solid State Current (i_1)	$(1-\epsilon)\sigma\nabla^2\Phi_1 - a(i_{in,\alpha}+i_{in,\beta}) = 0$	$i_1 = 0$	$i_1 = i_{applied}$ $V_{cc} = \Phi_{1,cc}$
Electrolyte Current (i_2)	$\nabla \bullet (\kappa\Phi_2) + \epsilon F(Z_+D_+ + z_-D_-)\nabla^2 c_0 + a(i_{in,\alpha}+i_{in,\beta}) = 0$	$Phi_2 = 0$	$i_2 = 0$
Electrolyte Concentration (c_0)	$\epsilon\frac{\partial c_0}{\partial t} =$ $D_{0,eff}\nabla^2 c_0 + \frac{F}{RT}(Z_+D_+ + z_-D_-)c_0\nabla^2\Phi_2 + \frac{a(i_{in,\alpha}+i_{in,\beta})}{F}$	$c_0 = c_{bulk}$	$N = -D_{0,eff}\nabla c_0 = 0$

and τ is the tortuosity. The Bruggeman relationship for spherical particles (equation 2.9) is used to relate the tortuosity to the porosity.[72]

$$\tau = \epsilon^{-0.5} \tag{2.9}$$

This relationship is known to underestimate tortuosity in porous electrodes, but is used as a baseline in this study.[73,74]

2.4.4 Electronic Conductivity

The electronic conductivity of the electrode is modeled using percolation theory, depending on the volume fraction of conductive additive.[75] According to percolation theory, there is a significant increase in electronic conductivity when a critical volume fraction of the conductive additive is achieved, creating a connected conduction path through the electrode. This critical volume fraction, $\overline{v}_{percolation}$, has been reported over a wide range of values for different active materials and conductive additives, and is shown to be highly dependent on the aspect ratio of the conductor, as high aspect ratio additives can achieve a percolated network at lower volume fractions.[75–79] For this study $\overline{v}_{percolation}$=0.05 is chosen.

Below this percolation threshold, the electronic conductivity is given by

$$\sigma = \sigma_{AM}\left(\frac{\overline{v}_{percolation} - \overline{v}_{cond}}{\overline{v}_{percolation}}\right)^{-s} \tag{2.10}$$

where σ_{AM} is the intrinsic electronic conductivity of the active material, lithium trivanadate, and $\overline{v}_{cond}$ is the volume fraction of conductive additive. Previous reports have shown that s is approximately 1, so s is chosen as unity here.[80,81] Above the percolation threshold, the electronic conductivity is given by:

$$\sigma = \sigma_{cond}\left(\frac{\overline{v}_{cond} - \overline{v}_{percolation}}{1 - \overline{v}_{percolation}}\right)^{t} \tag{2.11}$$

where σ_{cond} is the intrinsic electronic conductivity of the conductive additive, multiwalled carbon nanotubes. The value of t has been reported between 1 and 3 for different systems.[75,77] Here, t=1 is chosen for simplicity. Figure 2.9 shows how the electrode conductivity varies with the volume fraction of MWNTs.

A summary of the selected model parameters, and a comparison to the parameters in the previously published model is given in Table 2.3.

2.5 Results

2.5.1 Extended First Cycle Model of the LixV3O8 Cathode

Three parameters needed to be estimated to complete the model development for the lithiation of the β-phase: $k_{rxn,\beta}$, associated with the charge transfer kinetics, D_{β}, the diffusion coefficient of lithium in the β-phase, and $U_{ref,\beta}$, the reference potential for the electrochemical reaction.

The model was fit to electrochemical data for a 330 μm electrode with a mass loading of 16 $mg\ cm^{-2}$. This electrode was highly porous (calculated porosity of $\epsilon = 0.74$ based on electrode preparation), and modeling confirmed that electrode-scale transport effects could be ignored. The parameter estimates are shown in Table 2.4. The diffusion coefficient needed to obtain agreement is consistent with a previous finding that the diffusion coefficient of lithium in the β-phase is three

Table 2.3: Comparison of model parameters in previously developed model[64] and current model for porous LixV3O8 cathode.

Parameter	**Symbol**	**Units**	**Brady et. al.[64]**	**Current study**
Electrode Scale				
Electronic conductivity in electrode	σ	$S\ cm^{-1}$	$1x10^{-2}$	-
Electronic conductivity of LVO	σ_{AM}	$S\ cm^{-1}$	-	$1x10^{-5}$
Electronic conductivity of conductive additive (MWNT)	σ_{cond}	$S\ cm^{-1}$	-	$1x10^{0}$
Crystal Scale				
Crystal Size	L_x	nm	60	60
Li diffusivity in α-phase	D_α	$cm^2\ s^{-1}$	$1x10^{-13}$	$1x10^{-13}$
Rate constant for Li insertion in α-phase	$k_{rxn,\alpha}$	$cm^{5/2}\ mol^{-1/2}\ s^{-1}$	$3.0x10^{-8}$	$3.0x10^{-8}$
Saturation concentration in α-phase for phase formation	$c_{\alpha,sat}$	x in $Li_xV_3O_8$	2.5	2.5
Reaction rate constant for phase change	k_β	$cm^3\ mol^{-1}\ s^{-1}$	$1.4x10^{-1}$	$1.4x10^{-1}$
Li concentration in β-phase as formed	$c_{\beta,0}$	x in $Li_xV_3O_8$	4.0	4.0
Li diffusivity in β-phase	D_β	$cm^2\ s^{-1}$	-	$7.5x10^{-16}$
Rate constant for Li insertion in β-phase	$k_{rxn,\beta}$	$cm^{5/2}\ mol^{-1/2}\ s^{-1}$	-	$2.5x10^{-8}$

orders of magnitude lower than the diffusion coefficient of lithium in the α-phase.8 Compared to the previously published model by Brady et. al., the model developed here shows improved agreement at the end of discharge, where lithiation of the β-phase is important.

Table 2.4: Parameter Estimates for Lithium insertion into β-phase.

Model Parameter	Value	95% Confidence Interval
$U_{ref,\beta}$ (V)	2.36	[2.34,2.38]
$k_{rxn,\beta}$ $(cm^{5/2}\ mol^{-1/2}\ s^{-1})$	2.5$x10^{-8}$	[1.4,4.3] $x10^{-8}$
D_β $(cm^2\ s^{-1})$	7.5$x10^{-16}$	[6.5, 8.6] $x10^{-16}$

The fitted model shows good agreement with electrochemical measurements for a 741 μm, 10 $mg\ cm^{-2}$ electrode discharged at three different current rates (1C = 362 $mA\ g^{-1}$) (Figure 2.1). At the higher current rates, insertion of lithium into the α-phase outcompetes phase change, causing the potential to drop rapidly before a significant fraction of the crystal has been converted to the β-phase. Because less of the crystal undergoes phase change, lithiation of the β-phase is not as significant at high rates. Simulations corresponding to the electrodes shown in Figure 1 reveal that at C/10, the average value of the dimensionless concentration c_β is 0.31 at the end of discharge, and at 1C, this number falls to $c_\beta = 0.02$.

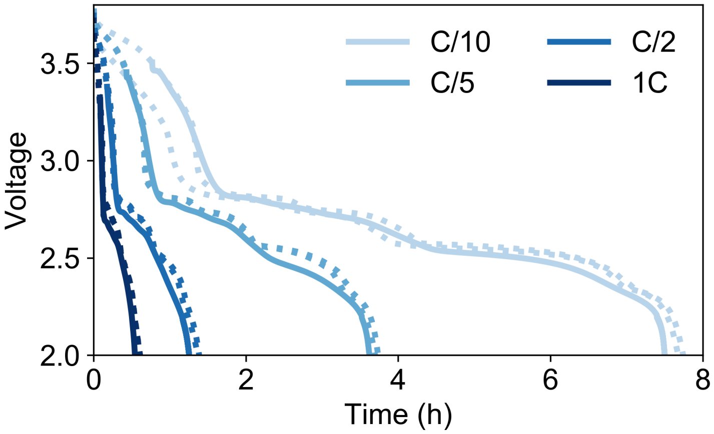

Figure 2.1: Agreement between experiments (dashed lines) and simulations (solid lines) for discharge of 3-dimensional porous electrodes at three different current rates.

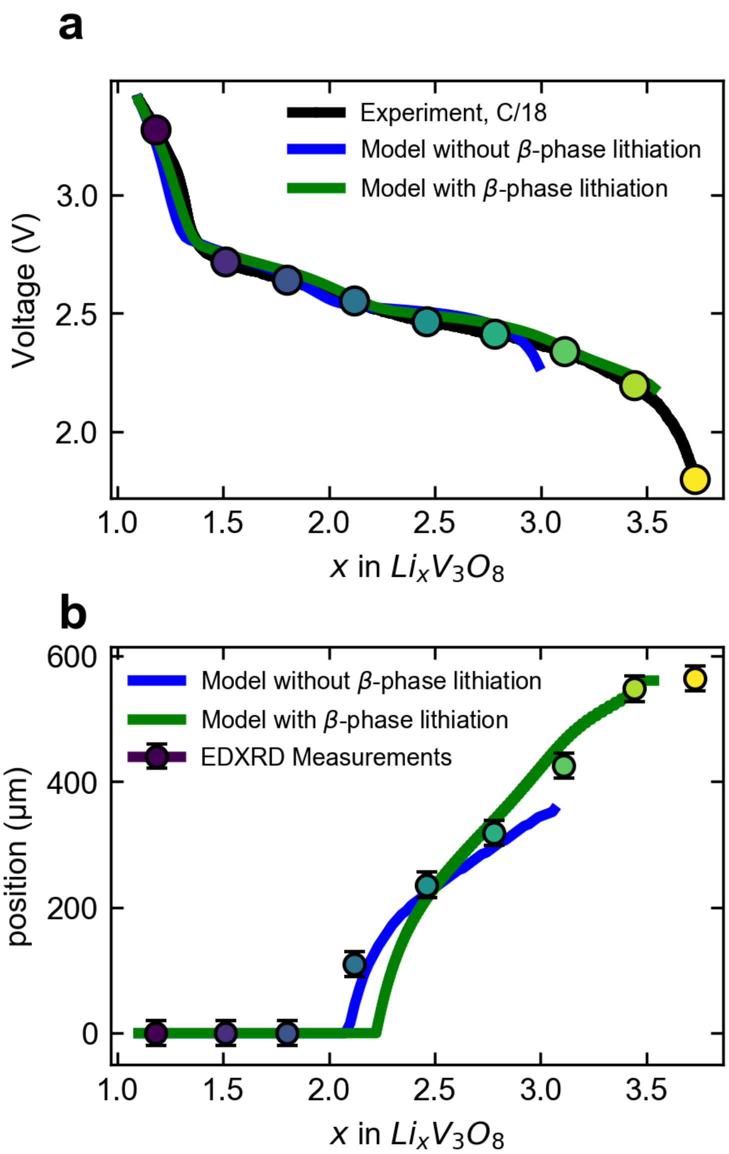

Figure 2.2: (a) Electrochemical measurements for C/18 discharge of 561 μm thick cathode. Experimental potential measurements shown are shown in black. Simulated electrochemical behavior of the previously published model ignoring lithiation of the β-phase is shown in in blue, and the simulated behavior accounting for lithiation of the β-phase is shown in in green. Points correspond to depths of discharge at which EDXRD measurements were taken. (b) Points correspond to the measured position of the phase change front, associated by color with the points in (a). The simulated movement of the front throughout the depth of discharge is shown for the previously published model and the extended model.

2.5.2 Operando EDXRD Measurements

Figure 2.2a compares agreement of both the previously published model and the extended model with an experiment where a thick (561 μm) pellet electrode was discharged at 20.17 $mA\ g^{-1}$, corresponding to a current rate of C/18. In the previous study, the effective diffusion coefficient for transport of lithium ions through the electrolyte $D_{eff,0}$ was estimated to be 5.5×10-7 $cm^2\ s^{-1}$. To achieve agreement with the electrochemical and EDXRD measurements using the two-phase insertion model, the effective diffusion coefficient was refit. Fitting to only the electrochemical measurements (λ = 0, see Equation 2.1) $D_{eff,0}$ was determined to be 2.6 ×10-7 $cm^2\ s^{-1}$. Fitting to only the EDXRD measurements (λ = 1), $D_{eff,0}$ was determined to be 2.7 ×10-7 $cm^2\ s^{-1}$. Therefore, similar diffusivities were determined, bolstering the claim that the model captures the physics on the electrode scale as well as the crystal scale.

The circles overlaid on the experimental discharge profile in Figure 2.2a indicate the depths of discharge at which EDXRD measurements were taken. The locations where the phase change front was detected by the EDXRD at these depths of discharge are shown by the points in Figure 2.2b, where the vertical error bars are 20 μm. A comparison of the movement of the phase change front across the length of the electrode as measured and as simulated is presented in Figure 2.2b. A minimum β-phase volume fraction of 5% is assumed to be the limit of detection,15 and this value was used to determine the phase change front from the simulations. The extended model overpredicts the depth of discharge at which the onset of phase formation occurs, but shows good agreement with the phase change front measured with EDXRD.

In addition to comparing the movement of the front, the model can provide insight into the spatial variation of the volume fraction of the β-phase during discharge. Figure 2.10 shows this volume fraction as a function of position at different depths of discharge, where phase change occurs preferentially near the separator because lithiation of the α-phase is slow near the current collector due to electrode-scale transport limitations. Throughout the duration of the experiment the reaction front shows an extended region where the volume fraction of the β-phase changes gradually.

2.5.3 Optimization

Performance of various electrode architectures was quantified by volumetric energy density E_V and the areal density E_A, given in equations 2.12 and 2.13. E_A is calculated by integrating the discharge profile V(t) over the total discharge time t_{dchg} given an applied current density $i_{applied}$. The time for discharge t_{dchg} is the time to reach a cutoff voltage of 2.0 V. The volumetric energy density E_V is the areal density E_A divided by the cell thickness, given by $L_{cathode}$ and the thickness of the balance of the cell (i.e. anode, separator, current collectors) L_{BOC}. The anode thickness is calculated by matching the anode capacity Q_a to the simulated cathode capacity Q_c, given the mass loading m_{LVO} ($mg\ cm^{-2}$) and assuming a graphite anode with a fixed porosity of $\epsilon_{anode} = 0.35$.22 The thicknesses of the separator and current collectors, along with other assumed constants, are shown in Table V.

$$E_A = \int_0^{t_dchg} V(t) i_{applied} dt \tag{2.12}$$

$$L_{anode} = \frac{Q_c m_L VO}{Q_a(1-\epsilon_{anode})\rho_{graphite}} \tag{2.13}$$

$$L_{BOC} = L_{anode} + L_{separator} + L_{cc}^{anode} + L_{cc}^{cathode} \tag{2.14}$$

$$E_V = \frac{E_A}{L_{cathode} + L_{BOC}} \tag{2.15}$$

E_A in equation 2.12 is calculated based on a voltage versus Li metal, and changes in the anode potential as a function of time are not considered. Though this consideration will marginally reduce the values of E_A and E_V reported, the optimization conducted in this study is on the cathode fabrication, so the optimal thicknesses, porosities, and volume fractions of conductive additive will remain the same.

The effective diffusivity for lithium ions in the electrolyte is determined based on the value fitted to the operando EDXRD experiment $D_{eff,0}^{EDXRD}$, the porosity of the electrode in that experiment ϵ_{EDXRD}, and the porosity of the simulated electrode ϵ per equations 2.8 and 2.9.

$$D_{0,eff} = D_{0,eff}^{EDXRD} \left(\frac{\epsilon}{\epsilon_{EDXRD}} \right)^{1.5} \tag{2.16}$$

A comparison of electrode volumetric energy density ($E_A/L_{cathode}$) for two fabricated electrodes with the maximum achievable E_V is shown in Figure 2.3. There is room for improvement in electrode energy density, up to an order of magnitude, by tuning the design parameters during electrode fabrication.

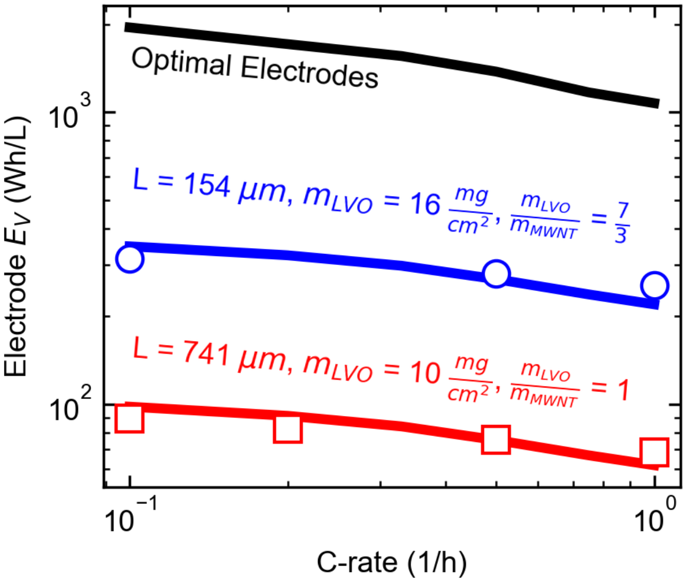

Figure 2.3: Electrode energy density E_V over a range of discharge rates from C/10 to 1C. Points correspond to experimentally measured E_V from rate capability tests for two electrodes. The corresponding blue and red solid lines are the simulated E_V for these two electrodes. The blue electrode corresponds to ϵ=0.74 and $\overline{v}_{cond}$=0.08, and the red electrode corresponds to ϵ=0.90 and $\overline{v}_{cond}$=0.06. In black, the maximum achievable electrode E_V by optimizing electrode design at each individual discharge rate is shown.

Figure 2.4 shows the maximum achievable cell E_V (4a), as well as the values of the design parameters required to achieve those maxima (b-d). An energy density of 556 $Wh\ L^{-1}$ can be achieved at a C/10 discharge rate. At 1C, this maximum achievable E_V falls to 300 $Wh\ L^{-1}$. From low to high C-rate, the optimal electrode thickness decreases from 154 μm to 85 μm, while the optimal porosity increases from 0.16 to 0.26, and the optimal volume fraction of the conductor remains just above the percolation threshold at 5.5%. The net effect is a decrease in mass loading with C-rate from 38 to 18 $mg\ cm^{-2}$ (Figure2.11).

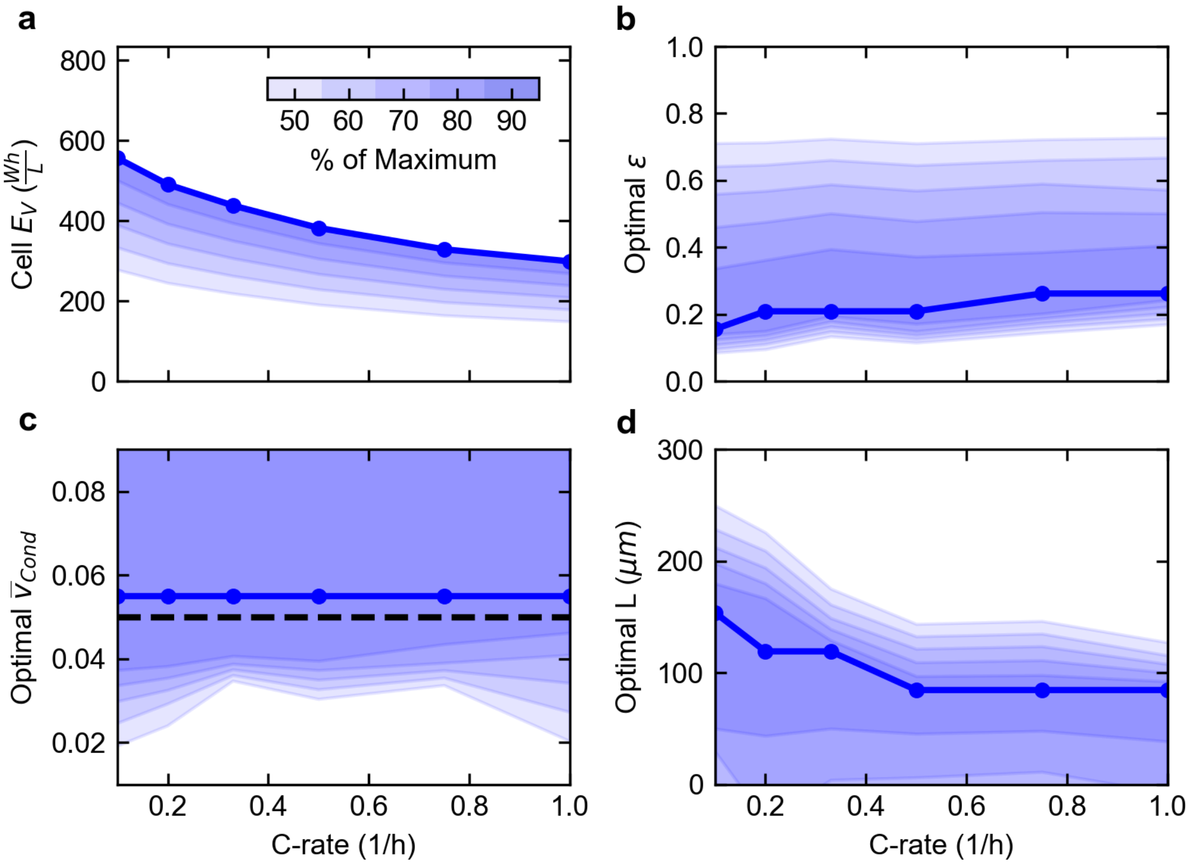

Figure 2.4: The maximum achievable cell energy density E_V over a range of discharge rates from C/10 to 1C (a) and the porosity, volume fraction of conductor, and electrode thickness with which an electrode should be fabricated to achieve that E_V(b-d). Shaded contours in (b-d) correspond to the range of values of the design parameters that will give a certain percentage (see color scale inset in a) of the maximum achievable E_V at a given discharge rate.

Because the three design parameters chosen all affect electrode-scale transport, the optimal design parameters result from minimizing losses due to poor lithium ion transport in the electrolyte, ensuring that all the material through the length of the electrode is utilized. The reduction in the energy density despite minimal transport losses indicate that the rate capability of the lithium

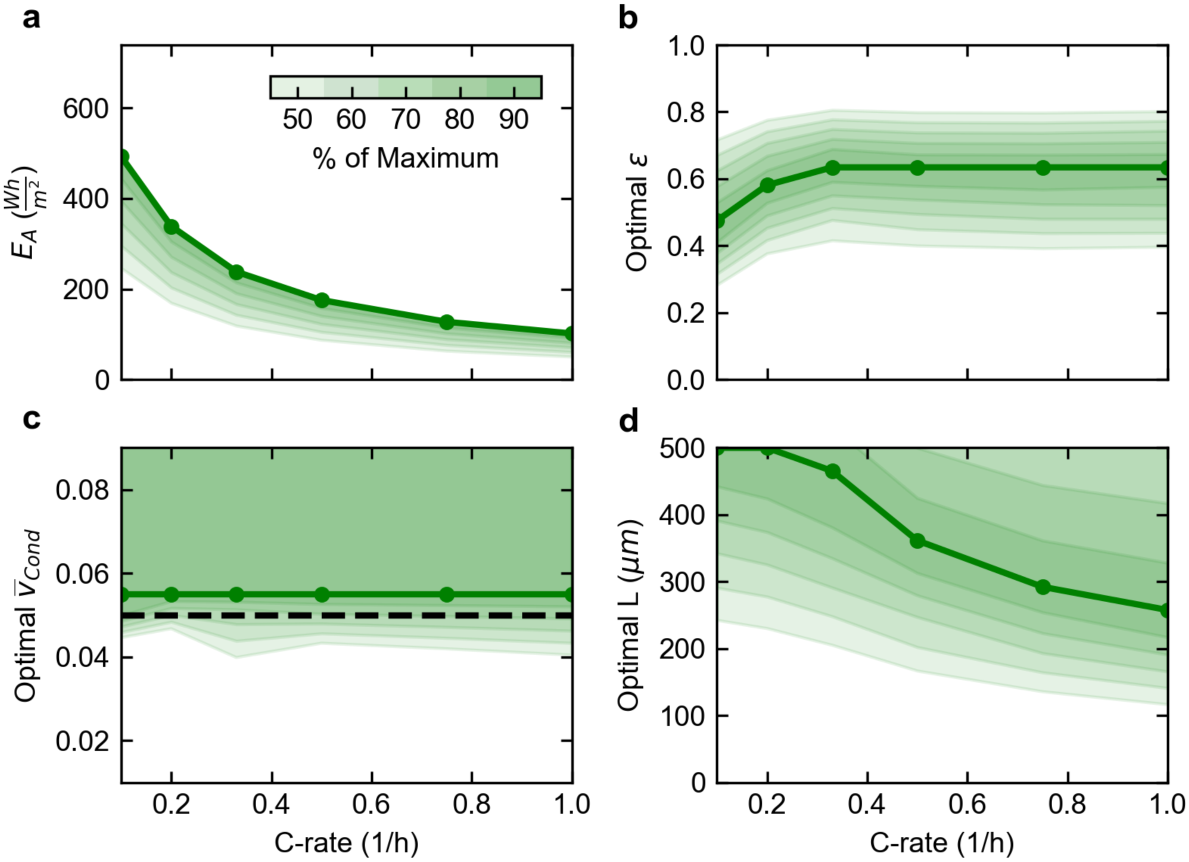

Figure 2.5: The maximum achievable cell energy density E_A over a range of discharge rates from C/10 to 1C (a) and the porosity, volume fraction of conductor, and electrode thickness with which an electrode should be fabricated to achieve that E_A (b-d). Shaded contours in (b-d) correspond to the range of values of the design parameters that will give a certain percentage (see color scale inset in a) of the maximum achievable E_A at a given discharge rate.

trivanadate electrode is limited by diffusion of lithium in the crystal itself: at higher discharge rates, active material within each crystal is underutilized. Figure 2.12 shows uniform utilization of the electrode optimized for each discharge rate. Further investigation reveals that for crystals near the separator, in the middle of the electrode, and near the cathode current collector, the concentration profiles within the crystal are similar, but the average utilization of each crystal decreases with discharge rate (Figure 2.13).

The maximum possible E_A ranges from 493 Wh m-2 to 102 Wh m-2 for discharge rates between C/10 and 1C (Figure 2.5). The range of optimal porosities is higher, between 0.48 and 0.63, and the optimal electrode length varies significantly as a function of C-rate, from 500 μm at C/10 to 258 μm at 1C. It should be noted that at C/10, the optimum is likely above 500 μm, but 500 μm was the maximum electrode thickness considered in this study. These optimal design parameters correspond to mass loadings in the range of 74 to 25 $mg\ cm^{-2}$. Since there is not a volume penalty when optimizing for E_A, thicker electrodes with higher areal loading are preferred, compared to optimization of E_V. Again, volume fractions of conductors are always chosen above the percolation threshold.

The sensitivity of E_V and E_A to the various design parameters are shown in the shaded contours in Figures 4 and 5. For each design parameter, the contour line was chosen by finding the maximum and minimum value of that design parameter to achieve a certain percentage of the maximum E_V or E_A when holding the other design parameters constant at their optimal values. The sensitivity of E_V to porosity is highly asymmetric (Figure 2.4b). For example, consider the C/3 discharge rate in Figure 2.4b. An E_V that is 50% of the maximum possible E_V at C/10 can be obtained by increasing the porosity for a 119 μm thick electrode with 0.055 volume fraction of conductor from 0.26 to 0.74, equivalent to a decrease in mass loading of 18 $mg\ cm^{-2}$. However, to achieve that same E_V by decreasing the porosity and increasing the mass loading, the porosity need only be reduced to 0.18, corresponding to an increase in mass loading of 3 $mg\ cm^{-2}$. This asymmetry in sensitivity is due to the more rapid change in the effective diffusivity as porosity is increased in the low porosity regime (Figure 2.6a,b). In this regime, the effect of reducing the active material loading by increasing the porosity is minimal compared to the gain in favorable ionic transport as the effective diffusivity changes ($D_{0,eff}\quad\epsilon^{1.5}$). Above the optimum porosity, the improvement in effective diffusivity is marginal, and the reduction energy density is driven by a decrease in active material loading, which decreases linearly with porosity. These results indicate that the sensitivity of the energy density to porosity is controlled by the tortuosity's dependence on the porosity, or the Bruggeman exponent. Without this dependence, the energy density would be symmetrically sensitive to changes in porosity about the optimum.

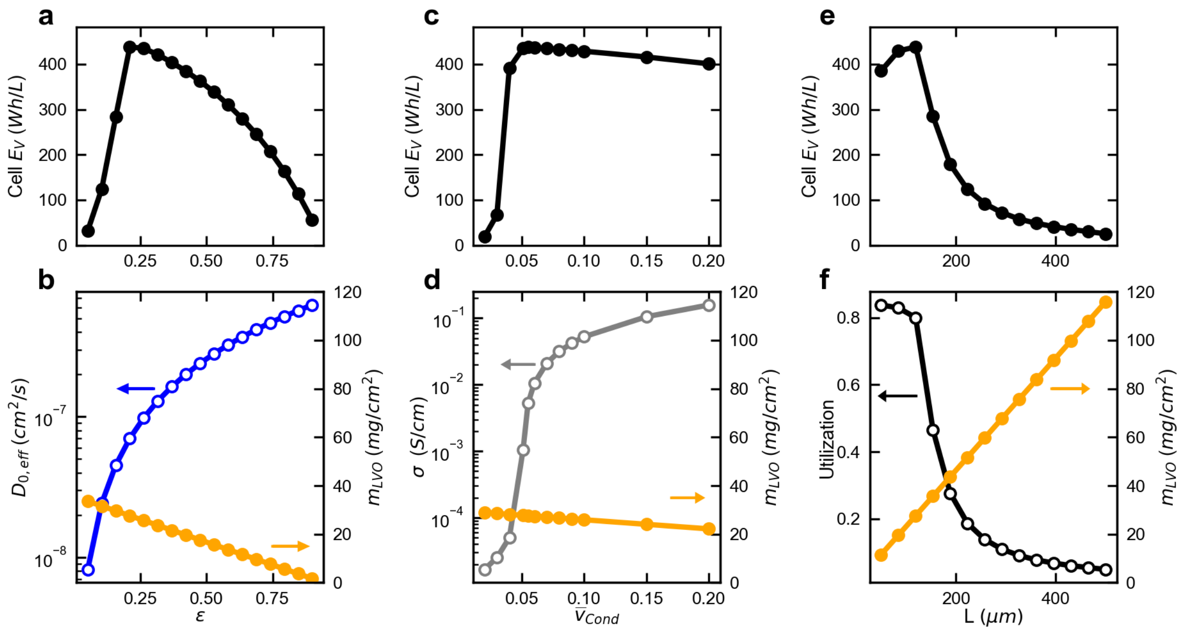

Figure 2.6: Sensitivity of cell energy density to porosity (a,b), volume fraction of conductor (c,d), and electrode length (e,f). Top row (a,c,e) show how the energy density varies as the design parameter is changed, holding the other two design parameters fixed. The variation in the effective diffusivity of lithium ions and active material loading when porosity is changed is shown in (b) for a 119 μm thick electrode with $\overline{v}_{cond}$=0.055. The change in electronic conductivity and active material loading when the volume fraction of conductor is varied is shown in (d) for a 119 μm thick electrode with ϵ=0.26. Finally, the change in electrode utilization and active material loading as electrode thickness is increased is shown in (f) for an electrode with ϵ=0.26 and $\overline{v}_{cond}$=0.055.

The sensitivity of E_A to porosity appears to be much more symmetric than in the case of optimizing for E_V. This can be explained by the fact that the optimal porosity is near 0.6, as opposed to 0.2 for E_V. In the higher porosity regime, $D_{0,eff}$ is not as strong a function of porosity as it is in the lower porosity regime.

For a given electrode porosity and volume fraction of conductor, the electrode thickness scales linearly with the mass loading of active material. As the thickness is increased, there is a gain in volumetric energy density associated with the increase in mass loading (Figure 2.6e). However, because the optimal electrode has a porosity of 0.26 for a C/3 discharge, the effective diffusivity of lithium ions is limited, so the length over which the electrode is entirely utilized is also limited. This is apparent in Figure 2.6f, where until 150 μm, the entire electrode is utilized, but for electrodes thicker than this, the electrode length is greater than the critical diffusion length, and the electrode utilization falls off, causing the volumetric energy density to fall off as well.

The volume fraction of conductive additive is highly asymmetric in its effects on both E_V and E_A. There is very little penalty to increasing the fraction of conductive additive above the percolation threshold, since the conductivity is already at a value that is sufficient to avoid electronic transport resistances (5 ×10-3 $S\ cm^{-1}$, Figure 2.9). However, since the conductivity drops off so rapidly below the percolation threshold, there is an extreme sensitivity to reducing the fraction of conductor. The sensitivity analysis with respect to volume fraction of conductor for E_V is presented in Figure 2.6c and d for a discharge rate of C/3.

Figure 2.7 shows a comparison of the maximum achievable E_V with a graphite anode with ϵ = 0.35 and a lithium metal anode. As expected, the optimal cathode design is independent of the choice of anode (Figures 7b,c,d). By moving from a graphite anode to a lithium metal anode, the increase in cell energy density can be up to 71% at C/10, to 55% at 1C. The anode thicknesses corresponding to the optimize cathode are shown in Figure 2.7d. Because lithium metal has such a high specific capacity (3860 mAh g-1) compared to graphite (372 mAh g-1), the thickness of the lithium metal anode is not as strong a function of the cathode mass loading. However, the graphite anode thickness varies more strongly with cathode mass loading, from 124 μm to 260 μm between 1C and C/10. This change explains the difference in improvement of cell energy density by switching out a graphite anode for a lithium metal anode at slower and faster discharge rates.

Since phase change has been shown to contribute to capacity fade in lithium trivanadate cath-

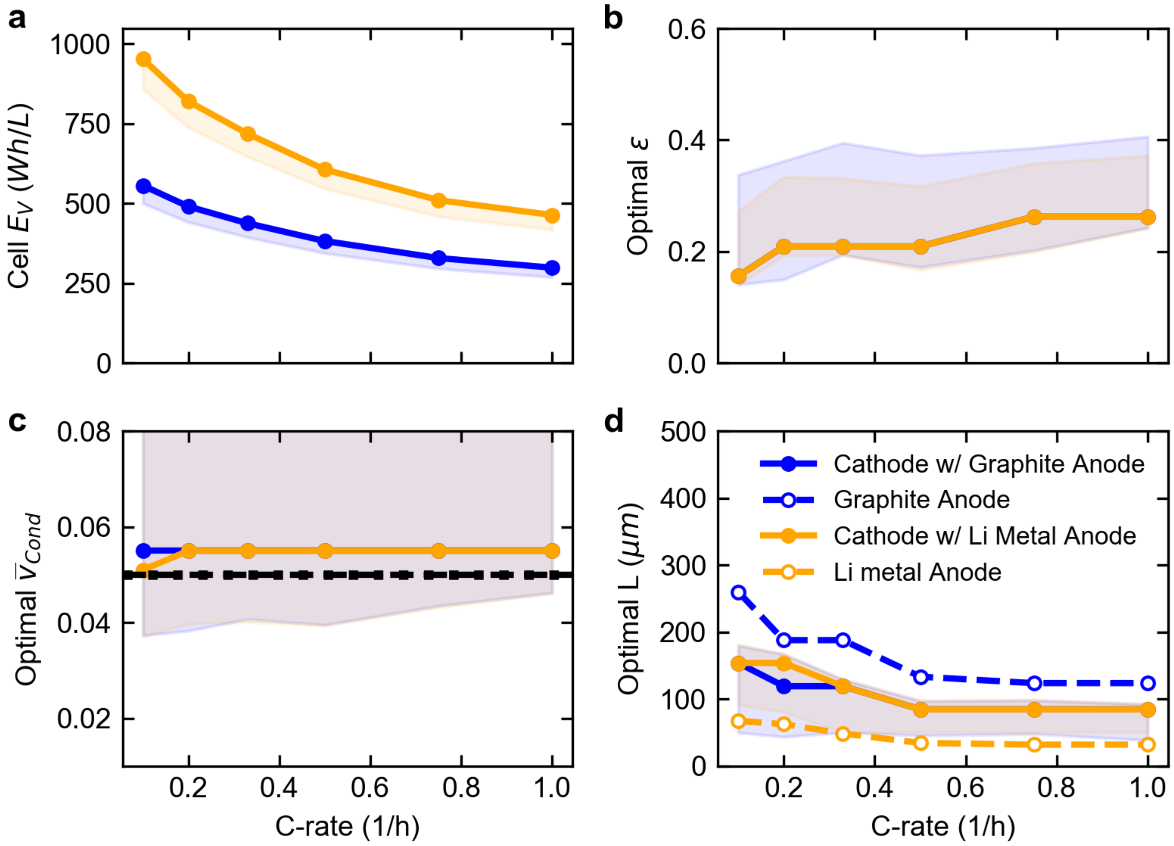

Figure 2.7: The maximum achievable cell energy density E_V over a range of discharge rates for cells with a graphite anode (blue) and a lithium metal anode (yellow) (a) and the porosity, volume fraction of conductor, and electrode thickness with which an electrode should be fabricated to achieve that E_V (b-d). Shaded regions correspond to the range of values of the design parameters that will give 90% of the maximum achievable E_V at a given discharge rate. The thicknesses of both electrodes for each cell are shown in (d).

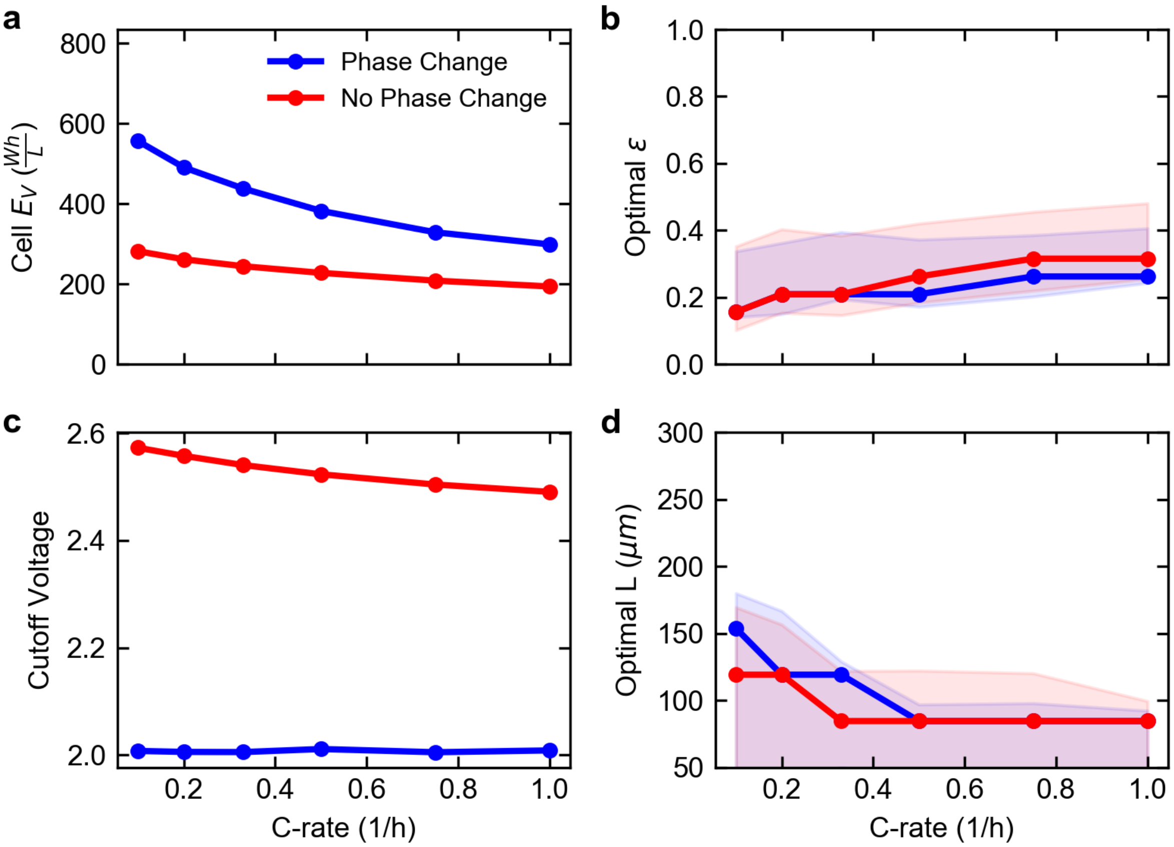

Figure 2.8: The maximum achievable cell energy density E_V over a range of discharge rates with and without phase change (a) and the porosity, volume fraction of conductor, and electrode thickness with which an electrode should be fabricated to achieve those E_Vs (b,d). (c) gives to the cutoff voltage used for the analysis at each discharge rate.

odes,9,32 the effect of avoiding the phase change entirely on optimization of E_V is explored. The phase transition does not involve an electron transfer and occurs when the local lithium ion concentration has exceeded $Li_{2.5}V_3O_8$. At slower discharge rates, the phase change kinetics are fast compared to the intercalation of lithium ions, and a voltage plateau is observed in the discharge profile. At higher discharge rates, the rate of intercalation of lithium ions becomes faster than the rate of conversion, and charge transfer losses are amplified. As a result, phase change begins to occur at lower voltages for faster discharge rates for a given electrode.

Figure 2.8 gives the maximum achievable values of E_V with and without phase change as a function of discharge rate. Since volume fraction of conductor was shown not to make a difference in the previous analyses, $\overline{v}_{cond} = 0.06$ was chosen. The optimal porosity and electrode length when discharging to avoid the phase transition (Figures 8b, 8d) do not deviate much from the base case of the full discharge, and fall on top of the base case optimums at high discharge rates. The voltage at which to cut off the discharge for these optimal electrodes to prevent β-phase formation is shown in Figure 2.8c. At slower discharge rates, a significant portion of the energy density is sacrificed when avoiding the phase change (50% reduction in E_V at C/10). However, the energy density opportunity cost for avoiding phase change to extend cycle life is smaller at higher C-rates. At 1C, a 36% reduction in E_V results from avoiding phase change. Therefore, for high rate applications where cycle life is important, cycling to a cutoff voltage that avoids the formation of the β-phase may be highly advantageous.

2.6 Conclusion

A continuum model was developed to describe discharge of the lithium trivanadate cathode for its full depth of discharge, and validated by both electrochemical data and EDXRD measurements. The model is then used to guide electrode fabrication to optimize volumetric and areal energy density by tuning the porosity, length, and volume fraction of the conductive additive. Optimal values of these design parameters are identified over a range of discharge rates between C/10 and 1C, and the sensitivity of the volumetric and areal energy density to the three design parameters is quantified. The optimization analysis is applied to interrogate the differences in electrode fabrication with the design constraint of avoiding the phase transition to extend cycle life. It was determined that the energy density penalty with this constraint decreased at faster discharge rates, and that for a given set of design parameters, the cutoff voltage to avoid phase change decreased with increasing discharge rate.

2.7 List of Symbols

Table 2.5: Crystal Scale Symbols

Symbol	**Definition**
c_{α}	Concentration f Li in α-phase ($mol\ cm^3$)
$c_{\alpha,sat}$	Saturation concentration of Li in the α-phase, above which phase change occurs ($mol\ cm^3$)
$c_{\alpha,max}$	Maximum concentration of Li in the α-phase ($mol\ cm^3$)
$c_{\beta,0}$	Concentration of Li in the β-phase upon formation from the α-phase ($mol\ cm^3$)
c_{β}	Concentration of Li in the β-phase ($mol\ cm^3$)
$c_{\beta,max}$	Maximum concentration of Li in the β phase ($mol\ cm^3$)
D_{α}	Diffusivity of Li in the α-phase ($mol\ cm^3$)
D_{β}	Diffusivity of Li in the β-phase ($mol\ cm^3$)
θ_{α}	Volume fraction of α-phase
θ_{β}	Volume fraction of β-phase
k_{β}	Reaction rate constant for phase change (cm^3 mol−1 s^{-1})
R_{β}	Rate of β-phase formation (s^{-1})

Table 2.6: Reaction Thermodynamics and Charge Transfer Kinetics Symbols

Symbol	**Definition**
$k_{rxn,\alpha}$	Exchange current reaction rate constant for Li intercalation in the α-phase ($cm^{5/2}\ mol^{-1/2}\ s^{-1}$)
$k_{rxn,\beta}$	Exchange current reaction rate constant for Li intercalation in the β-phase ($cm^{5/2}\ mol^{-1/2}\ s^{-1}$)
$i_{in,\alpha}$	Local current density for Li intercalation in α-phase ($A\ cm^{-2}$)
$i_{in,\beta}$	Local current density for Li intercalation in β-phase ($A\ cm^{-2}$)
$i_{0,\alpha}$	Exchange current density for Li intercalation in α-phase
$i_{0,\beta}$	Exchange current density for Li intercalation in β-phase
U_α	Reversible potential for Li intercalation in α-phase (V)
U_β	Reversible potential for Li intercalation in β-phase (V)
α_a	anodic charge transfer coefficient
α_c	cathodic charge transfer coefficient
R	Ideal gas constant (8.314 $J\ mol^{-1}\ K^{-1}$)
F	Faraday's constant (96,485 $C\ mol^{-1}$)
T	Temperature (K)

Table 2.7: Electrode scale symbols

Symbol	**Definition**
a	Specific surface area ($cm^2\ cm^{-3}$)
c_0	Li-ion concentration in the electrolyte ($mol\ cm^-3$)
c_{bulk}	Li-ion concentration in the bulk electrolyte ($mol\ cm^-3$)
$i_{applied}$	Applied current density ($A\ cm^{-2}$)
D_0	Diffusivity of Li-ions in the bulk electrolyte ($cm^2\ s^{-1}$)
$D_{0,eff}$	Effective Diffusivity of Li-ions in the electrolyte in the porous electrode ($cm^2\ s^{-1}$)
ϵ	Void fraction of porous electrode (porosity)
τ	Tortuosity
σ	Electronic conductivity in solid ($S\ cm^{-1}$)
κ	Iionic conductivity of bulk electrolyte ($S\ cm^{-1}$)
z_i	Species charge
u_i	Species mobility ($cm^2\ s\ mol\ J^{-1}$)
Φ_1	Solid state potential (V)
Φ_2	Solution potential (V)
c.c.	current collector

Table 2.8: Electrode and Cell Fabrication Symbols

Symbol	Definition
m_{LVO}	Active material mass loading ($g\ cm^{-2}$)
ρ_{LVO}	Density of lithium trivanadate (3.15 $g\ cm^{-3}$)
$L_{cathode}$	Cathode thickness (cm)
L_{anode}	Anode thickness (cm)
L_{BOC}	Thickness of the balance of cell components: separator, current collectors (cm)

Table 2.9: Cell Performance Optimization Symbols

Symbol	Definition
t_{dchg}	Time to complete discharge (h)
E_A	Areal energy density ($Wh\ m^{-2}$)
E_V	Volumetric energy density ($Wh\ L^{-1}$)
Q_c	Cathode specific capacity ($mAh\ g^{-1}$)
Q_a	Anode specific capacity ($mAh\ g^{-1}$)

2.8 Supplementary Information

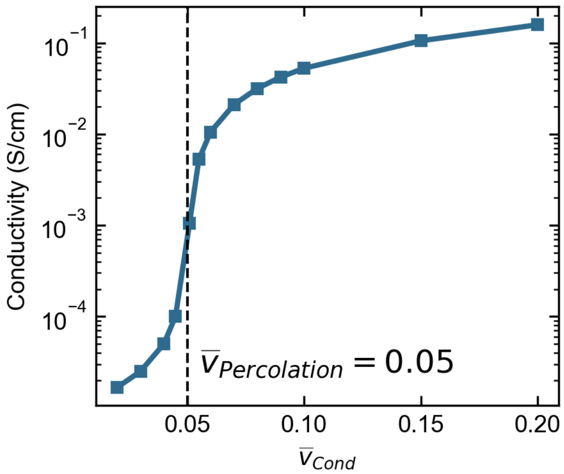

Figure 2.9: Model for electronic conductivity varying with volume fraction of conductive additive.

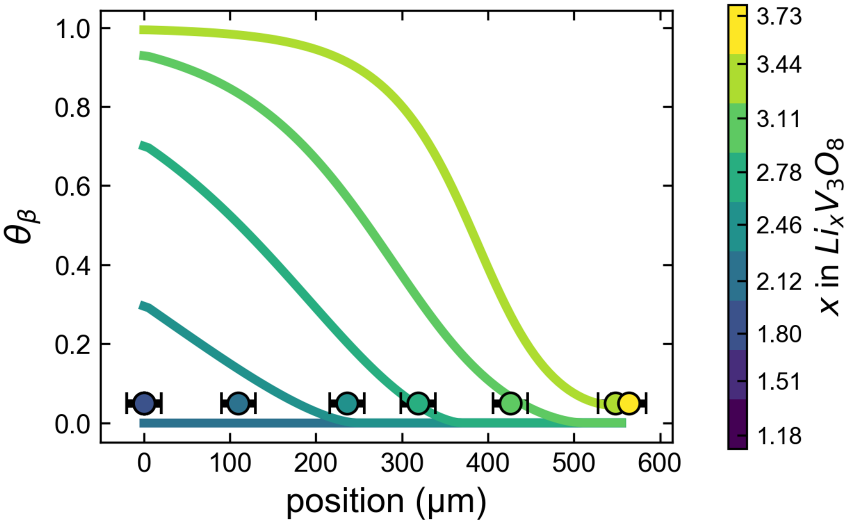

Figure 2.10: Spatial variation of the volume fraction of the β-phase at the depths of discharge (color bar) at which EDXRD measurements were taken.

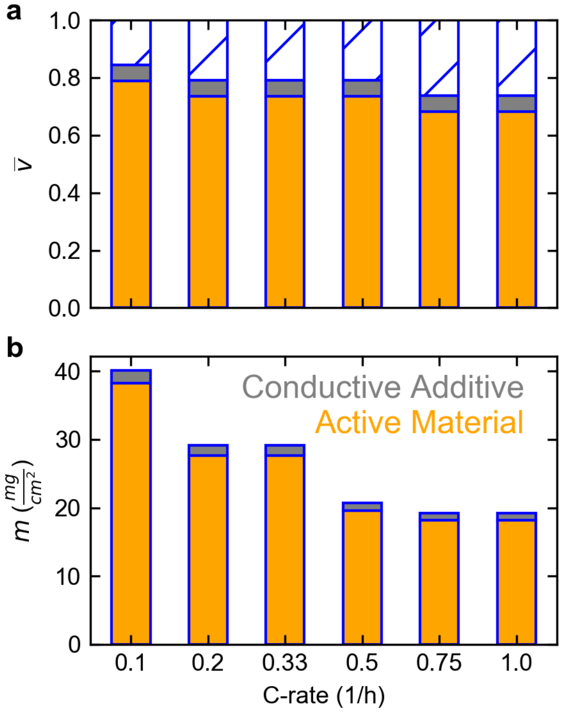

Figure 2.11: Volume fraction distribution (a) and mass loading (b) for electrodes that maximize cell energy density at discharge rates from C/10 to 1C. Orange corresponds to active material (lithium trivanadate), grey corresponds to conductive additive (multiwalled carbon nanotubes) and the hashed bars in (a) correspond to pore volume.

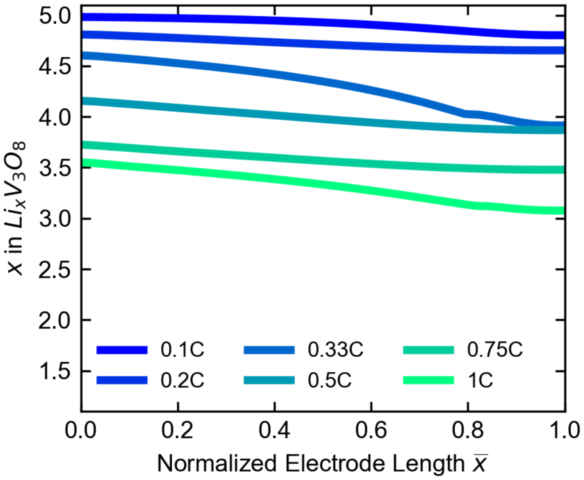

Figure 2.12: Utilization of the crystals along the length of the electrode at the end of discharge optimized for cell energy density at each discharge rate.

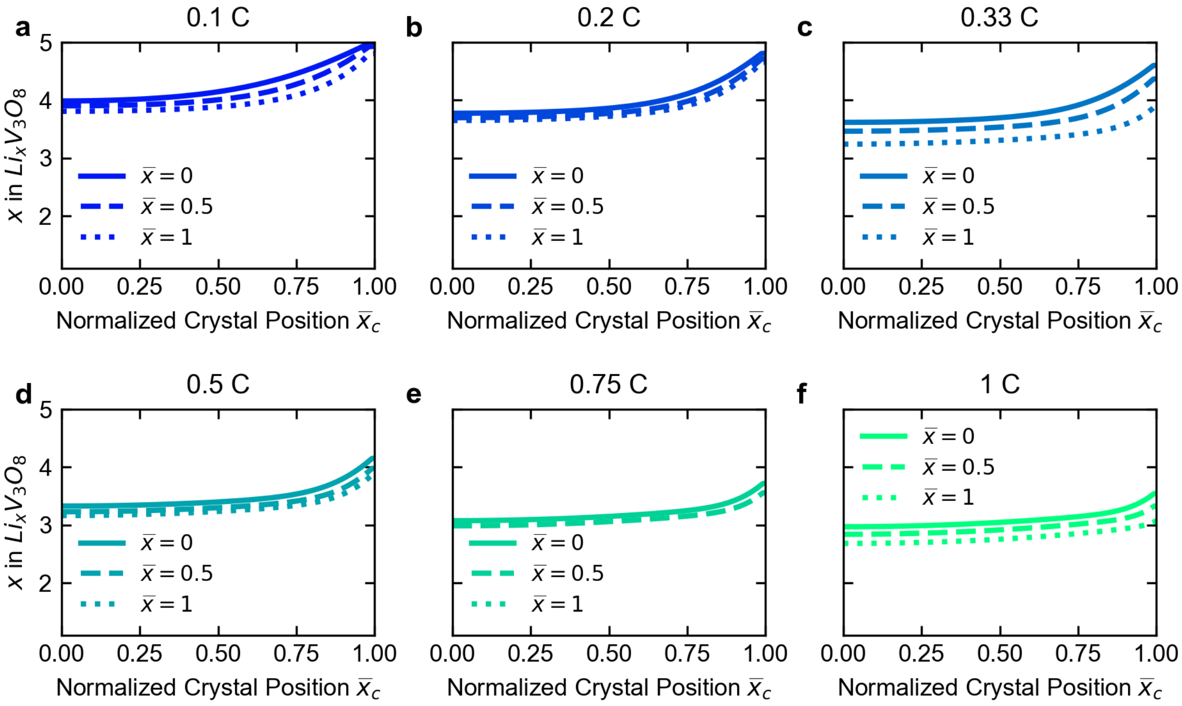

Figure 2.13: Concentration profiles of lithium from center of crystal (left) to crystal edge (right) at the end of discharge for crystals near the separator ($\bar{x} = 0$), in the center of the electrode ($\bar{x} = 0.5$), and near the cathode current collector ($\bar{x} = 1$), for six discharge rates from C/10 to 1C (a-f).

Chapter 3

Quantifying Uncertainty in Tortuosity Estimates for Porous Electrodes[*]

---

[*] This chapter has been published: Karthik S. Mayilvahanan, Zeyu Hui, Kedi Hu, Jason Kuang, Alison H. McCarthy, John Bernard, Lei Wang, Kenneth J. Takeuchi, Amy C. Marschilok, Esther S. Takeuchi, Alan C. West, "Quantifying Uncertainty in Tortuosity Estimates for Porous Electrodes," *Journal of the Electrochemical Society.*, vol. 168, no. 7, p. 070537, Jul. 2021.
The thesis writer's contribution was physics-based model analysis and experimental design, and writing. The electrochemical observations for LVO were provided by Jason Kuang and Alison McCarthy from the Marschilok-Takeuchi Research Group at Stony Brook University. The electrochemical observations for NMC were provided by Kedi Hu, Zeyu Hui, and John Bernard from the West Group at Columbia University.

3.1 Introduction

Understanding and characterizing the limitations to high rate performance of lithium ion battery (LIB) electrodes is essential in enabling high loading electrodes for high energy density LIBs. One major limitation to rate performance of high loading LIB electrodes is the transport of lithium ions through the electrolyte phase. A characteristic property of electrodes that describes the ease or difficulty of lithium-ion transport through the electrode and the associated ohmic losses is the electrode tortuosity τ. When quantified accurately and precisely the electrode tortuosity can parameterize physics-based models that can be used for performance prediction, diagnosis, and optimization.[14,82]

There are several definitions of tortuosity in the literature, including microscopic definitions and geometric definitions.[83] In this work, we will address tortuosity from the macroscopic view of a porous medium, as described by the MacMullin Number N_M:[84]

$$\frac{\tau}{\epsilon_e} = \frac{D_{e,0}}{D_{e,eff}} = \frac{\kappa_{e,0}}{\kappa_{e,eff}} = N_M \tag{3.1}$$

where ϵ_e is the electrode porosity (volume fraction of the electrolyte phase, denoted by subscript e) and D and κ are electrolyte diffusivities and conductivities, with subscript 0 indicating a bulk property and subscript eff indicating an effective property.

Several methods exist in the literature for quantifying tortuosity in porous electrodes. Tortuosity can be calculated from reconstructed microstructure using X-ray computed tomography (XCT) and focused-ion beam SEM (FIB-SEM).[21,85–87] These techniques suffer from limited resolution, as representative volumes are much smaller than the electrodes themselves. Observing the conductive carbon and binder domains, which have been shown to impact tortuosity,[88–90] also remains challenging. Some have worked around this limitation by numerically generating these inert domains to assess their impact on tortuosity.[91,92]

Thorat et. al. published a polarization-interrupt method, where an electrode is sandwiched between two separators in a lithium/lithium cell.[93] Polarization of this cell induces a concentration gradient in the liquid phase, and the subsequent relaxation of this concentration gradient when the polarization is interrupted produces a response in the measured solution potential, which can be mapped to an effective diffusion coefficient and thus a tortuosity via Equation 3.1. A similar method is used by Gasteiger and coworkers to quantify bulk transport properties in electrolytes.[94,95] In terms of practical implementation for cathode materials, this technique can prove challenging because it requires fabrication of a freestanding electrode that can be placed in the unique electrode configuration.

The most widely adopted method for estimating tortuosity is the use of electrochemical impedance spectroscopy (EIS) under blocking conditions.[74] A nonreactive electrolyte is chosen to prevent charge transfer (i.e., blocking), such that a transmission line model (TLM) originally proposed by de Levie can be applied to interpret the impedance of the porous electrode.[96] The TLM treats porous electrodes as a set of one dimensional, homogeneous parallel pores. The electrode-electrolyte interface is assumed to be capacitive (modeled with a capacitor), the solid phase is assumed to have infinitely high electronic conductivity, and ion diffusion due to concentration gradients is neglected.[97] In an experiment that satisfies all these assumptions, the ionic resistance R_{ion} can be simply calculated from the cell resistance R_{cell} and the high frequency intercept of the spectrum R_{HFR} as

$$R_{ion} = 3(R_{cell} - R_{HFR}) \tag{3.2}$$

The effective conductivity $\kappa_{e,eff}$ can be calculated from R_{ion} and the geometry of the porous electrode, and Equation 3.1 can be used to determine the tortuosity. This measurement, as with the described approach in this study, is more descriptive than the polarization-interrupt measurement because the latter addresses the shortest ionic pathway rather than the accessibility of the electrochemically active surface area, such as dead-end pores.[98]

Landesfeind et. al. published a comprehensive study of tortuosities in separators and electrodes using the EIS-TLM method, modifying the de Levie model by generalizing the interfacial impedance to a constant phase element (CPE).[74] Malifarge et. al. relaxed the assumption of infinitely high electronic conductivity in the solid phase.[31] Wang et. al. included the impedance of current collectors in the expression for the full cell impedance under blocking conditions.[99]

Experimentally observed deviations from the expected TLM response can complicate the simple extraction of an ionic resistance from the impedance spectra using Equation 3.2. Current collector impedances can result in semicircles in the intermediate frequency range, necessitating fitting of the entire spectra.[99,100] Nguyen et. al. simulated impedance spectra of electrodes reconstructed from tomographic data with varying pore morphologies and showed that deviations from the expected TLM behavior in the high to intermediate frequency region could be explained by considering pores on multiple length scales, as well as "dead-end" pores.[98]

Finally, tortuosity can be extracted from discharge curves using physics-based electrochemical models based on the porous electrode theory developed by Newman.[73,101] A recent study that estimated tortuosity using a coupled multiscale model based on Newman's psuedo-2D (P2D) model showed results consistent with impedance-based measurements and analysis of 3D reconstructed electrodes.[92] This approach has remained relatively unexplored in the literature, likely due to the complexity and relative difficulty of implementation compared to the transmission line model.

In all the above studies, tortuosity is treated as a model parameter that is optimized to fit the experimental observations. However, the uncertainty in the tortuosity estimate that should arise from the fitting of a model to experimental data is rarely reported or discussed in detail. In most cases where error bars in the tortuosity estimate are provided, the error bars represent the sample-to-sample variability and not the uncertainty of an individual measurement.[21,74] When using a model to predict the performance, having a good understanding of the uncertainty in the model parameters, such as tortuosity, is essential in understanding the range of possible outcomes.

In this study, we aim to introduce to the literature a more nuanced attempt to quantify uncertainty in tortuosity estimates for porous electrodes. We describe a procedure to extract tortuosity estimates from standard rate capability experiments using a P2D model. The procedure is validated against synthetic experiments, and a dimensionless group for reducing uncertainty in tortuosity estimates is derived based on the results. The estimation procedure is applied to experimental data for $Li_xV_3O_8$ (LVO) and $Li_xNi_{0.33}Mn_{0.33}Co_{0.33}O_2$ (NMC) electrodes. We continue to discuss the limitations of this procedure and motivate further sources of uncertainty to be explored. Finally, we reexamine published impedance spectra, focusing on quantifying uncertainty in the estimates using the transmission line model, and compare the results to our P2D-based estimation procedure.

3.2 Experimental

3.2.1 Lithium Vanadate

Li1.1V3O8 (LVO) was synthesized via a sol-gel approach as previously reported.[55] Briefly, V_2O_5 and $LiOH$ were used as precursor materials in a stoichiometric ratio of Li:V=1.1:3. The resulting solid was annealed at $500°C$. 3D porous electrodes (3PEs) contained carbon nanotubes (CNTs) and LVO (weight ratios 30:70). The 0.5 inch diameter electrodes were used in coin type cells with Li metal anodes and polypropylene separators prepared in an argon-filled glove box with $1M\ LiPF_6$ in ethylene carbonate/dimethyl carbonate (volume ratio of 3:7) electrolyte. Rate capability experiments were conducted using current rates between C/10 and 2C (1C = 362 mAh/g). Two consecutive cycles were performed at each rate. All cell specifications are listed in Table 3.1.

3.2.2 NMC

NMC Cathodes were cast on 16 μm Al foil with doctor blades using a mixture of NMC111 (MSESupplies LLC), carbon black (Timcal), and PVDF (Arkema Kynar761) at a mass ratio of 90:5:5, dissolved in N-Methyl-2-Pyrrolidone (NMP) (Sigma-Aldrich). The as-casted electrode was heated on a hot plate at $80°C$ for 1 hour, then at $110°C$ for 2 hours to evaporate the NMP solvent.

CR2032 Coin cells were made inside an argon filled glove box. A commercial liquid electrolyte, 1 M $LiPF_6$ in ethylene carbonate/diethyl carbonate (1:1, w/w) (Gotion Inc.) and 25 μm separators (Celgard 2325) were used. 250 μm lithium metal foils were used as the counter electrodes. After assembly, three formation cycles at a C/10 rate were conducted prior to the rate capability experiments, which were performed using Landt and Neware battery testers. In the rate capability experiment, discharge rates ranging from C/5 to 2C were used, with C/5 charge used between each discharge (1C = 150 mAh/g). The slow charge was used to ensure that instability due to lithium plating during charge would not impact the subsequent discharge. Two consecutive cycles were performed at each rate. Cell specifications are listed in Table 3.1.

Table 3.1: Specifications for LVO and NMC cells used in this study.

Electrode	Loading ($mAh\ cm^{-2}$)	Thickness (μm)	Porosity
LVO-1	5.27	441	0.80
LVO-2	5.98	371	0.77
LVO-3	5.79	329	0.75
LVO-4	5.07	156	0.55
LVO-5	9.49	323	0.59
LVO-6	7.82	173	0.37
LVO-7	8.65	230	0.47
NMC-1	3.67	133	0.50
NMC-2	3.91	139	0.50
NMC-3	3.94	131	0.46
NMC-4	4.89	178	0.51
NMC-5	5.17	179	0.48

3.2.3 Bulk Electrolyte Diffusivity Measurements

The electrolyte bulk diffusivity $D_{e,0}$ is a model parameter of the P2D models used in this study, and must be determined to estimate tortuosity (Equation 3.1). A procedure outlined by Gasteiger and coworkers is followed to determine $D_{e,0}$.[94,95]. A pulse experiment was set up using a Swagelok cell assembled in an argon-filled glove box. The cell consisted of layers of Celgard 2325 separators sandwiched between two lithium foil electrodes. The separators were pre-soaked in electrolyte for 12 hours prior to cell assembly.

Two cells were constructed, and six pulse measurements were taken on each cell in a glove box at 25 $^\circ C$. Each pulse experiment consisted of a 120 second galvanostatic pulse of either +1mA or -1mA, after which the open circuit potential of the cell was recorded for one hour. For each cell, three positive current pulses and three negative current pulses were applied in an alternating fashion to discourage the growth of lithium dendrites at either of the electrodes. The region of the recovery used to determine $D_{e,0}$ is delineated by selecting the portion of the recovery where the voltage is between 10 mV and 1 mV of the average voltage at the final minute of the recovery. The slope of the natural log of this region and the distance between the lithium foil electrodes are used to determine D_0/τ. The tortuosity of Celgard 2325, reported as 2.2,[102] is then used to determine $D_{e,0}$.

For the electrolyte used in the NMC cells, 1 M $LiPF_6$ in EC/DEC (1:1, w/w), the bulk diffusivity was determined using to be 1.0×10^{-6} cm^2 s^{-1} using this procedure, consistent with results in the literature for this electrolyte.[103] A transference number of 0.3 was used.[104–106] For the electrolyte used in the LVO cells, 1 M $LiPF_6$ in EC/DMC (3:7 v/v), a transference number of 0.25 and a bulk diffusivity of 2.8×10^{-6} cm^2 s^{-1} were used for simulations, calculated from a bulk conductivity measurement and consistent with previous studies of this electrolyte system, including the work by Gasteiger described above.[95,107]

3.3 Methods

Previously published multiscale mathematical models for LVO and NMC were used in this work[32,108]. Both models follow the structure of the pseudo-2D (P2D) porous electrode paradigm pioneered by Newman[101]. The LVO model couples electrode-scale ion transport to a crystal-scale model that incorporates simultaneous lithiation of two phases as phase transition occurs[32]. The NMC model couples electrode-scale ion transport to an agglomerate-scale model, which has been shown to be in good agreement with experiments.[108]. A description of the electrode-scale equations that are common to both models, and descriptions of the particle-scale equations that are unique to each model are provided in Table 3.3, with the accompanying parameters in Table 3.3 and notation in Table 3.7.

Electrode Scale Equations				
	Governing Equation	Li Anode / Separator interface	Separator / Cathode interface	Cathode / Current collector interface
Solid State Current	$\nabla \bullet i_s = a i_{rxn}$ $i_s = \epsilon_s \sigma \nabla^2 \Phi_s$ LVO: $i_{rxn} = i_{rxn}^{\alpha} + i_{rxn}^{\beta}$	$i_s = 0$	$\nabla \bullet i_e = 0$	$i_s = i_{applied}$
Electrolyte Current	$\nabla \bullet i_e = -a i_{rxn}$ $F i_e = z_+ N_+ + z_- N_-$	$\Phi_e = 0$	$\nabla \bullet i_e = 0$	$i_e = 0$
Electrolyte Concentration	$\epsilon \frac{\partial c_e}{\partial t} = -\nabla \bullet N_+ + \frac{a i_{rxn}}{F}$ $N_+ = \frac{\epsilon_e}{\tau}\left[-D_{e,0}\nabla c_e - \frac{F}{RT} z_+ D_{e,+} c_e \nabla \Phi_e\right]$	$N_+ = \frac{i_{app}}{F}$	$\nabla \bullet N_+ = 0$	$N_+ = 0$
Solid State Concentration	$\epsilon_{AM} \frac{\partial c_s}{\partial t} = -\frac{a i_{rxn}}{F}$			
Particle Scale: NMC (agglomerate)[108]				
	Governing Equation	Particle Center	Particle Edge	
Solid State Current	$\nabla \bullet i_s^{agg} = a^{agg} i_{rxn}^{agg}$ $i_s^{agg} = \epsilon_s^{agg} \sigma \nabla^2 \Phi_s^{agg}$	$i_s^{agg} = 0$	$i_s^{agg} = i_{surface}^{agg}$ $i_{surface}^{agg} = \frac{\partial c_s}{\partial t} \frac{F V_{agg}(1-\epsilon_{agg})}{A_{agg}}$	
Electrolyte Current	$\nabla \bullet i_e^{agg} = -a^{agg} i_{rxn}^{agg}$ $F i_e^{agg} = z_+ N_+^{agg} + z_- N_-^{agg}$	$i_e^{agg} = 0$	$\Phi_e^{agg} = \Phi_e$	
Electrolyte Concentration	$\epsilon \frac{\partial c_e^{agg}}{\partial t} = -\nabla \bullet N_+^{agg} + a^{agg} i_{rxn}^{agg}$ $N_+^{agg} = \epsilon_e^{agg}\left[-D_{e,0}^{agg}\nabla c_e^{agg} - \frac{F}{RT} z_+ D_{e,+}^{agg} c_e^{agg} \nabla \Phi_e^{agg}\right]$	$N_+^{agg} = 0$	$c_e^{agg} = c_e$	
Solid State Concentration	$\epsilon_{AM}^{agg} \frac{\partial c_s^{agg}}{\partial t} = -\frac{a^{agg} i_{rxn}^{agg}}{F}$			
Particle Scale: LVO (crystal)[32]				
Overall Li Balance	$\frac{\partial(c_s^{\alpha}\theta^{\alpha} + c_s^{\beta}\theta^{\beta})}{\partial t} = \theta^{\alpha} D_s^{\alpha} \nabla^2 c_s^{\alpha} + \theta^{\beta} D_s^{\beta} \nabla^2 c_s^{\beta}$	$\nabla c_s^{\alpha} = 0$	$-\theta^{\alpha} D_s^{\alpha} \nabla c_s^{\alpha} = \theta^{\alpha} \frac{i_{rxn}^{\alpha}}{F}$	
Li Balance in β-phase	$\frac{\partial(c_s^{\beta}\theta^{\beta})}{\partial t} = \theta^{\beta} D_s^{\beta} \nabla^2 c_s^{\beta} + c_{s,0}^{\beta} R_{\beta}$	$\nabla c_s^{\beta} = 0$	$-\theta^{\beta} D_s^{\beta} \nabla c_s^{\beta} = \theta^{\beta} \frac{i_{rxn}^{\beta}}{F}$	
Rate of β-phase formation	$R_{\beta} = \frac{\partial \theta^{\beta}}{\partial t} = k_{\beta}(c_s^{\alpha} - c_{s,max}^{\alpha})(1-\theta^{\beta})$			
Electrochemical Reactions[32,108]	$i_{rxn}^{j} = i_0^{j}\left[exp\left(\frac{\alpha_a F \eta}{RT}\right) - \left(\frac{-\alpha_c F \eta}{RT}\right)\right]$	$\eta = \Phi_1 - \Phi_2 - U_j$	$i_0^{j} = f(k_{rxn}^{j}, c_{s,min}^{j}, c_{s,max}^{j}, c_s^{j}, c_e)$	
	j = n/a for NMC, $j = \alpha$ or β for LVO			
Reversible Potentials	See Reference [108] for NMC, Reference [32] for LVO			

Table 3.2: Model equations. Notation can be found in Table 3.7.

Symbol	Value	Units
NMC parameters		
$D_{e,0}$	1.0×10^{-6}	$cm^2\ s^{-1}$
t_+	0.3	
σ	1.0×10^{-2}	$S\ cm^{-1}$
R	5	μm
D_{agg}	12×10^{-10}	$cm^2\ s^{-1}$
k_{rxn}	1.0×10^{-7}	$cm^{5/2}\ mol^{-1/2}\ s^{-1}$
LVO parameters		
$D_{e,0}$	2.8×10^{-6}	$cm^2\ s^{-1}$
t_+	0.25	
σ	1.0×10^{-2}	$S\ cm^{-1}$
R	60	nm
k^{α}_{rxn}	3.0×10^{-8}	$cm^{5/2}\ mol^{-1/2}\ s^{-1}$
k^{β}_{rxn}	2.5×10^{-8}	$cm^{5/2}\ mol^{-1/2}\ s^{-1}$
k_{β}	1.4×10^{-2}	$cm^3\ mol^{-1}\ s^{-1}$
D_{α}	1.0×10^{-13}	$cm^2\ s^{-1}$
D_{β}	7.5×10^{-16}	$cm^2\ s^{-1}$

Table 3.3: Model parameters corresponding to models in Table 3.3. Notation can be found in Table 3.7.

To estimate tortuosity using a given electrode discharged at a given rate, the discharge is simulated using the exact electrode parameters used to prepare the electrode (electrode length, porosity, volume fraction of conductive additive, volume fraction of binder, and active material loading). Both models have been validated against experiments with low-loading electrodes in which performance is dominated by particle-scale effects. This leads to descriptions of electrode kinetic as well as diffusion coefficient through the smaller length scale, along with estimates of associated parameters (primarily exchange current densities and diffusion coefficients). These parameters were not re-estimated, but we explore the impact of their uncertainties on tortuosity estimates in the discussion section. The tortuosity was fit to the experimental discharge capacity. Analysis was also performed by fitting the entire voltage profile. Fits to the entire profile normally yielded the same result, but were sometimes prone to overfitting, returning unreasonable estimates of tortuosity that were not predictive of other discharges for the same cell. More predictive results were obtained when fitting to the discharge capacity As mentioned in the experimental section, analysis of discharge data and not charge data was used for estimation because we restricted the charge rate to C/5 to avoid instabilities that may be caused by lithium plating.

To determine which electrodes and experiments provide confident estimates of tortuosity, synthetic experiments were generated using the validated models. These synthetic experiments were created by evaluating the model in the forward direction, i.e. inputting known tortuosities, outputting voltage curves. Using these synthetic datasets allows us to evaluate the efficacy of the proposed procedure. The LVO model was used to generate synthetic discharge curves for electrodes with thicknesses between 50 μm and 500 μm, and porosities between 0.1 and 0.9. Active material loading was allowed to vary freely, with a conductive additive volume fraction of 5%. Discharge rates between 0.1C and 2C were explored.

In this work, we look to handle parameter estimation and uncertainty quantification from a Bayesian perspective.[109] According to Bayes theorem, the multivariate probability distribution of a set of m parameters $X = [p_1, p_2, ...p_m]$ from a model that is meant to describe data set D is

$$prob(X \mid \{D\}) = \frac{prob(\{D\} \mid X)prob(X)}{prob(\{D\})} \tag{3.3}$$

The left hand side of the equation $prob(X \mid \{D\})$ is referred to as the posterior distribution for the parameters X. On the right hand side, $prob(\{D\} \mid X)$ is called the likelihood, describing the likelihood of observing the data D given a parameter set X. $prob(X)$ represents the prior knowledge of the distribution of the parameters X (called the prior distribution). Finally, $prob(\{D\})$ is the evidence, and can be understood as a rescaling factor for the posterior distribution that does not depend on X.

For the P2D-based tortuosity estimation procedure Bayes theorem can be written as

$$prob(\tau \mid \{Q_k\}) = \frac{prob(\{Q_k\} \mid \tau)prob(\tau)}{prob(\{Q_k\})} \tag{3.4}$$

where Q_k is a capacity measurement at a given rate for a single electrode, and $\{Q_k\}$ is a set of capacity measurements from a rate capability test for that electrode. A uniform prior distribution for tortuosity $prob(\tau)$ is assumed, between 1 and 10 (i.e. our prior knowledge is that tortuosities between 1 and 10 are all equally likely). The likelihood of a tortuosity given an observed capacity is assumed to be normally distributed, with a standard deviation in capacity σ_{Q_k},

$$prob(Q_k \mid \tau) = \frac{1}{\sigma_{Q_k}\sqrt{2\pi}} exp\left(\frac{(Q_{sim}(\tau) - Q_k)^2}{-2\sigma_{Q_k}^2}\right) \tag{3.5}$$

where $Q_{sim}(\tau)$ is the model-predicted capacity for a given tortuosity.

For analysis of synthetic experiments, the experimental uncertainty that characterizes the standard deviation of the normal distribution used in the likelihood function is assumed to be 1.5% of the experimental discharge capacity. An investigation of the dependence of the uncertainty in the tortuosity estimate σ_τ on the assumed experimental variance revealed that reducing the experimental variance by 1% could reduce σ_τ by 0.04. While this analysis was performed on one electrode, the takeaway for the reader is that the uncertainty in the tortuosity estimate can be reduced if the experimental variance can be reduced (i.e. multiple discharges of the same electrode at the same rate are more reproducible).

For analysis of experiment, the experimental uncertainty was evaluated based on the variance in the observed capacity at each rate in the rate capability test, since each rate was done in duplicate. The percent variance in capacity at each rate was averaged over each electrode presented in Table 3.1 for LVO and NMC, and are presented in Figure 3.1.

Tortuosities were estimated from individual discharges to demonstrate the model-guided design rule. However, when estimating tortuosities for a given electrode, results from all discharge rates were used. To this end, each capacity measurement is assumed to be independent, and the likelihood of a set of N capacity measurements $\{Q_k\}$ is given by

$$prob(\{Q_k\} \mid \tau) = \prod_{k=1}^{N} prob(Q_k \mid \tau) \tag{3.6}$$

Though the assumption of consecutive capacity measurements in a rate capability test being independent is not entirely true, we justify this approximation with the use of slow charges between consecutive discharges.

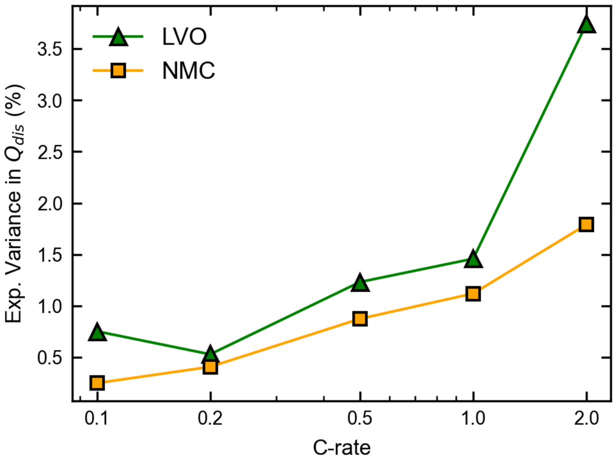

Figure 3.1: Percent variance in discharge capacity for LVO and NMC, calculated based on the average percent variance in discharge capacity for the cells in Table 3.1.

When analyzing the experimental data, we found that the LVO model was not able to describe the experiments well at rates above 1C. The root mean squared error in voltage over the course of a discharge exceeded 50 mV, indicating that some other model parameters need to be tuned to accurately describe the high rate data. Therefore, only experimental data generated at rates below 1C are reported. Further discussion on impact of including other model parameters in the estimation procedure is provided below.

3.4 Results and Discussion

3.4.1 Analysis of Synthetic Experiments

Three representative synthetic experiments are summarized in Table 3.4 and Figure 3.2. The black dashed lines in Figure 3.2 represent the simulated discharge profile for each synthetic experiment. The model was used to predict discharge for the same electrode (using the thickness, porosity, and C-rate), but the tortuosity was allowed to vary between 1 and 10. The predicted discharge profiles while varying the tortuosity are shown by the colored lines in Figure 3.2. Examining each successive panel in Figure 3.2, it is apparent that the sensitivity of the model to tortuosity varies greatly. In Figure 3.2a, there is no difference in the predicted discharge profile whether $\tau = 1$ or $\tau = 10$. For the electrode in Figure 3.2b, the predicted discharge profile does not vary for τ between 1 and 3, but for τ greater than 3 the predicted discharge profile starts to vary significantly. For the electrode in Figure 3.2c, the model is highly sensitive to even small changes in τ.

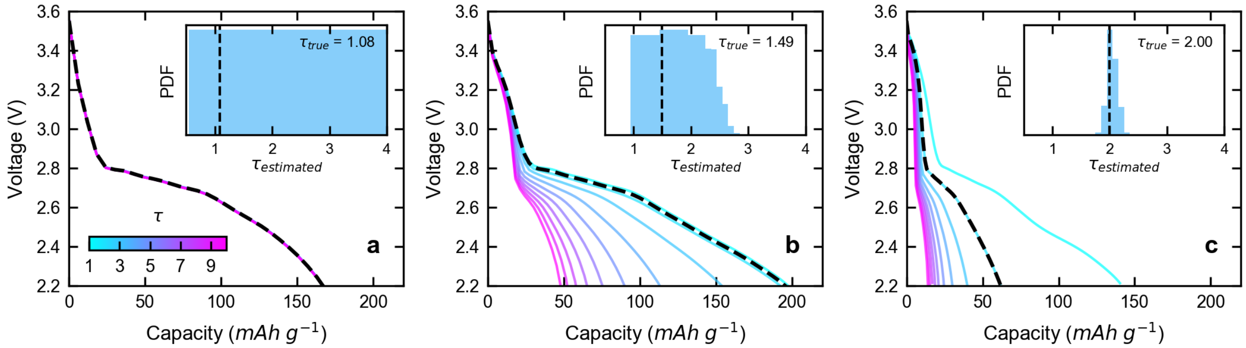

Figure 3.2: Tortuosity estimation for three representative synthetic experiments. Specific parameters describing each experiment are presented in Table 3.4. Dashed black lines represent simulated behavior of electrodes at a given discharge rate, and colored lines represent predicted response of those electrodes while varying the tortuosity in the model (color bar in 1a applies to all). Insets show probability distribution of estimated tortuosity and the true tortuosity of the synthetic electrode from the parameter estimation.

Table 3.4: Summary of parameters used to generate representative synthetic experiments shown in Figure 3.2, along with tortuosity estimation results. Uncertainties for $\tau_{estimated}$ are one standard deviation.

	L (μm)	ϵ_e	C_r (h^{-1})	τ_{true}	$\tau_{estimated}$
Fig 1a	50	0.84	1	1.08	5.5 ± 2.9
Fig 1b	200	0.45	0.5	1.49	1.7 ± 0.5
Fig 1c	400	0.25	2	2.00	2.0 ± 0.1

These differences in model sensitivity can be leveraged to obtain distributions for τ, shown in the insets of Figure 3.2. When the model is insensitive to tortuosity, tortuosity cannot be estimated with any degree of confidence. However, when the model is very sensitive to tortuosity, it can be estimated with a high degree of confidence. For the electrode shown in Figure 3.2c, τ can be estimated to within 0.1. The uncertainties (one standard deviation) are tabulated for each electrode in Table 3.4.

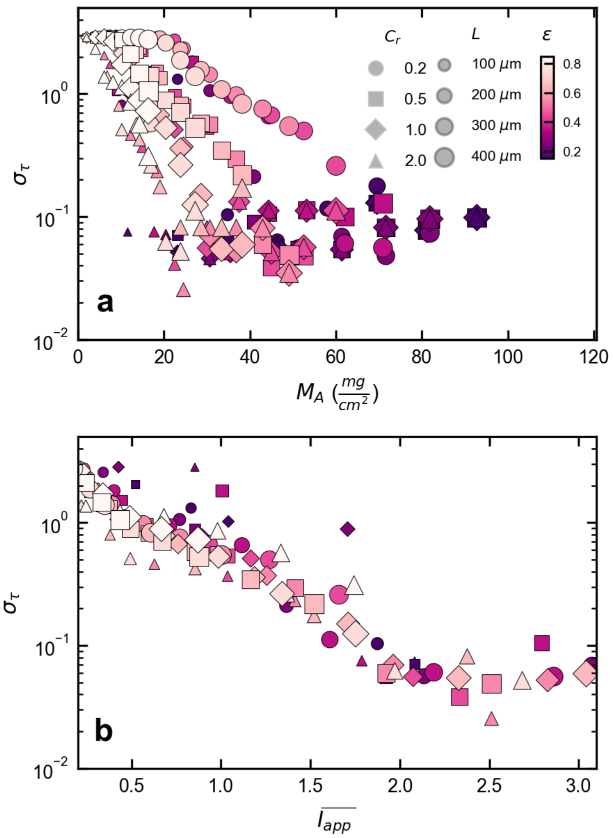

Figure 3.3: Uncertainty in estimated tortuosity σ_τ versus mass loading for model-generated LVO experiments as a function of mass loading (**a**) and dimensionless current (**b**).

To develop a rule for designing experiments to measure tortuosity with confidence, we consider a range of LVO electrodes and their simulated discharge at various rates in Figure 3.3. As indicated by the legend inset in Figure 3.3a, these sets of synthetic experiments contain electrodes with different thicknesses (size) and porosities (color) whose discharge is simulated at different rates (shape). The uncertainty in the estimate of tortuosity for the synthetic experiments are plotted against the loading in Figure 3.3a. Some general trends are observed: higher loading electrodes (thicker, less porous) give more confident tortuosity estimates, and there appear to be distinct curves for each C-rate. These results demonstrate that when a higher ion transport impedance exists on the electrode scale, more can be learned about the tortuosity.

To better summarize results, we turn to porous electrode theory, specifically to the governing equation that describes the mass balance for lithium ions in the electrolyte. A simplified form assuming transport is dominated by diffusion rather than migration is presented.

$$\epsilon_e \frac{\partial c_e}{\partial t} = \frac{\epsilon_e D_{e,0}}{\tau} \frac{d^2 c_e}{dx^2} + \frac{a i_n}{F} \tag{3.7}$$

where ϵ_e is the porosity, c_e is the salt concentration in the electrolyte, $D_{e,0}$ is the bulk salt diffusion coefficient in the electrolyte, a is the active surface area per unit volume, and i_n is the local reaction current density. The spatial average of the local current density must equal the applied current density at the current collector I_{app}, which is related to the C-rate C_r and the capacity loading Q_A ($mAh\ cm^{-2}$) by

$$\overline{a i_n} L = I_{app} = C_r Q_A \tag{3.8}$$

The salt concentration, time, and length can be nondimensionalized as follows:

$$\overline{c} = \frac{c_e}{c_{e,bulk}} \tag{3.9}$$

$$\overline{t} = t C_r \tag{3.10}$$

$$\overline{x} = \frac{x}{L} \tag{3.11}$$

where $c_{e,bulk}$ is the bulk salt concentration in the electrolyte. Substituting equations 3.8-3.11 into equation 3.7, and assuming a pseudo-steady state, we arrive at the result

$$\frac{d^2 \overline{c}}{d\overline{x}^2} = \frac{C_r Q_A L \tau}{\epsilon D_{e,0} c_{e,bulk} F} = \overline{I_{app}} \tag{3.12}$$

We denote the dimensionless group here as $\overline{I_{app}}$, a dimensionless applied current. This dimensionless current follows a formulation similar to a diffusion-limited C-rate proposed by Heubner et. al.[110].

To test the applicability of $\overline{I_{app}}$ in predicting experiments that will give confident tortuosity estimates from fitting to discharge curves, we replot the results in Figure 3.3a in Figure 3.3b. As we do not know the value of the tortuosity τ beforehand, the Bruggeman relation ($\tau = \epsilon_e^{-0.5}$) is used. All the results collapse onto a common curve, indicating that $\overline{I_{app}}$ can be used to guide design of experiments. Small deviations from the curve are likely due to transport impedances on the smaller scales that may still be relevant at high rates.

Physically, $\overline{I_{app}}$ has multiple relevant interpretations. One interpretation is the ratio of the applied current at the current collector to the limiting current in the porous electrode, i.e. the current at which the salt at the current collector is depleted.

$$\overline{I_{app}} = \frac{I_{app}}{I_{lim}} = C_r Q_A \left(\frac{\epsilon_e D_{e,0} c_{e,bulk} F}{\tau L} \right)^{-1} \tag{3.13}$$

In this case, as the applied current approaches and exceeds the limiting current, more confident estimates of tortuosity can be obtained. Another interpretation is a modification on a dimensionless number proposed by Doyle et. al. S_e[101], which compares the characteristic diffusion time to the C-rate:

$$S_e = C_r \left(\frac{L^2 \tau}{\epsilon_e D_{e,0}} \right) \tag{3.14}$$

By factoring out S_e from $\overline{I_{app}}$, an additional dimensionless group emerges, which describes the capacity available in the active material relative to the lithium inventory in the electrolyte.

$$\overline{I_{app}} = S_e \left(\frac{Q_A}{c_{e,bulk} L F} \right) \tag{3.15}$$

While some analyses of rate performance of electrodes rely on the analysis similar to that presented by Doyle et. al.[111], this result emphasizes the importance of also considering the lithium inventory in the electrolyte when considering ion transport impedances in porous electrodes[110,112].

It is noted that though an assumption is made about the tortuosity to identify experiments that will give confident estimates of tortuosity, if the true tortuosity is higher (as is the case for most active materials), the trend of experiments with high values of $\overline{I_{app}}$ giving more confident estimates will hold.

3.4.2 Analysis of Experiments

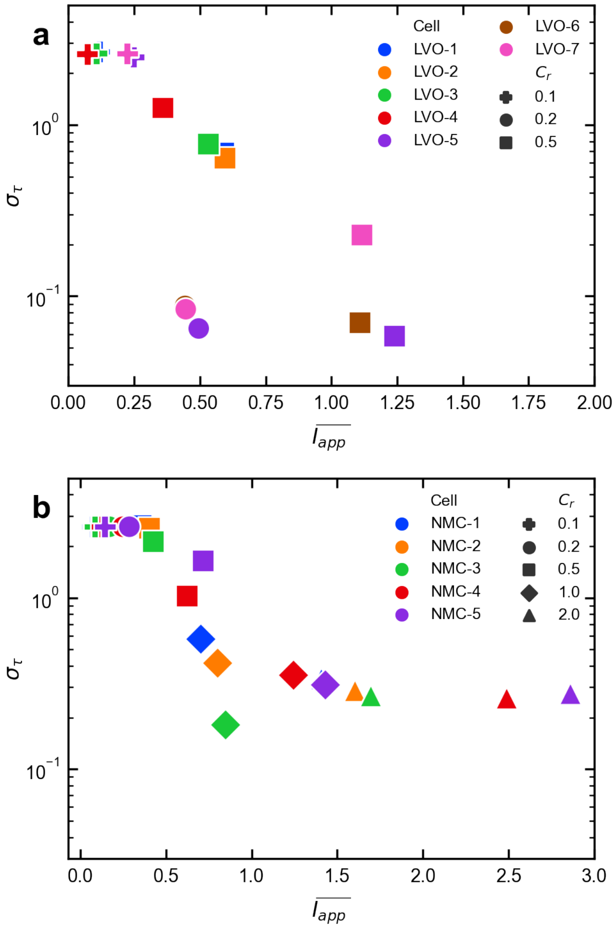

Figure 3.4: Uncertainty in estimated tortuosity σ_τ versus mass loading for real LVO (a) and NMC (b) experiments as a function of $\overline{I_{app}}$., overlaid on results for model-generated analysis from Figure 3.3b.

When estimating tortuosity of the fabricated electrodes that underwent rate capability tests, instead of assuming a constant experimental variance in capacity of 1.5% as was done in Figure 3.3, the experimentally derived experimental variance presented in Figure 3.1 was used. Each individual discharge rate was analyzed separately to evaluate the effectiveness of $\overline{I_{app}}$ as a design rule (Figure 3.4). As expected, experiments that have a higher value of $\overline{I_{app}}$ yield more confident estimates in tortuosity. Some deviations from the expected trend from Figure 3.3b are observed in the analysis experimental data. This can be attributed to increasing experimental variance with discharge rate, which yields less confident estimates than expected at high rates for the same electrode.

The above discussion has been restricted to reducing uncertainty in the tortuosity estimate. We next examine the values of the tortuosity estimates themselves. When estimating the tortuosity for an electrode, all the measured capacities from the discharge are used to form a set $\{Q_k\}$, and the posterior distribution for tortuosity is evaluated using Equations 3.4-3.6. This is because in some cases the highest rate may not yield the lowest uncertainty (Figure 3.4) due to higher experimental error at high rate, and the most probable value of the tortuosity estimate may shift as a function of c-rate. The estimated tortuosity should describe the observed discharge capacity of an electrode at all rates.

Tortuosity estimates for the set of LVO electrodes used in this study and plotted in Figure 3.5a. To analyze the tortuosity dependence on porosity, a Bruggeman-type model is fit to the data, as is done by Thorat et. al.[93]

$$\tau = \gamma \epsilon_e^{\alpha} \tag{3.16}$$

In the literature, a relationship like the one above is often fit to measurements at different porosities, and values for γ and α are reported.[31,74,88,93] However, most electrodes are fabricated with porosities above 0.3, where this Bruggeman-type model is not distinguishable from a variety of other correlations.[113] To further establish this point, we estimated γ and α in the Bruggeman-type model given our tortuosity estimates for electrodes with different porosities. The posterior distribution for γ and α takes the form of a bivariate normal distribution, with a likelihood function that assumes each tortuosity estimate τ_k follows a normal distribution $\mathcal{N}(\mu_{\tau_k}, \sigma_{\tau_k}^2)$. The values of

μ_{τ_k} and $\sigma^2_{\tau_k}$ are determined individually from the P2D estimation procedure described above.

$$prob(\gamma, \alpha \mid \{\tau_k\}) = \frac{prob(\{\tau_k\} \mid \gamma, \alpha) prob(\gamma, \alpha)}{prob(\{\tau_k\})} \tag{3.17}$$

$$prob(\{\tau_k\} \mid \gamma, \alpha) = \frac{1}{\sigma_{\tau_k}\sqrt{2\pi}} exp\left(\frac{(\gamma \epsilon_k^{\alpha} - \mu_{\tau_k})^2}{-2\sigma^2_{\tau_k}}\right) \tag{3.18}$$

The prior $prob(\gamma, \alpha)$ is chosen to be uniform, in the ranges [1,10] and [0,-1] for γ and α respectively, and each measurement is independent, such that $prob(\{\tau_k\} \mid \gamma, \alpha)$ is merely the product of the likelihood for each measurement, similar to Equation 3.6.

The results are presented in Figure 3.5b. It appears that for LVO the Bruggeman relationship underestimates tortuosity for LVO, as has been found for a variety of other materials.[73,74,88,91–93] The solution for the posterior distribution (Equation 17) is presented in Figure 5b. Since it is a bivariate normal distribution, each variable is shown on the x and y axis and the probabilities of observing combinations of the two variables is shown using a contour map. Given the measurements made for the electrodes in this study, the exponent α cannot be known with much certainty (relative to the chosen priors) compared to the prefactor γ. Measurements would need to be made at much lower porosities to pin this exponent down. Even if this is done, electrodes of similar porosities yield different tortuosities due to sample-to-sample variance, indicating that a large number of electrodes would need to be prepared and measured to extract any meaningful tortuosity porosity relationship. We emphasize that the focus of this study is to quantify and systematically reduce the measurement uncertainty for a given electrode, and not to establish a tortuosity-porosity relationship.

The tortuosity estimates for the NMC electrodes in this study are shown in Figure 3.6a, alongside estimates for NMC electrodes in the literature for context. Measurements using the EIS-TLM method are shown in yellow, measurements from XCT are shown in red, and measurements using the P2D model-fitting approach are shown in cyan. Results analyzed in this paper are outlined in black. Each of these studies used electrodes with different materials, recipes, and fabrication processes, all of which will influence tortuosity. Details for each of the measurements shown in

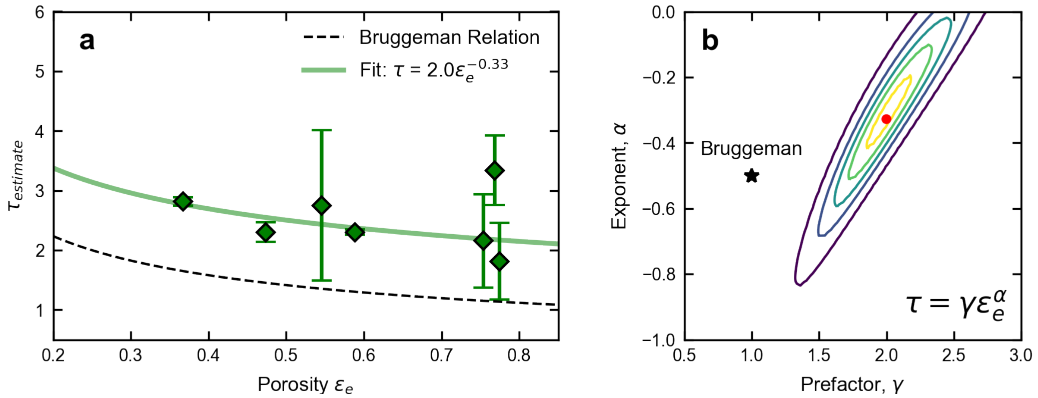

Figure 3.5: Tortuosity estimates for LVO electrodes at different porosities, compared to the Bruggeman relation (a). Contour map of the bivariate distribution for the two parameters γ and α in the Bruggemean-type model (b). Contours correspond to 10%, 30%, 50%, 70%, and 90% of the peak of the joint distribution (red).

the plot are included in Table 3.5.

Electrodes prepared in this study for measurement all have porosities between 0.45 and 0.55. Though less porous electrodes were not fabricated, we applied our tortuosity estimation procedure to data from another study where rate capability results were published for a high loading (72 $mg\ cm^{-2}$) NMC111 electrode, and the result is included in Figure 6 as well.[114] Possible reasons for the difference between the results reported here and those reported in the literature include the different electrode compositions,[90] heterogeneity in cell fabrication,[115] and sample to sample variance. In addition, the accuracy of our estimates is subject to some assumptions made in the model development, which are discussed further in the next section.

The results of the parameter estimation for the Bruggeman-type relationship for the NMC tortuosity estimates are shown in 3.6b. In evaluating the joint posterior distribution for γ and α, only estimates with an uncertainty reported were used. The results reveal a stronger covariance of α with γ, and given the variation in the different measurements, the prefactor γ can be known with even less confidence compared to LVO. These attributes of the joint distribution are not properties of the materials themselves, but rather artifacts of the data available.

Figures 3.5b and 3.6b indicate that the community should exercise caution in using Bruggeman-type models for tortuosity, since these models are not very identifiable (that is, γ and α cannot be identified with certainty). A more fundamental understanding of tortuosity's dependence on microstructural properties of an electrode may arise from studies that derive tortuosity from the microstructure itself (i.e. XCT, FIB-SEM), and consider factors like particle anisotropy and elongation effects.[21] Methods like the one discussed here or the EIS-TLM method may require many more experiments than are currently done in the literature to overcome the sample-to-sample variance problem and tease out such a fundamental understanding of tortuosity's dependence on microstructure.

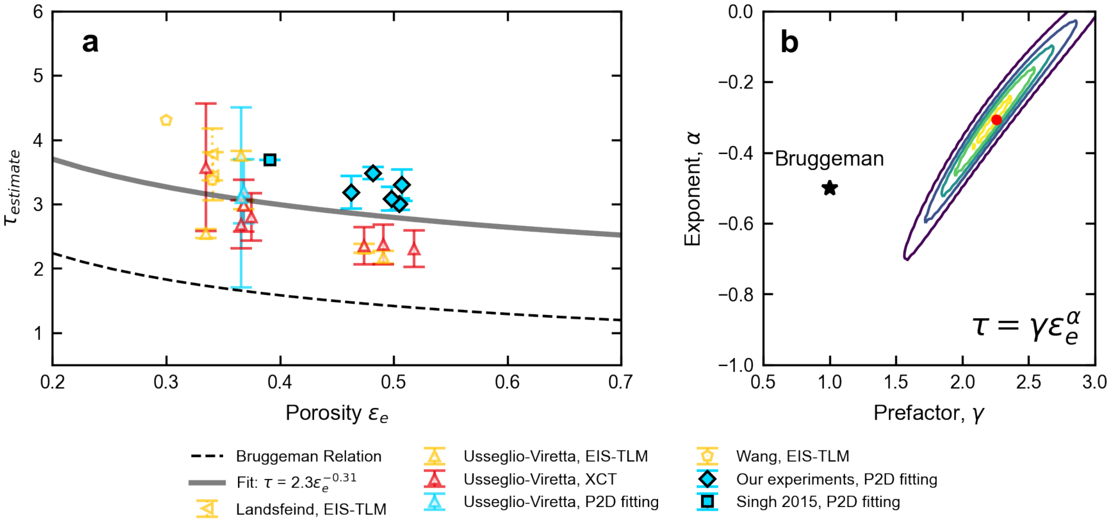

Figure 3.6: Tortuosity estimates for NMC electrodes in this study (bold outline) and studies in the literature (a). Contour map of the bivariate distribution for the two parameters γ and α in the Bruggemean-type model (b). Contours correspond to 10%, 30%, 50%, 70%, and 90% of the peak of the joint distribution (red).

3.4.3 Consideration of Other Model Uncertainties

The procedure described above for extracting tortuosities from experiments using a P2D model relies on the existence of a validated physics-based model on the particle scale. Though only one model parameter - the tortuosity - is being fitted, the uncertainties being reported assume other model parameters are known exactly, which is of course not the case. Our previous studies quantified the uncertainties associated with kinetic and transport related parameters (reaction rate constants for lithium insertion, lithium diffusion in the active material) for particle-scale models.[32,108]

Table 3.5: Specifications for various studies measuring tortuosity for NMC electrodes. Results of the studies are shown in Figure 3.6.

Ref.	Author	Method	Active Material	Electrode Recipe	Uncertainty Source
[74]	Landesfiend	EIS-TLM	NMC111	96:2:2 AM:PVDF:C65	Thickness Measurement
[92]	Usseglio-Viretta	EIS-TLM	NMC532	96:2:2 AM:PVDF:C65	Measurement to measurement variance
[92]	Usseglio-Viretta	XCT	NMC532	90:5:5 AM:PVDF:C65	CBD distribution, numerical error, ϵ error
[92]	Usseglio-Viretta	P2D fiting	NMC532	90:5:5 AM:PVDF:C65	Model sensitivity
[99]	Wang	EIS-TLM	NMC111	90:5:5 AM:PVDF:C65	not reported
	This paper	P2D fiting	NMC111	90:5:5 AM:PVDF:C65	Model sensitivity
[114]	Singh	P2D fiting	NMC111	90:3:3:4 AM:PVDF:C65: graphite	Model sensitivity

In this section, we provide an example of an analysis that incorporates uncertainty in other model parameters by considering the effects of charge transfer kinetics and particle-scale transport parameters on the reported tortuosity uncertainties. We proceed to discuss other model parameters and assumptions that could impact both the precision and accuracy of estimates using the method described here.

Let us consider the active surface area per unit volume for charge transfer reaction. In many P2D models where the active material is assumed to be spherical in shape, the surface area per volume is defined as

$$a_t = \frac{3\overline{\epsilon}_{AM}}{R} \tag{3.19}$$

where a_t denotes the theoretical relationship, $\overline{\epsilon}_{AM}$ is the volume fraction of active material, and R is the particle radius. This relation, developed for non-overlapping spheres, overestimates the true active surface area when spherical particles overlap.[69,91]. Conductive additives and binders further reduce the active surface area.[116,117] In P2D models, the active area per volume a always appears alongside an exchange current density (Table 3.3). Uncertainty in the active surface area available for charge transfer can therefore can also be interpreted as uncertainty in exchange current density. Ultimately, both represent uncertainty surrounding the charge transfer resistance.

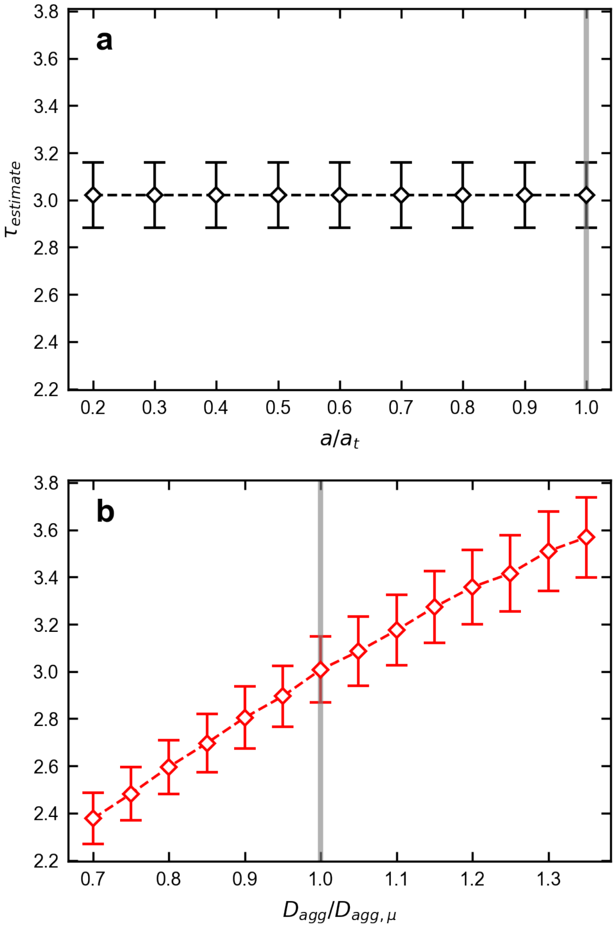

Figure 3.7: Analysis of a 2C discharge of electrode NMC-5. Tortuosity estimates with different assumptions about the amount of active surface area available for charge transfer (a). Tortuosity estimates for different assumptions about the value of D_{agg} (b).

To understand sensitivity of the tortuosity estimate to the charge transfer resistance, the estimation was repeated for different values of a/a_t, a normalized modification factor to the surface area as determined by equation 3.19 (Figure 3.7a). As the surface area is reduced, the charge transfer resistance increases and the average voltage during a 2C discharge changes, but the absolute capacity used to fit the tortuosity remains unchanged. Over one order of magnitude, the estimate is not sensitive to the surface area, indicating that this uncertainty does not impact the uncertainty in the tortuosity estimate.

A second source of uncertainty in the model is the particle-scale diffusivity. In the context of NMC, this is the diffusivity of lithium ions through spherical NMC agglomerates. The notation from Table 3.3, $D_{e,0}^{agg}$, is translated to D_{agg} here for simplicity. Based on the results in our previous study of NMC, the D_{agg} is known to within ±30%.[108] The mean value $D_{agg,\mu}$ is 12×10^{-10} $cm^2 s^{-1}$. Values from 8 to 16 $\times 10^{-10}$ $cm^2 s^{-1}$ are considered here, and the analysis is presented in Figure 3.7b. A covariance is observed between tortuosity and D_{agg}. As D_{agg} increases, the model predicts better utilization of the active material. As a result, a higher tortuosity must exist in the porous electrode to explain the lower delivered capacity at the end of discharge.

Given this covariance, one would expect the uncertainty in tortuosity to increase if the assumption of an exactly known value of D_{agg} is relaxed. Figures 3.8a and b compare the conditional distribution for tortuosity $\text{prob}(\tau \mid \{Q_k\}, D_{agg,\mu})$, which assumes exact knowledge that $D_{agg} = D_{agg,\mu}$, and the marginal distribution $\text{prob}(\tau \mid \{Q_k\})$, which assumes D_{agg} is onlu known to within ±30% by marginalizing the multivariate posterior distribution over D_{agg}. This comparison is made for results at both 1C and 2C. At 1C, we see a slight widening of the distribution when marginalizing over D_{agg}. At 2C, we see that the marginal distribution spreads significantly, and confidence in the estimate is lost. This result serves as an important caution to the design rule of reducing $\overline{I_{app}}$ presented earlier. Though electrode-scale ion transport impedance becomes more dominant at high rate, particle-scale diffusion impedance also becomes more important. As a result, analyzing the 2C discharge proves less valuable than analyzing the 1C result. This result emphasizes the importance of analyzing multiple rates simultaneously for a given electrode when estimating tortuosity using this method. The marginal and conditional distribution as determined by analyzing all rates for a rate capability test for NMC-5 is presented in Figure 3.8c. Similar uncertainties are obtained, but the means of the distributions are different.

The model predicted rate capability is compared to the experimental rate capability in 3.8d to confirm that the fitted models predict the rate performance well. The distributions for τ and D_{agg} can be translated to a range of model predictions for rate performance, shown in the shading in 3.8b. As discussed previously, the range of model predictions increases at higher rates, since ion transport on the electrode scale and the agglomerate scale become more limiting at higher rates.

While we motivate the need for detailed uncertainty analysis using the two examples described above, the impact of several other model parameters and assumptions remains unexplored. For instance, concentration dependence of $D_{e,0}$, t_+, and $\kappa_{e,0}$ is not considered in the model described in Table 3.3. Since the proposed procedure intentionally induces concentration gradients, the exclusion of concentration dependence of these parameters will affect the accuracy of the results. A more thorough analysis should incorporate functions for these properties as a function of concentration, as has been reported by Valoens and Reimer,[107] but would require uncertainties in these functions as well, which were not reported. Future work could incorporate these functions and their associated uncertainties into the analysis. In addition, uncertainties in the other model parameters in Table 3.3 could be explored.

Though our estimates may suffer from some inaccuracy because of the aforementioned model simplifications, the systematic improvement of precision through design of experiments still holds. Inclusion of other model complexity and parameter uncertainties may cause the results in Figures 3 and 4 to shift upwards to higher values, but the reduction in uncertainty with $\overline{I_{app}}$ will remain.

3.5 Uncertainty Analysis for EIS

Electrochemical impedance spectra were taken from Wang et. al.'s study of various porous electrodes to perform an uncertainty analysis on the values of tortuosity extracted.[99] Wang et. al. study a variety of electrodes, including NMC, LCO, LFP, LTO, and graphite. Both Nyquist and

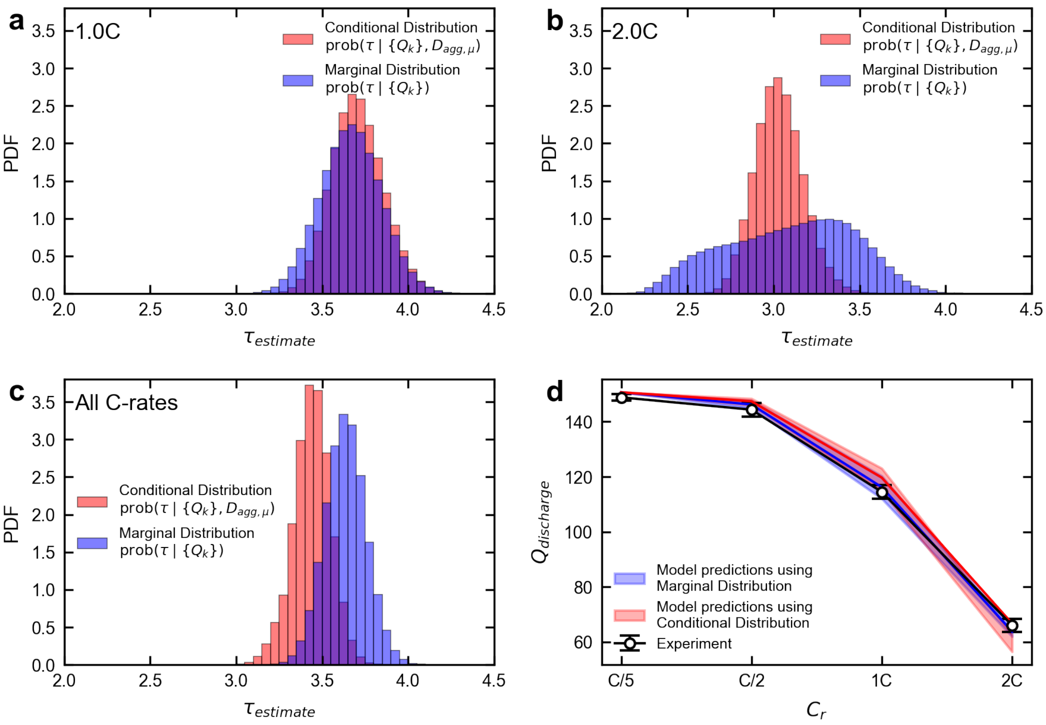

Figure 3.8: Analysis of electrode NMC-5, comparing tortuosity estimates conditioned on $D_{agg} = D_{agg,\mu}$ (red) to estimates that marginalize over a 30% range of D_{agg} (blue). All c-rates were used to fit tortuosity. Results are presented for an analysis of the 1C discharge capacity (a), the 2C discharge capacity (b), and all discharge capacities between 0.1C and 2C (c). The model predictions for capacity at various rates considering both cases are compared to the experimental rate capability in (b). The shaded region correspond to model predictions for two standard deviations above and below the mean parameter estimates, and the error bars on the experimental points are the assumed experimental variance.

Bode plots were provided for select NMC, LCO, LFP, and LTO electrodes in the appendix of Reference[99]. Only the NMC and LCO electrodes were included in our analysis because only those electrodes met all the assumptions of the TLM used by Landesfiend et al. (namely that electronic resistance was negligible relative to ionic resistance). Data from the Bode plots were extracted using WebPlotDigitizer[118] and converted to complex numbers to get the complex impedance.

The equivalent circuit model (ECM) used to fit the impedance spectra is shown in Figure 9. The impedance of the cell (Z_{cell}, Equation 3.20 is the summation of the high frequency resistance (R_{HRF}), the impedance of the porous electrode, and the impedance of the current collector (subscript cc). The reader is referred to Reference[99] for further details on the definition of the ECM.

$$Z_{cell} = R_{HFR} + Z_{electrode}(R_{ion}, Q_{CT}, \gamma_{CT}) + Z_{cc}(R_{cc}, Q_{cc}, \gamma_{cc}) \tag{3.20}$$

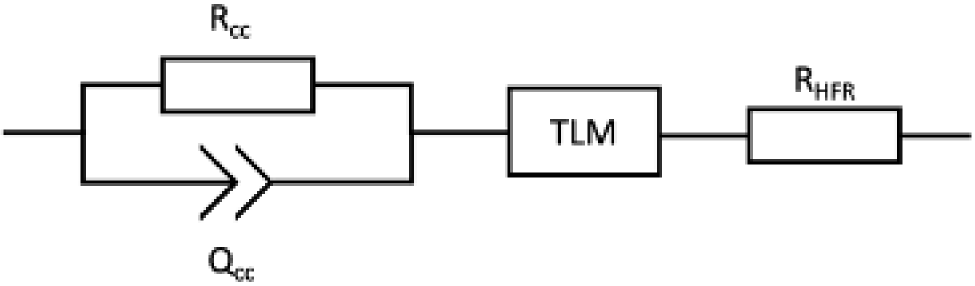

Figure 3.9: Equivalent circuit model used to interpret impedance spectra from Reference[99].

In total the equivalent circuit model in Figure 3.9 contains 7 parameters, listen in Table 6. The value of the ionic resistance in the electrode R_{ion} can be mapped to a tortuosity by

$$\tau = \frac{R_{ion} A \kappa_{e,0} \epsilon_e}{2L} \tag{3.21}$$

where A is the electrode cross sectional area and L is the electrode length, with a factor of two present because a symmetric cell was assembled.

Quantifying uncertainty in the parameter estimates for the transmission line model can be framed using Bayes Theorem, as was done for the P2D-based estimation procedure (Equation

3.4). Here, the 7 parameters of the model are represented by X, and the posterior distribution for X is a multivariate distribution given by Equation 3.23.

$$X = [R_{HFR}, R_{cc}, Q_{cc}, \gamma_{cc}, R_{ion}, Q_{CT}, \gamma_{CT}] \tag{3.22}$$

$$prob(X \mid Z_{cell}) = \frac{prob(Z_{cell} \mid X)prob(X)}{prob(Z_{cell})} \tag{3.23}$$

Analogous to Equations 3.5 and 3.6, the likelihood of observing the impedance spectrum Z_cell given a set of parameters X is given by

$$prob(Z_{cell} \mid X) = \prod_{k=1}^{N_\omega} prob(ReZ_{cell}(\omega_k) \mid X)prob(ImZ_{cell}(\omega_k) \mid X) \tag{3.24}$$

$$prob(ReZ_{cell}(\omega_k) \mid X) = \frac{1}{\sigma_{ReZ_{cell}}\sqrt{2\pi}} exp\left(\frac{(ReZ^{sim}_{cell}(X,\omega_k) - ReZ_{cell}(X,\omega_k))^2}{-2\sigma_{ReZ_{cell}}}\right) \tag{3.25}$$

$$prob(ImZ_{cell}(\omega_k) \mid X) = \frac{1}{\sigma_{ImZ_{cell}}\sqrt{2\pi}} exp\left(\frac{(ImZ^{sim}_{cell}(X,\omega_k) - ImZ_{cell}(X,\omega_k))^2}{-2\sigma_{ImZ_{cell}}}\right) \tag{3.26}$$

where $Z^{sim}_{cell}(X,\omega_k)$ is the model-predicted impedance at frequency ω_k given X, $\sigma_{Z_{cell}}$ is the experimental variance of the observed spectrum, Re and Im denote the real and imaginary components of Z, and N_ω is the number of frequencies over which the impedance spectrum was collected. Since the experimental variance could not be calculated from the given data, a value of 5 Ω is assumed for both $\sigma_{ReZ_{cell}}$ and $\sigma_{ImZ_{cell}}$. As mentioned previously, increasing this value will have the effect of widening the posterior distribution.

The posterior distribution is evaluated by using the open-source python package impedance.py,[119] which allows the user to build custom circuits with common circuit elements, including the TLM

Table 3.6: Parameter estimation results for ECM in Figure 3.9, including uncertainties. The final row shows the tortuosity estimate. Results are compared to those reported in Reference[99].

	NMC		LCO	
	Parameter estimate	Wang et. al.	Parameter estimate	Wang et. al.
R_{HFR}	60.8 ± 1.5	43.5	81.4 ± 1.7	36.9
R_{cc}	63.3 ± 2.6	70.2	89.9 ± 2.6	95.3
Q_{cc}	23.1 ± 5.5	31.3	17.8 ± 3.3	21.3
γ_{cc}	0.74 ± 0.03	0.7	0.68 ± 0.02	0.66
R_{ion}	158.2 ± 5.7	177.5	302.0 ± 6.1	365.9
Q_{CT}	0.66 ± 0.07	0.6	0.70 ± 0.02	0.7
γ_{CT}	0.92 ± 0.001	0.92	0.95 ± 0.002	0.94
$\tau_{estimate}$	3.18 ± 0.11	3.37	3.17 ± 0.06	3.66

in Reference[74]. Though we did not simulate impedance spectra using sets of X that spanned a 7-dimensional prior, the distributions that are output from the curve fitting function in impedance.py (built on scipy's curve fit) can be interpreted as the posterior distribution. Code for reproducing this parameter estimation is available on github.com/karthikmayil/EIS-uncertainty-analysis.

A distribution can be obtained for each individual parameter by marginalizing over the other 6 parameters. The mean values and uncertainties for each of these distributions (taken from the diagonal of the covariance matrix of the multivariate posterior distribution) are reported in Table 3.6, alongside the estimates by Wang et al., where uncertainties are not provided. The uncertainty in the tortuosity is calculated directly from the percentage uncertainty in R_{ion}, since the two are linearly related via Equation 3.21. Some discrepancy can be expected because of error in the data extraction and because the fitting by Wang et. al. included an extra parameter, the electronic resistance, which is neglected in our simplified model. Still, our results are close to those obtained by Wang et al., with the added benefit of quantifying the uncertainty associated with the tortuosity.

Based on this analysis, it appears that interpretation of EIS spectra collected under blocking conditions and interpreted with an equivalent circuit model that includes a TLM circuit element can obtain estimates of tortuosity that are as confident as, if not more confident than, those obtained by the P2D-based method described in this paper. The difference between the methods may be amplified if the limitations outlined in the previous section are addressed.

3.6 Conclusion

In this study, we have presented a comprehensive analysis of model-guided design of experiments and limitations of using a P2D physics-based model to estimate tortuosities from constant current discharge curves. A dimensionless current derived from porous electrode theory is used to guide the design of experiment to reduce uncertainty in tortuosity estimates by identifying when P2D models are sensitive to the tortuosity model parameter. Tortuosity estimates are reported for LVO and NMC electrodes. Analysis of the Bruggeman-type model for tortuosity dependence on porosity reveal that the prefactor and exponent in this model are not identifiable, indicating that they should be used with caution. A detailed discussion is provided on assumptions and limitations of the method, motivating the consideration of uncertainty in other model parameters when estimating tortuosity. Finally, an uncertainty analysis on an ECM for standard EIS spectra under blocking conditions is performed, resulting in comparable values of uncertainty to those obtained by our P2D method. We hope this study motivates others to consider reporting uncertainties in their estimates of tortuosity.

3.7 Supplementary Information

Table 3.7: List of symbols and notation.

Symbol	**Description**	**Units**
a	Electrochemically active surface area	cm^{2} cm^{-3}
c	Concentration	mol cm^{-3}
C_r	C-rate	h^{-1}
D	Diffusivity	cm^{2} s^{-1}
ϵ	Volume fraction	
η	Overpotential	V
F	Faraday's Constant	96485 C mol^{-1}
i	Current Density	A cm^{-2}
k	Rate constant	varies
κ	Ionic conductivity	S cm^{-1}
n	Flux	mol cm^{-2} s^{-1}
Φ	Potential	V
σ	Electronic conductivity	S cm^{-1}
t	Time	s
θ	Phase volume fraction	
U	Reversible Potential	V

	Superscripts and Subscripts
AM	Active material
agg	Agglomerate (NMC)
α	α-phase (LVO)
β	β-phase (LVO)
e	Electrolyte
max	Maximum concentration
min	Minimum concentration
rxn	Electrochemical reaction
s	Solid phase
sat	Saturation concentration

Chapter 4

Understanding Evolution of $Li_xV_3O_8$ Cathodes During Cycling via Reformulated Physics-Based Models and Experiments*

---

*This chapter has been published: Karthik S. Mayilvahanan, Jason Kuang, Alison H. McCarthy, Lei Wang, Kenneth J. Takeuchi, Amy C. Marschilok, Esther S. Takeuchi, Alan C. West, "Understanding Evolution of Lithium Trivanadate Cathodes During Cycling via Reformulated Physics-Based Models and Experiments," *Journal of the Electrochemical Society.*, vol. 168, no. 5, p. 050525, May 2021.
The thesis writer's contribution was physics-based model analysis, experimental design, and writing. The electrochemical observations and characterization were provided by Jason Kuang and Alison McCarthy from the Marschilok-Takeuchi Research Group at Stony Brook University.

4.1 Introduction

Vanadium based materials have garnered interest as active material candidates for cathodes in Li-ion batteries due to their capability for multiple electron transfers within a desirable voltage range.[51] Of these materials, monoclinic lithium trivanadate ($Li_xV_3O_8$, referred to as LVO) has a relatively high theoretical capacity (362 $mAh\ g^{-1}$) and has demonstrated good rate capability.[52,53] The mechanism of the initial lithiation and delithiation in LVO is well understood.[55–57,120] As-prepared LVO begins in the layered α-phase ($Li_{1.1}V_3O_8$), with layers of V_3O_8 sheets between which Lithium can be intercalated. Upon lithiation to $Li_{2.5}V_3O_8$, the α-phase is saturated and a phase transition occurs to the rock-salt like β-phase ($Li_4V_3O_8$), which can be lithiated up to $Li_5V_3O_8$.

Many have reported the dependence of capacity fade over extended cycling of LVO for materials prepared through an array of synthesis routes, including sol-gel based synthesis[55,58,70,121–125], solvothermal synthesis[58,59], flame spray pyrolysis[126], and freeze drying.[127] Zhang et. al. report LVO prepared by the sol-gel and solvothermal methods that were annealed at 500 °C that exhibit 15 to 20% loss in capacity over 100 cycles when cycled at a C/10 discharge rate.[58] Similarly prepared electrodes that were annealed at lower temperatures showed a 43% capacity loss when cycled at the same discharge rate for the same duration.[123] LVO prepared by freeze drying shows between 17 and 27% capacity fade over 50 cycles at a moderate C/6 discharge rate, depending on the annealing temperature.[127]

In addition to the annealing temperature and duration, the morphology of the active material is known to play an important role in its cycling stability. For instance, topotactically synthesized LVO nanowires demonstrated impressive cycling ability at very high discharge rates (88 % capacity retention at 4C for 1500 cycles).[128] Jouanneau et. al. determined that LVO crystals offer better cycling behavior compared to amorphous LVO.[121]

A widely cited cause of capacity fade in the literature is that the active material undergoes structural deformation due to the phase change from the layered α to rock-salt like β phase, which involves a significant expansion of the a axis and contraction of the b and c axes.[55] Experiments to support this claim are those where the formation of the β phase is avoided by cycling above 2.6 V[70] or galvanostatic cycling up to $Li_{2.5}V_3O_8$ to avoid the phase change.[58] Zhang et. al. observed a shortening of the plateau in the voltage profile at 2.5 V (attributed to the α to β transition) and an elongation of the shoulder in the voltage profile corresponding to lithiation of the β-phase during cycling at C/10, and suggest that their observations are indicative of irreversible β-phase formation.

Tanguy et. al. investigated capacity fade in LVO prepared by the common sol-gel method. They demonstrated that fade is observed in cells with different electrolytes, different amounts of conductive additives, and active materials annealed at different temperatures. Then, several possible explanations for capacity fade were systematically eliminated, including vanadium dissolution and water contamination, and it was conclusively shown that evolution of the cathode was primarily responsible for the fade observed in Li//LVO cells. Two (possibly related) mechanisms were identified: the formation of a surface film below 2.6 V, and the appearance of an additional electrochemical phenomena at 2.1 V.[124]

A more recent study by the authors employed *operando* energy dispersive X-ray diffraction (EDXRD) to compare thick porous LVO electrodes before and after cycling at 1C.[129] It was found that the utilization of these thick porous electrodes was uniform across the length of the electrode both before and after cycling despite significant capacity fade, ruling out electrode-scale effects as the dominant fading mechanism. EDXRD revealed that no β-phase was formed at the end of discharge after 95 cycles, qualitatively consistent with a model where the amount of active material after 95 cycles was reduced.

Whereas the previous experimental studies have relied on analysis of electrochemical measurements and characterization, the use of physics-based modeling in conjunction with these methods provides a powerful platform to draw conclusions about the evolution of LVO during cycling.

Approaches for understanding capacity fade using physics-based models have been employed in the literature. While many have taken the approach of implementing phenomenological models for different capacity fade mechanisms[48], this approach can prove complex when considering multiple phenomena occurring simultaneously. A simpler, easily implementable approach to understanding how the system is evolving is to reformulate a validated model by estimating model parameters relevant to physical phenomena at different cycles. Zhang et. al. used this approach to estimate electrode states of charge and cathode porosity for a graphite/NCO system using a pseudo 2-dimensional (P2D) model.[130] Similar work has been done for the LMO system.[131] Ramadesigan et. al. extended this approach to tracking changes in model parameters such as solid-state diffusion coefficients, reaction rate constants, and the Li ion diffusion coefficient in a P2D model, and included an analysis of uncertainties in the estimates of these parameters using an MCMC algorithm.[132] Li et. al. estimated 10 parameters in an extended single particle model (SPM) to determine model parameters that are most correlated with state of health for rapid health prediction.[133]

We have previously reported a full depth of discharge model for lithiation of the lithium trivandate cathode,[32] extending single particle and pseudo-2D (P2D) models developed by Brady et. al.[42,64] In this study, the reformulated physics-based model approach is employed in conjunction with the reported full depth of discharge model to understand how highly porous electrodes containing LVO prepared via the sol-gel method evolve with cycling at a current rate of C/5. Model results are used to design experiments to test the hypotheses generated by this parameter estimation approach, with the ultimate goal of identifying the physical mechanisms associated with the model parameters that are evolving.

4.2 Experimental

$Li_{1.1}V_3O_8$ (LVO) was synthesized via a sol-gel approach as previously reported.[55] Briefly, V_2O_5 and $LiOH$ were used as precursor materials in a stoichiometric ratio of $Li : V = 1.1 : 3$. The resulting solid was annealed at 500°C.

3D porous electrodes (3PEs) contained carbon nanotubes (CNTs) and LVO (weight ratios 30:70). The 0.5 inch diameter electrodes were used in a coin type cells with Li metal anodes and polypropylene separators in an argon-filled glove box. with 1 M $LiPF_6$ in ethylene carbonate/dimethyl carbonate (volume ratio of 3:7) electrolyte. Cycling is done at a C/5 rate, where 1C corresponds to 362 mA/g. All the electrochemical measurements were performed at 30 °C. A table of all the cells prepared and analyzed for this study is given in the Supporting Information.

For ex situ measurements, the cathodes were recovered in an argon filled glove box. The morphology characterization of pristine and cycled electrodes was obtained using a scanning electron microscope (SEM) (JEOL 7600F) operating at 10kV.

4.3 Parameter Estimation

The P2D model developed by Mayilvahanan et. al. has several model parameters because it couples the electrode scale with the particle scale, and models a mixed phase lithiation on the particle scale.[32] Re-estimating all these model parameters at different cycles is an onerous task. To narrow the parameter space, some preliminary analysis was performed.

Using the thickness, active material mass loading, and CNT mass loading, simulations reveal that heterogeneity across the length of the electrode can be neglected (Figure 4.11). This conclusion is supported by *operando* EDXRD results, which showed uniformity in three measurements across the length of a similarly prepared porous electrode.[129] Therefore, the analysis in this study is restricted to model parameters on the crystal scale, including the relative amount of active material $\%AM$, normalized to the active material with which the cell was assembled (here, inactive material refers to material that cannot participate in charge transfer), the solid phase diffusion coefficients in both phases D_i and the reaction rate constants for lithium insertion in both phases $k_{rxn,i}$ (closely related to exchange current densities, see reference[32]) where i refers to the phase α or β. It is important to note that when $\%AM$ is varied, the volume fraction of active material and the active surface area are reduced by $100 - \%AM$, but the porosity remains unchanged. Changes in the rate constant for phase change k_β were also initially considered, but the change in shape of the discharge profiles when varying this parameter did not match any observed profiles. It is important to note that, while 5 parameters are considered, the statistical treatment, discussed next, shows that only a subset appears to vary significantly during cycling.

The reformulated models are fit to discharge data at each cycle as outlined by the parameter estimation procedure published by Brady et. al.[71] In short, parameters are determined at each cycle by minimizing

$$RSS = \sum_{j=1}^{n} (V_{sim,j} - V_{exp,j})^2 \tag{4.1}$$

where n is the number of simulated data points for a discharge, $V_{sim,j}$ is the simulated voltage at point j, and $V_{exp,j}$ is the experimental voltage at point j. The fit of each simulation is quantified by this residual sum of squares (RSS) and the likelihood of a parameter set is evaluated based on an assumption of 50 mV experimental uncertainty in voltage measurements. The SciPy interpolation function interp1d is used to map the simulated voltages in a discharge to the exact time points of the experimentally measured voltages in a discharge. If a simulation reaches the lower cutoff voltage of 2.0 V at an earlier time compared to the discharge profile of the cycle being analyzed, the remainder of the simulation-predicted voltages are filled to 2.0 V. Error for a simulated discharge relative to an experimental discharge can be summarized by a root mean squared error, or $RMSE$, reported in mV.

$$RMSE = \sqrt{\frac{RSS}{n}} \tag{4.2}$$

In addition to minimization of RSS, an approach adopted from the least absolute shrinkage and selection operator (LASSO) algorithm, was used to determine the relative importance of each parameter in improving the fit between the reformulated model and experiment.[134] This approach is akin to a sensitivity analysis, but it achievable with minimal computational cost. In short the same simulated results from the sampling study used to minimize a new objective function

$$Lasso = RSS + \lambda \sum_{i}^{N_p} |\gamma_i| \tag{4.3}$$

where γ_i is a transformation of parameter i (i of N_p parameters) based on the first-cycle parameter estimate p_i^0 and the first-cycle parameter estimate uncertainty $\sigma_{p,i}^0$:

Table 4.1: Model parameters considered and the range of sampling.

Model Parameter	**Symbol**	**Range**	**Units**	p_0	σ_0
Relative active material	$\%AM$	$[75, 100]$	%	1	0.016
Solid phase diffusion coefficient in α phase	$log_{10}D_\alpha$	$[-13.0, -12.5]$	$cm^2\ s^{-1}$	-12.63	0.07
Rate constant for Li insertion in α phase	$log_{10}k_{rxn,\alpha}$	$[-8.0, -7.0]$	$cm^{5/2}\ mol^{-1/2}\ s^{-1}$	-7.00	0.06
Solid phase diffusion coefficient in β phase	$log_{10}D_\beta$	$[-15.2. - 14.5]$	$cm^2\ s^{-1}$	-15.09	0.03
Rate constant for Li insertion in β phase	$log_{10}k_{rxn,\beta}$	$[-9.0, -7.5]$	$cm^{5/2}\ mol^{-1/2}\ s^{-1}$	-8.75	0.25

$$\gamma_i = \frac{p_i - p_i^0}{\sigma_{p,i}^0} \tag{4.4}$$

The second term λ on the right hand side of equation 4.3 is an additional penalty (referred to as a shrinkage penalty) that favors γ_i values equal to zero,[135] corresponding to a parameter remaining unchanged from its first cycle estimate ($p_i = p_i^0$). The tuning parameter λ sets the weight of the penalty for a parameter changing from it's first cycle estimate. Minimization of equation 4.3 for different values of λ allows one to identify the parameters that most improve the fit and quantify the improvement in the fit resulting from changes in each parameter.

Parameters are sampled from uniform prior distributions in the ranges specified in Table 7.1, where the range of the distribution for each parameter is chosen to be sufficiently wide to encapsulate physically reasonable values of the parameters. Because results are somewhat limited by the density of sampling in the parameter space, when showing trends in parameters over the course of cycling, results are presented as 5 cycle rolling averages.

4.4 Results

4.4.1 Cycling Data

The cycling stability and discharge profiles are shown in Figure 4.1. The cell exhibits a more constant rate of fade initially. After 70 cycles, the rate of fade starts to accelerate. Upon cycling,

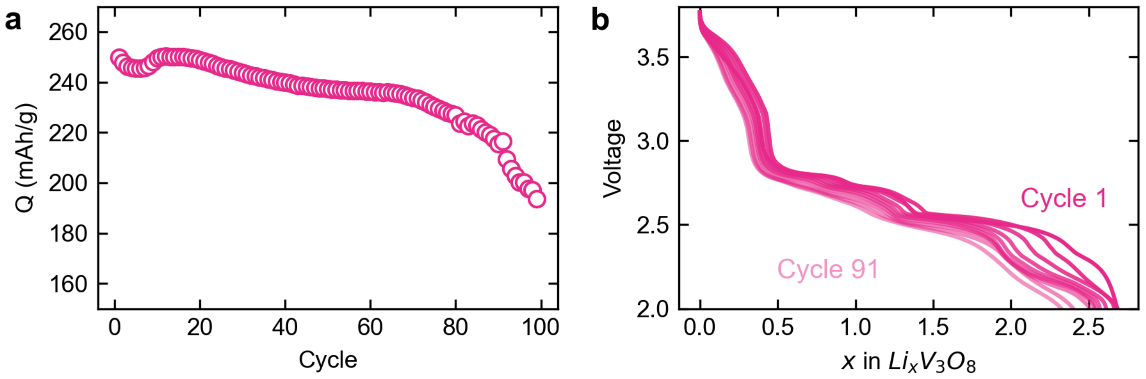

Figure 4.1: Discharge capacity fade (a) and voltage profiles for discharge for every 10 cycles (b).

an extended low-slope region is observed at approximately 2.1 V, as Tanguy et. al. observed.[124] To tease apart how the system is evolving in more detail, the parameter estimation procedure is applied.

4.4.2 Reformulated Model Analysis

The results of the parameter estimation are presented in Figure 4.2. The shaded regions about the solid lines describe the confidence of the parameter estimate, quantified by two standard deviations from the mean estimated parameter. Several important indicators of the evolution of the system are contained in these plots.

The estimate of active material decreases with cycle number, as concluded in the previous study.[129] The estimated rate constant for Li insertion in α phase $k_{rxn,\alpha}$ decreases by approximately an order of magnitude over the course of cycling. Since the applied current is set based on the mass of LVO with which the cell was assembled, less active material corresponds to higher local current densities for the material that is active. This, combined with a lower exchange current density for Li insertion in the α phase, results in an increased charge transfer overpotential. Diffusion in the α phase appears to be evolving as evidenced by the increase in estimated D_α.

The parameter estimation applied to the β phase presents insights into the evolution of the β phase with cycling (Figure 4.2d,e). D_β increases by half an order of magnitude over the course of 30 cycles, whereas the rate constant for Li insertion in the β phase drops to a value of approximately

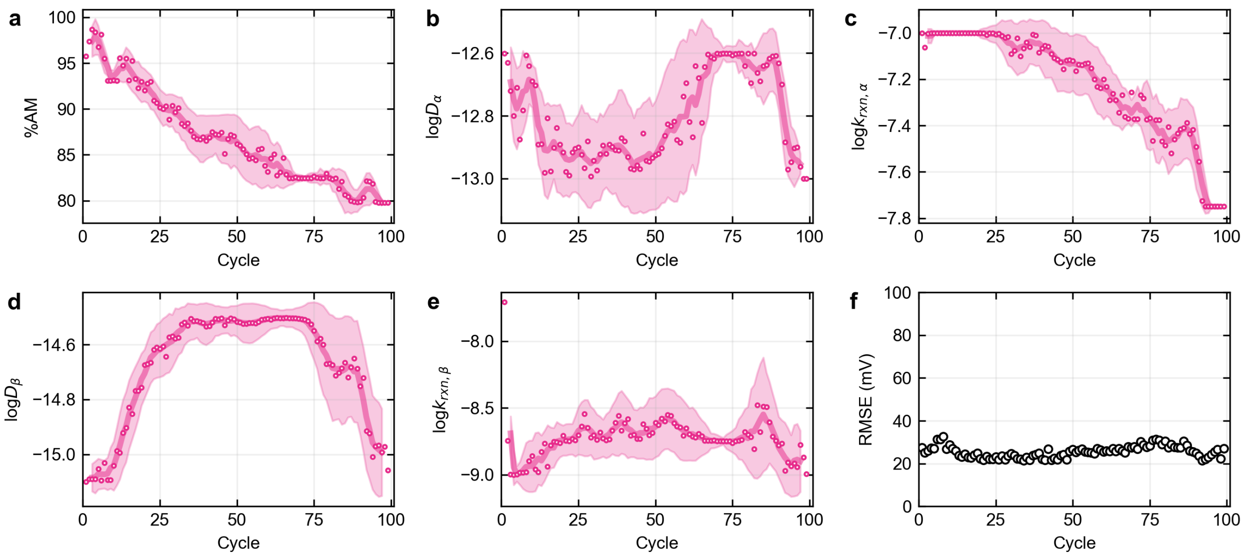

Figure 4.2: Parameter estimates for five parameters presented in Table 7.1 (a-e). Shaded regions show 2 standard deviations above and below the maximum likelihood parameter estimate. Root mean squared error (RMSE) for the maximum likelihood parameter estimates compared to experiments (f).

$10^{-8.7}$ in the first 10 cycles. Given the parameters considered in this study, the increase in estimated D_β and decrease in estimated $k_{rxn,\beta}$ represent the emergence of the plateau at 2.1 V. Because the β phase is formed towards the end of discharge, changing these two parameters do not have as much of an impact on the simulated voltage profile compared to $\%AM$, D_α, and $k_{rxn,\alpha}$. Therefore, the uncertainties in these parameters are larger.

Though in Figure 4.2b and d the results are presented as increasing diffusion coefficients, it is important to note that these results assume a fixed crystal size. An alternative conclusion from these results is that the length scale for diffusion is decreasing (smaller particles). A hypothesis that ties this in with the observation of loss of active material is particle fracture, which has been observed in other transition metal oxide cathodes.[136–138] As the active particles fracture, fragments could become disconnected from the conductive matrix, rendering them inactive.

Though Figure 4.2 provides some insights on which parameters are evolving over the course of cycling and by how much, it does not tell us about which parameters have the biggest impact on explaining the change in the voltage profile over the course of cycling. The LASSO framework provides a means to discuss this type of model sensitivity. An example of this analysis is presented in Figure 4.3, where one cycle (cycle 31) is analyzed.

In Figure 4.3a and b, the results of minimization of the LASSO objective function (equations 4.3) is presented for different values of the shrinkage penalty λ. For high values of λ on the right side of the plot, all the model parameters remain the same as their first cycle values (see equation 4.4 and Table 7.1). As the shrinkage penalty is lowered, parameters are allowed to vary from their first cycle values and are effectively added to the model, and the corresponding reduction in fitting error can be traced in Figure 4.3b. Inclusion of only the $\%AM$ model parameter can reduce the $RMSE$ by 47 mV. Subsequent inclusion of $k_{rxn,\beta}$ reduces the error by another 5 mV, and inclusion of D_β then reduces the error by another 6 mV. Finally, inclusion of $k_{rxn,\alpha}$ only reduces the error by less than 0.2 mV.

While the $RMSE$ for a model's prediction of an experimental voltage profile is a useful summary statistic, a more detailed analysis is needed to understand what portions of the voltage profile are controlled by each model parameter. In Figure 4.3c, the experimental voltage profile for cycle 31 is shown alongside the cycle 1 model prediction, referred to as the base model, and the subsequent models that arise from including each additional parameter as λ is lowered. For example, the model labeled $+D_\beta$ is the base model with $\%AM$ reduced by 8 standard deviations from its first cycle estimate and $k_{rxn,\beta}$ reduced by 5 standard deviation from its first cycle estimate, given by $\beta_{\%AM}$ = -8 and $\beta_{k_{rxn,\beta}}$ = -5 in Figure 4.3a, respectively. All the models predict the voltage profile well until about 170 $mAh\ g^{-1}$. To emphasize the differences at the end of discharge, the results in Figure 4.3c are presented as differences between model predictions and experiments in Figure 4.3d. Here, the value of the inclusion of each subsequent parameter is made clear. The base model overpredicts the voltage of the cycle 31 discharge starting at approximately 50 $mAh\ g^{-1}$. Inclusion of $\%AM$ fixes this, but still overpredicts the voltage at 200 $mAh\ g^{-1}$ and underpredicts the voltage and final capacity afterwards. Inclusion of $k_{rxn,\beta}$ improves the fit at 200 $mAh\ g^{-1}$, but still suffers from underprediction of voltage and capacity at the very end of discharge. Inclusion of D_β results in good agreement at at 200 $mAh\ g^{-1}$ and beyond, to the end of discharge. Finally, inclusion of $k_{rxn,\alpha}$ offers minimal improvement.

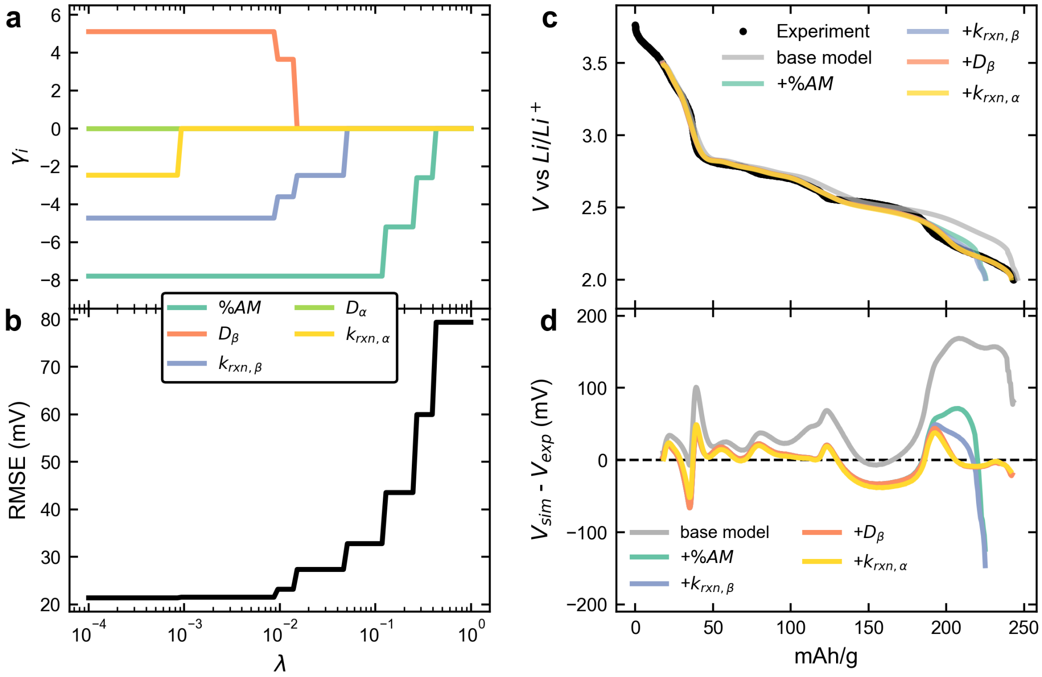

Figure 4.3: An example of the LASSO analysis is presented for the cycle 31 discharge. Change in transformed parameter values that minimize the $LASSO$ objective function (see equations 4.3,4.4) for different LASSO shrinkage penalties (a). The corresponding change in $RMSE$ for the parameter set that minimizes the $LASSO$ objective function (b). Model predictions as each additional parameter is added, starting with the base (cycle 1) model (c). The difference between the predicted voltage and the experimental voltage for the models in c as a function of lithiated capacity (d)

This LASSO inspired framework provides a systematic approach to understanding the impact of each parameter on the voltage profile. As opposed to doing a one-by-one sensitivity analysis varying each parameter individually and then in conjunction, it allows for extraction of model sensitivity from already generated simulations in the parameter estimation. By considering varying shrinkage penalties, a series of models with a different number of free parameters (i.e. parameters different from their cycle 1 values) are generated, and the marginal contribution of each additional parameter added to the model can be evaluated.

The procedure discussed above is applied to several cycles over the course of cycling to understand how the contribution of different model parameters to improving the fit from the base model depends on the cycles completed. The analysis is presented in Figure 4.4. The improvement in $RMSE$ from the base model is evaluated by considering the drop in $RMSE$ when a model parameter is allowed to vary (see Figures 4.3a and b). The total height of the bar corresponds to the difference between the $RMSE$ of the five parameter model and the $RMSE$ of the base model. In Figure 4.4a, the $RMSE$ is calculated over the whole discharge, between 3.6 V and 2.0 V. It is clear that the $\%AM$ is the parameter that explains most of the evolution of the voltage profile at all cycles.

As discussed in the above analysis of cycle 31, the inclusion of parameters after $\%AM$ serve to improve agreement at the end of the discharge. To better assess the impact of these additional parameters, the $RMSE$ is calculated below 2.45 V in Figure 4.4b. The contribution of the parameters associated with the β-phase - D_β and $k_{rxn,\beta}$ - appear to become negligible after cycle 76. This may explain why the uncertainty in D_β increases drastically in Figure 4.2d after this cycle number. The rapid increase in uncertainty, combined with the lack of model sensitivity to this parameter indicate that changes in this parameter after cycle 75 should not be considered meaningful. In short, the statistical analyses suggest that a decline in D_β after 75 cycles is not likely to be physical.

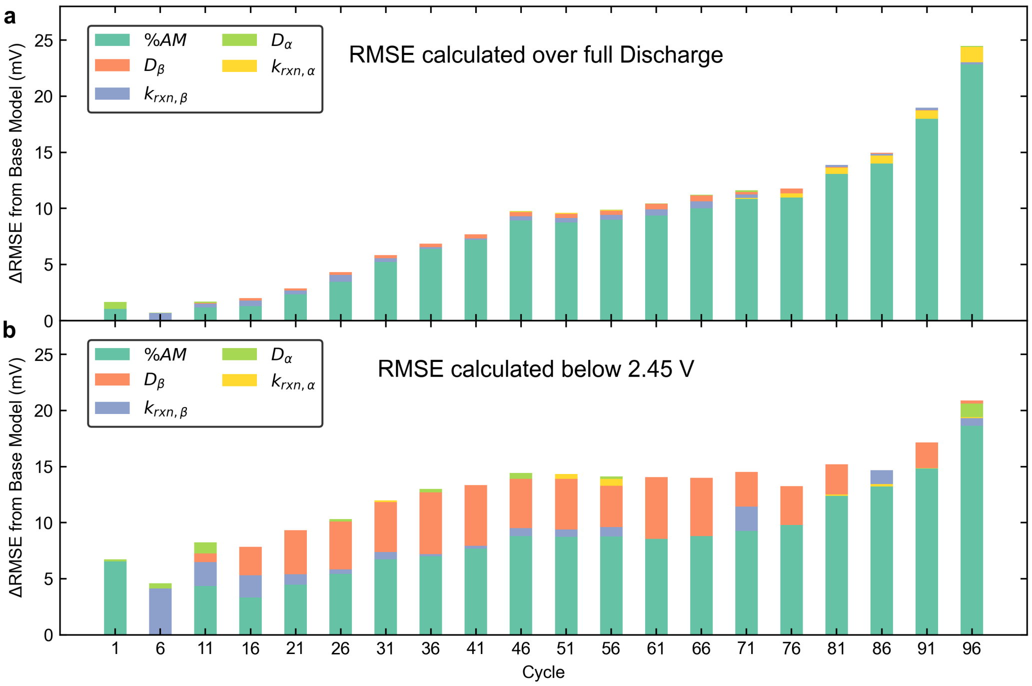

Figure 4.4: Results of the LASSO procedure applied to experimental data from every five cycles over the course of 100 cycles. Improvement in the $RMSE$ from the base model (parameters fitted to cycle 1) is shown for the entire discharge (a) and for the portion of the discharge below 2.45 V (b).

4.4.3 Current Interrupt Experiments

To validate the conclusion of an increasing amount of LVO becoming inaccessible for charge transfer based on the parameter estimation results, the galvanostatic interrupt titration technique (GITT) was performed before and after cycling for 40 cycles (Figure 4.5a). The number of cycles was chosen based on the parameter estimation results, which show the system appears to have evolved significantly by 40 cycles. After cycling, recoveries occur at lower voltages, and the recovery portions of the response appear to have larger voltage recoveries to open circuit in earlier interrupts, compared to the response before cycling. The recovery time at each current interrupt portion of the experiment is calculated as the time required for the measured voltage to reach within 1 mV of the final voltage at rest. The results of this analysis are shown in Figure 4.5b, where the recovery time at a given interrupt is plotted as a function of the cumulative capacity lithiated before that interrupt. Faster recovery times are observed after cycling when up to approximately 120 mAh/g has been lithiated in the current interrupt experiment. We note that in Figure 4.5a it appears that the relaxations in the β-phase regime do not reach equilibrium in the 1 hour allowed for recovery.Therefore, recovery times calculated in these regions should not be used to draw any conclusions.

By taking the parameter estimates after 40 cycles and using those as inputs into the model, the GITT experiment before and after cycling were simulated to explain the experimental observations. The simulation results are shown in Figure 4.6. The model predictions agree qualitatively with the observed GITT responses. Some disagreement is expected since the cell cycled and shown in Figure 4.5 is different than the cell from which parameter estimates were obtained. In both, lower voltages are reached at earlier interrupts. This can be explained by the deactivation of LVO. As material becomes inactive, the particles that are active must take on a higher current and thus a higher degree of lithiation, corresponding to lower voltages.

The model predicts that the cycled cell undergoes a greater degree of phase transformation (α to β) at earlier times (Figure 4.6b). Higher local currents after cycling cause a more rapid lithiation of the active particles. The saturation concentration $Li_{2.5}V_3O_8$ is reached, and the material undergoes phase transformation at earlier times. This can explain some of the differences between measured voltage response to the GITT experiment before and after cycling. Previous results have shown that the kinetics for lithium insertion into the β-phase are slower than the kinetics for lithium insertion into the α-phase.[32] Therefore, the larger voltage recoveries appearing at earlier times after cycling are likely associated with the disappearance of larger charge transfer overpotentials when the current is interrupted, because the lithium being inserted into the active material is entering the β-phase.

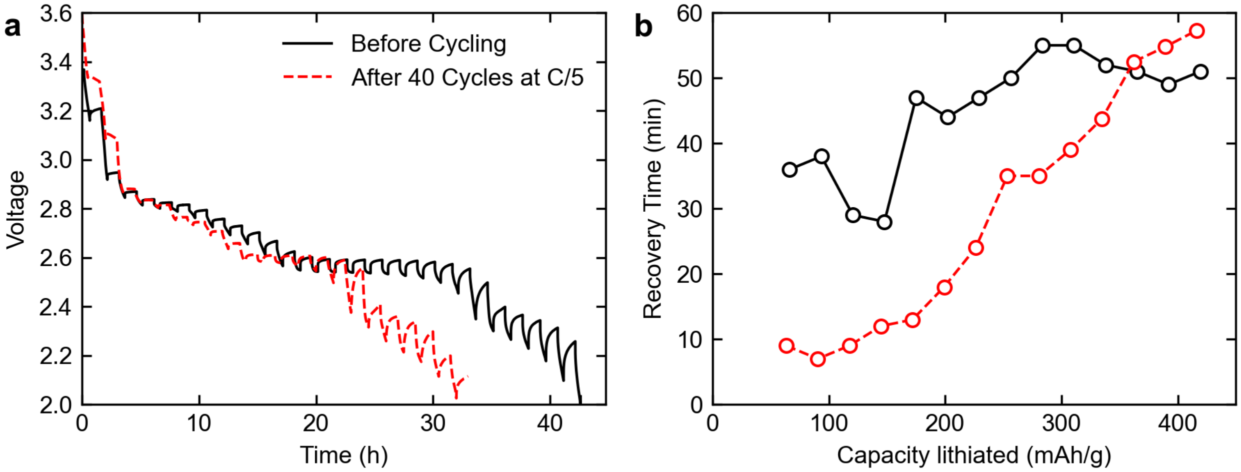

Figure 4.5: GITT response for a pristine cell and the response after cycling that cell for 40 cycles to 2.0 V at 0.2 C. A 0.05 C pulse is applied for 30 minutes, followed by a 1 hour recovery (a). Recovery time (i.e. time to reach within 1 mV of final potential in recovery) for each interrupt (b).

Obtaining a better understanding of the state of the material at each interrupt in Figure 4.5 can also provide insight into the conclusions from parameter estimation about diffusion processes becoming faster as the material is cycled (Figure 4.2b,d). Figure 4.6b shows the simulated volume fraction of β-phase as a function of the capacity lithiated in the GITT experiment. In the first 5 interrupts (up to 50 mAh/g lithiated), where the material is expected to be entirely in the α-phase, it is clear from Figure 4.5b that the diffusion process in the α phase is faster after cycling. After cycling, the material is expected to have a higher volume fraction of β-phase when more than 50 mAh/g has been lithiated. Since $D_\beta << D_\alpha$,[32,57] all else equal, one would expect a longer recovery times after cycling. That the opposite is observed indicates that the material has evolved, and the

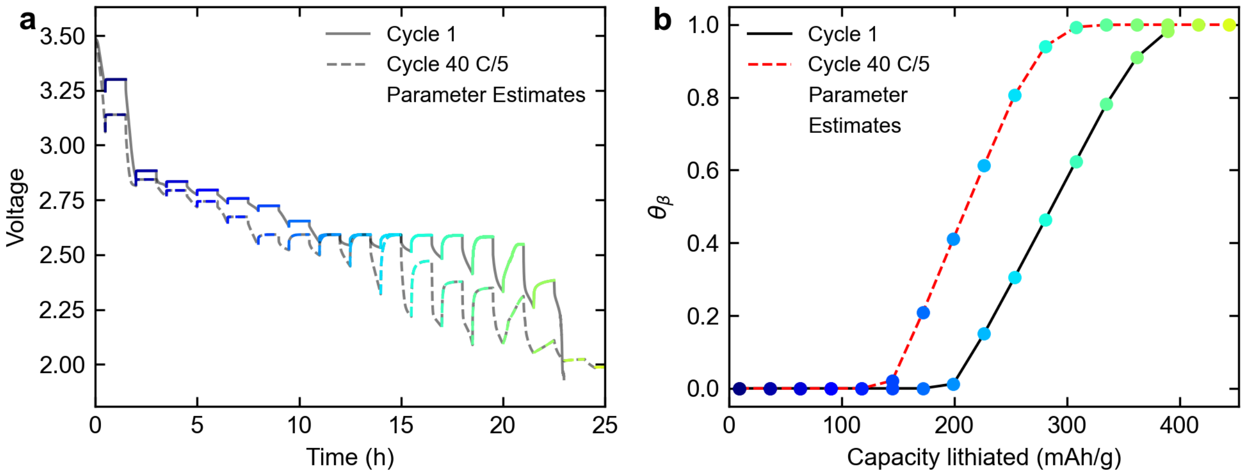

Figure 4.6: Simulated GITT response before and after cycling for 40 cycles to 2.0 V at 0.2 C. Simulations shown for a 0.05 C pulse is applied for 30 minutes, followed by a 1 hour recovery (a). Model-predicted volume fraction of β-phase θ_β over the course of both simulated experiments, as a function of the capacity lithiated before each interrupt (b). Each interrupt in (a) is highlighted by a given color to match θ_β at a given interrupt in (b).

experiment is probing a meaningful change in lithium diffusion in both phases induced by cycling. We note that though the simulated recoveries appear to be faster compared to the experiments, it is meaningful that the model is able to reproduce the slow recoveries after cycling compared to before cycling, as well as the shift down of the whole voltage profile for the experiment after cycling.

4.4.4 Evidence of Particle Cracking

The parameter estimation results pointed to faster diffusion processes in both phases, a result that was further supported by the GITT experiment. To address whether these results were due to shorter length scales for diffusion, the dimensions and morphology of the LVO crystals before and after cycling were investigated via SEM. The micrographs are shown in Figure 4.7.

Before cycling, there appear to be large rectangular particles and smaller fragments (Figure 4.7a,b), which are not observed after cycling (Figure 4.7c,d). Particle size distributions were extracted from the micrographs, and results are shown for the length and width of the larger particles before and after cycling in Figure 4.8. Clear reductions in particle size are observed. Smaller (sub-micron) particles are also observed in the SEM, but their sizes were difficult to quantify.

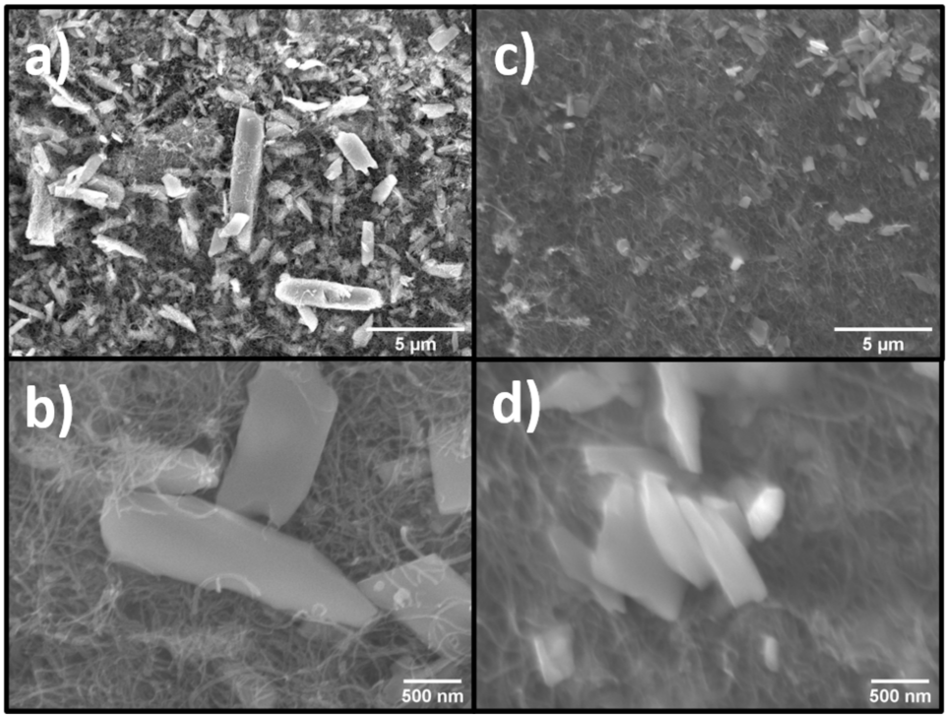

Figure 4.7: SEM characterization of the morphology evolution of LVO-CNT electrodes: pristine (a, b) and after aging (c, d).

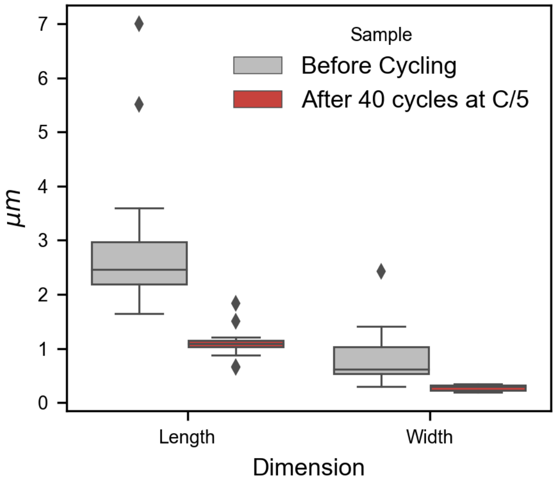

Figure 4.8: Particle size distribution for LVO crystals before and after cycling, shown as box and whisker plots. Distributions shown for the longer dimension (length) and shorter dimension (width) of rectangular LVO crystals. Boxes show the interquartile range of the measurements, and whiskers extend to 1.5 times the interquartile range. Observations outside this limit are identified as outliers and denoted by diamonds.

4.4.5 Partial Cycling

The findings from the parameter estimation, current interrupt experiments, and SEM suggest that as cycling occurs, capacity fade is the result of particle cracking and subsequent loss of active material. The question remains as to the root cause of these phenomena, and two competing hypotheses in the literature, phase change induced capacity fade[55,58,70] or a low-voltage electrochemical reaction[124], are considered. To test these hypotheses, two modified cycling protocols were designed and compared to the original cycling protocol used for the data in Figure 4.1. The protocols are summarized in Table 4.2.

Table 4.2: Description of cycling protocols for extended cycling experiments. For all experiments, discharge and charge currents are at 0.2 C, and at the top of charge the voltage is held at 3.6 V until current falls below 0.1 C.

Protocol	Discharge voltage window	Constant voltage hold
CC-full	3.6 to 2.0 V	-
CC-partial	3.6 to 2.6 V	-
CC-CV-partial	3.6 to 2.5 V	at 2.5 V until current falls below 0.1 C

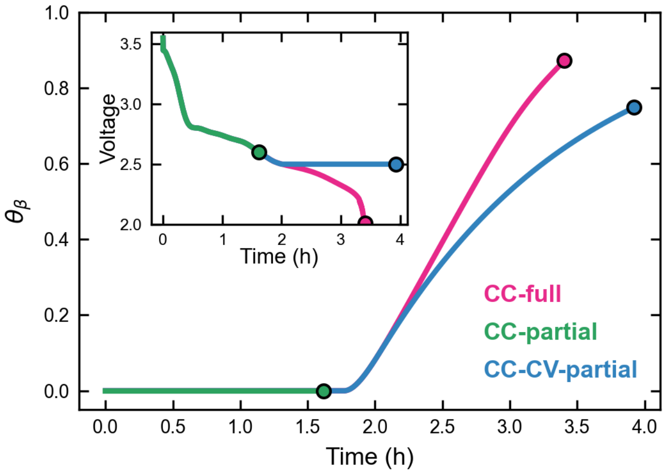

Figure 4.9: Volume fraction of β-phase (θ_β) through the duration of the discharge for three different cycling protocols, described in Table 4.2. Corresponding simulated voltage profiles shown in inset.

The first protocol, referred to as CC-partial, reproduces an experiment in the literature where cycling is performed between 3.7 V and 2.6 V, but at a higher rate (0.2 C) compared to what has been reported (0.1C, 0.05 C).[70] The choice of the lower bound of this cycling window ensures that

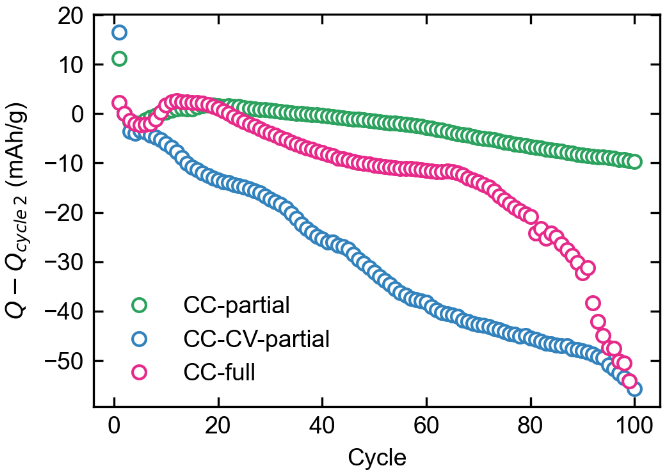

Figure 4.10: Loss in capacity for each cycling protocol in Table 4.2. Second cycle capacity was chosen as a normalization to better visualize long-term evolution due to cycling as opposed to the first-cycle drop in capacity.

no β-phase is formed (Figure 4.9) and avoids a possible electrochemical phenomena around 2.1 V. The results of the experiment are shown in green in Figure 4.10, where results are plotted as the difference between the delivered capacity and the capacity at cycle 2. The capacity is more stable than the full depth of discharge protocol (CC-full) over 100 cycles, but some fade is still observed. Closer examination of the voltage profiles (Figure 4.12e) reveals non-negligible material loss, as evidenced by the shift back in the voltage profile. That capacity fade is still observed indicates that there is still a fade mechanism that is not related to phase change with a small effect. This mechanism is likely similar to the mechanism in play when cycling at 1C, where less than 20% of the crystal is expected to undergo phase transformation at the end of discharge.[129]

While it has been established that there is a greater degree of capacity fade when cycling to 2.0 V compared to restricting the voltage window to above 2.6 V with the CC-partial protocol, it is still unclear whether this result is due to avoiding phase change or avoiding an emerging reaction at 2.1 V. This is because as the material is discharged to lower voltages, the material is simultaneously undergoing phase change, as seen in the pink curve (CC-full) in Figure 4.9. To decouple the phase change from the low voltage region where there may be a side reaction present, a second cycling protocol was designed. In this protocol, referred to as CC-CV-partial, the discharge cutoff voltage is set to 2.5 V, and when this condition is reached, a constant voltage hold is applied until the current falls below a value equivalent to 0.1 C. The simulations reveal that an extent of phase transformation similar to that at the end of discharge for the CC-full experiment (pink) can be achieved in the CC-CV-partial experiment (blue), all while avoiding voltages below 2.5 V. The cycling stability results in Figure 4.10 (blue) show that there is a greater rate of normalized capacity fade than the CC-full cycling experiment. The signature of active material loss, the shift back in the voltage profile, is also seen (Figure 4.12f) These results support the hypothesis that phase change drives the particle cracking and subsequent material loss in LVO particles when cycling at 0.2 C. Though this does not definitively rule out Tanguy et. al.'s hypothesis of a low voltage side reaction, it confirms that phase change does play a significant role, and that their differential capacity analysis could be mistaking a faster diffusion process in the β-phase for a side reaction.

4.5 Conclusions

A reformulated model approach is applied to analyze cycling of LVO at a current rate of 0.2 C. Parameters in a validated LVO model are re-estimated over the course of 100 cycles, and evolution of the electrode is identified in terms of deactivation of LVO and faster diffusion processes in the LVO particles. A framework is provided to assess the impact of model parameters in explaining the changes in the voltage profiles, and the percent active material parameter is shown to explain a majority of the evolution in the observed voltage profile. The hypotheses from the parameter estimation are supported by a current-interrupt experiment. SEM reveals fractured particles after cycling, consistent with the observations about transport and material loss, since fractured particles are more susceptible to lose connectivity with the electronically conductive network. Finally, partial cycling experiments confirm that formation of the β-phase does in fact play a significant role in capacity fade when cycling at 0.2 C, but that non-negligible capacity fade is also observed even when no β-phase is formed, in line with observations of fade at high-rate cycling.

This paper also can serve as a general framework for understanding capacity fade in various electrode materials. While estimating parameters of a validated model at later cycles can generate hypotheses about what may be evolving in the system, further experimentation designed by models and informed by these results can be insightful in testing these hypotheses and understanding their root causes.

4.6 Supporting Information

Table 4.3: Electrode fabrication details for the five electrodes shown in this study. Refer to Table 4.2 for definitions of cycling protocols.

Figure	**Cycling Protocol**	**LVO (mg/cm2)**	**CNT (mg/cm2)**	**Thickness (um)**
1,8	CC-full	13.5	5.8	307
3	GITT, CC-full, GITT	15.3	6.6	241
5,6	CC-full	18.3	7.8	344
8	CC-partial	18.1	7.8	303
8	CC-CV-partial	17.1	7.3	307

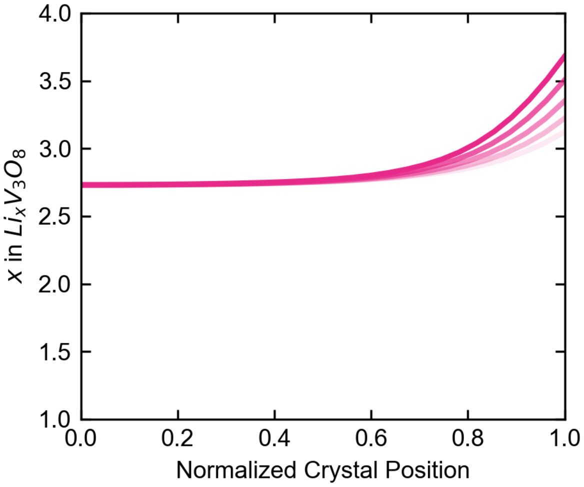

Figure 4.11: Simulated lithiation state at the end of first discharge for crystals at different locations along the lengths of the electrode considered in this study. Each family of profiles of a given color correspond to an electrode discharged at the indicated current rate. The opacity of the line corresponds to the position of the crystal for which the profile is shown, going from crystals near the separator (darkest) to crystals near the current collector (lightest).

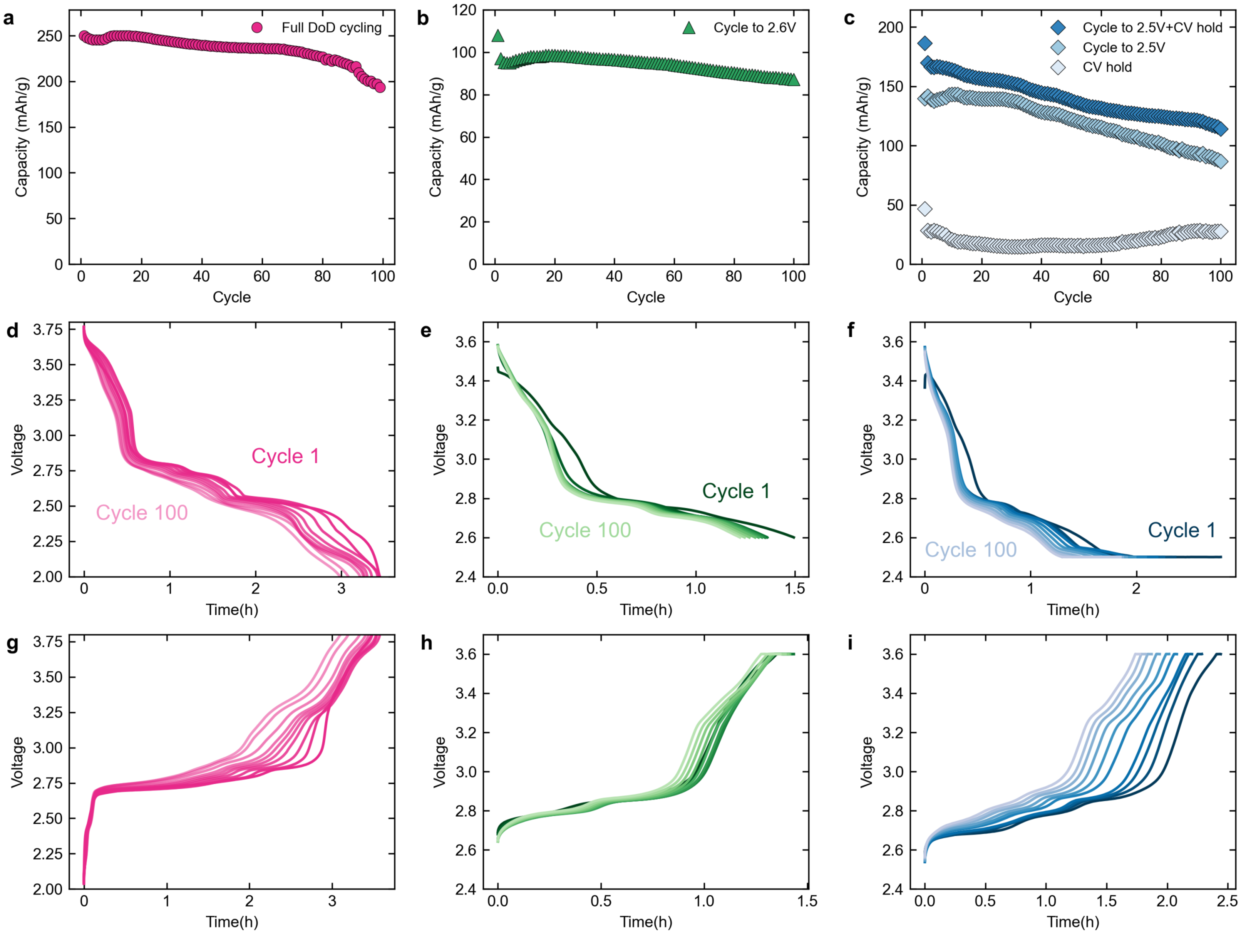

Figure 4.12: Results for each of the three cycling protocols described in this paper. The first column (a,d,g) corresponds to the full depth of discharge experiment CC-full. The second column (b,c,h) corresponds to the partial depth of discharge experiment CC-partial. The first column (c,f,i) corresponds to the partial depth of discharge experiment with a constant voltage hold CC-CV-partial. Top row shows delivered capacities, second row shows discharge profiles, and thrid row shows charge profiles. The capacity from the set current and constant voltage portions of the discharge for the CC-CV-partial as well as their sum is shown in (c).

Chapter 5

Supervised Learning of Synthetic Big Data for Li-ion Battery Degradation Diagnosis*

---

*This Chapter has been published: Karthik. S. Mayilvahanan, Kenneth. J. Takeuchi, Esther. S. Takeuchi, Amy. C. Marschilok, and Alan. West, “Supervised Learning of Synthetic Big Data for Li-ion Battery Degradation Diagnosis,” *Batteries & Supercaps*, p. batt.202100166, Aug. 2021.
The thesis writer’s contribution was ideation, implementation of ML models, analysis and writing.

5.1 Introduction

Li-ion batteries can undergo significant degradation during use and storage, which result in capacity fade and power fade. Models to understand, diagnose, and predict degradation are necessary in management of commercialized batteries and development of new batteries. The existing models for diagnosis and prognosis of the state of Li-ion batteries include empirical, mechanistic, and physics based models. Physics based models describe physical phenomena inside the battery using coupled partial differential equations.[48,82] These models allow for description of a wide variety of degradation processes in Li-ion batteries, such as solid electrolyte interphase (SEI) formation[45,46,139] and particle cracking.[47] Mechanistic models do not explore the root causes of degradation, but model the evolution of the system using the net effect of the degradation processes, such as loss of active material, loss of lithium inventory, and resistance increase.[48,140] While these models encode physically relevant information, their applicability may be limited by more cumbersome evaluation and the large number of parameters that must be identified.

Empirical models include algebraic equations for capacity prediction[141] as well as more flexible data-driven machine learning (ML) models.[142] These models have been reported extensively in the literature for both state of health (SOH) estimation[143–147] and remaining useful lifetime (RUL) prediction.[148–153] While they are easy to evaluate, the lack of incorporated physics, and relatively small data sets make them limited in scope, often to the specific data set, chemistry, and cycling conditions of the data on which they were trained.

Recently, there has been interest in the community in combining the physical grounding and interpretability of mechanistic models with the adaptability and ease of evaluation of empirical ML models.[13,154] Specifically, supplementing or replacing experimental training data for ML models with synthetic training data generated by a physics based or mechanistic model has been proposed as a solution to the data limitation problem.[155]

In this study, supervised learning models are trained on low rate charge curves generated by a mechanistic model published by Dubarry et al.[156–158] C/25 charge curves are provided for three different cells (graphite-LFP, graphite-NCA, and graphite-NMC811), and full-cell voltage vs. capacity curves are provided for varying degrees of loss of lithium inventory (LLI) loss of active material (LAM) in either electrode with extremely high resolution, creating a big-data training set for the development of ML algorithms. The authors of this data set have published an analysis alongside a model that uses predefined predictive features from the voltage curves and a lookup table to predict the values of the degradation modes with very high accuracy (1 %).[159] Others have trained ML models on similar, smaller data sets to regress values of the degradation modes as well.[160]

The goal of this study is to provide a detailed implementation and comparison of supervised machine learning models to diagnose battery degradation. We take some common transformations of the low rate charge curves that are known to contain information relevant for diagnosis, including incremental capacity and differential voltage curves, and use these curves to train machine learning models to diagnose battery degradation. We first train models to regress values of the common degradation modes and compare model accuracies to the state of the art. Results indicate that random forest regressors trained on features from incremental capacity curves perform the best, with root mean squared errors of about 5 %. Next, we train classifiers to identify the limiting electrode during charge and discharge, which can be identified to 97 % accuracy. In deliberately choosing interpretable models in this study, we aim to make two main contributions. First, we quantify interpretable models' performance, i.e. the ability to learn the relationship between the voltage curves and the degradation modes. Knowing these values are important when benchmarking more complex deep learning algorithms, as a simpler model should be chosen if it gives comparable performance to a more complex model. Second, we explore the ability of interpretable models to understand what features are indicators of degradation, since models that are able to perform well and provide same physical understanding at the same time are of great value to the community. We find that with large synthetic training sets, these simple, interpretable machine learning approaches can achieve high accuracy while simultaneously offering interpretability after fitting.

5.2 Degradation Modes and Limiting Electrodes

A helpful framework provided by Birkl et al.[161] categorizes degradation into causes, mechanisms, modes, and effects. Causes include factors such as temperature, voltage cutoffs, current, and mechanical stress that can affect the extent of degradation. Mechanisms include physical phenomena such as SEI growth, particle cracking, Li plating, etc. that are influenced in a highly coupled way by the causes. Mechanisms manifest in degradation modes, which are broad categories including loss of lithium inventory (LLI), loss of active material (LAM), and ohmic resistance increase (ORI). The degradation modes are also coupled to various combinations of degradation mechanisms. The final category, effects, provides the observable results of the degradation, namely capacity fade and power fade.

Studies understanding the relationships between causes and effects of degradation are being conducted on commercial cells.[162–164] Such data sets are well positioned for data driven studies because the training data can be generated under different cycling conditions to observe the resulting power and capacity fade, but generating large enough data sets that explore all the causes and combinations of causes remains challenging.

Mapping causes to mechanisms or mechanisms to effects is more challenging, because there are several possible mechanisms for a given cell with specific active materials, electrolyte, binders, conductors, etc. under different cycling conditions. Physics-based models for different mechanisms and their relation to the causes have been proposed and used to some extent[48,132,165] but the resulting parameter space is large unless some cell-specific expert knowledge is applied for reduction.

Degradation modes represent the collective effects of the degradation mechanisms on the capacity and voltage. Since the degradation modes can fall into a few broad categories, it is a more achievable task to identify them.[140] In this study, we examine slow rate diagnostic cycles. Because of the current rate, thermodynamic degradation modes (LLI, LAM) are probed , and ORI from slower charge transfer kinetics or slower transport will not appear. Future work could include analysis of voltage curves at different current rates, which would allow for ORI diagnosis as well.

The data sets from Dubarry et al. analyzed here consider three degradation modes: loss of lithium inventory (LLI), loss of active material in the positive electrode (LAM_{PE}), and loss of active material in the negative electrode (LAM_{NE}). LAM_{PE} and LAM_{NE} can occur in the lithiated or delithiated state. In this case, LAM_{PE} and LAM_{NE} are assumed to occur in the delithiated state. Any loss of lithiated active material is counted in both LAM and LLI.

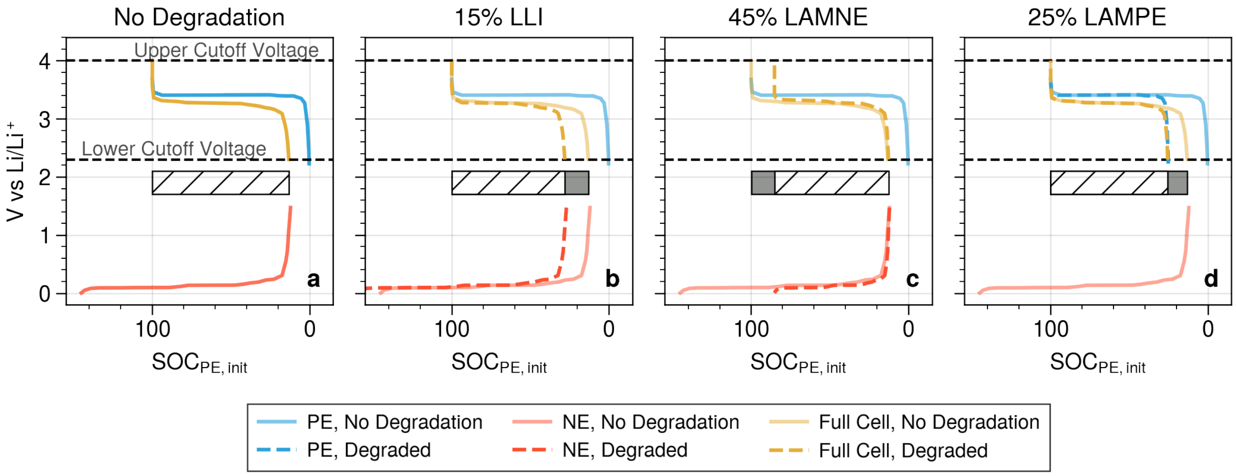

Figure 5.1: Exemplary low rate charge curves for an LFP cell. The half cell voltages and resulting full cell voltage for the case of no degradation (a), 15% LLI, (b), 45% LAM_{NE}, (c), 25% LAM_{PE}, (d). The hashed bar in the center of each plot represents the cyclable lithium (usable capacity). The grey regions in the bars in (b-d) show the amount of capacity lost relative to the no degradation case in (a). Figure is adapted from Reference[161].

The effects of these three modes on the low rate charge curves are well documented.[140,161] Figure 5.1, adapted from reference[161], shows examples of the effects of these modes on the low rate charge curves. In Figure 5.1a, the case for no degradation is shown. The x-axis is normalized to the capacity of the positive electrode. Two characteristic parameters of the half cell and full cell low rate charge curves are defined by Dubarry et al.[140]: the loading ratio LR and the offset OFS. LR is simply the ratio of capacities of the anode to the cathode, i.e. $LR = Q_{NE}/Q_{PE}$. OFS represents the offset, or slippage, between the cathode and the anode. When a cell is assembled, the fully lithiated cathode is aligned with the fully delithiated anode at 0% SOC_{PE}. Typically, after some formation cycles where an SEI is formed and there is loss of lithiated anode, the anode curve (red, Figure 5.1a) shrinks to the left such that an offset OFS between the two electrodes is formed, reducing the amount of lithium that can be cycled in the full cell.

As demonstrated in Figure 5.1b, LLI causes an increase in the OFS between the two electrodes. This can be simply explained by considering the fact that if the anode and cathode both do not lose sites that can intercalate lithium, the width of the PE and NE curves cannot change. Therefore, the decrease in capacity due to lost lithium inventory must result from a shift in the curves relative to each other, resulting in a lower full cell capacity. LAM_{NE} (Figure 5.1c) results in a reduction in the width of the NE half cell curve, whereas LAM_{PE} (Figure 5.1d) results in a reduction in the width of the PE half cell curve.

Based on Figure 5.1a, when the cell is discharged, the sharp drop in cell voltage to reach the lower cutoff voltage at the bottom of discharge can be attributed to the sharp rise in the anode potential. Conversely, during charge, the sharp increase in cell voltage to reach the upper cutoff voltage at the top of charge can be attributed to the sharp rise in cathode potential. Thus, even from the low rate charge curves, we can determine which electrode limits the capacity on both charge and discharge. When there is sufficient LAM_{PE}, the limiting electrode for discharge switches from the anode to the cathode, as seen in Figure 5.1d. On charge, when there is sufficient LAM_{NE}, because the anode reversible potential is flat at high states of lithiation, the upper cutoff voltage will not be reached when the available active material in the anode is fully lithiated (Figure 5.1c). Instead, lithium plating will occur. While this may not immediately lower the capacity under ordinary cycling conditions, after some cycles the adverse effects of lithium plating may accelerate capacity fade.[166,167]

The onset of these phenomena can be described by the following, adapted from References[140] and[168]:

$$OFS = OFS_{init} + LLI - LAM_{PE} \tag{5.1}$$

$$LAM_{NE,PT} = 1 - \frac{1 - OFS_{init} - LLI}{LR_{init}} \tag{5.2}$$

where LR_{init} and OFS_{init} are the initial loading ratio and offset of the electrodes after formation, before degradation, as in Figure 5.1a. These values are scaled to the initial SOC_{PE}, such that Figures 5.1b-d can be compared against Figure 5.1a to verify the applicability of equations 5.1 and 5.2. $LAM_{NE,PT}$ refers to a reversible plating threshold. The limiting electrodes on charge and discharge can then be determined based on the values of OFS and $LAM_{NE,PT}$.

$$\text{Discharge:} \begin{cases} \text{PE limiting if} & OFS \leq 0 \\ \text{NE limiting} & \text{otherwise} \end{cases} \tag{5.3}$$

$$\text{Charge:} \begin{cases} \text{NE limiting if} & LAM_{NE} \geq LAM_{NE,PT} \\ \text{PE limiting} & \text{otherwise} \end{cases} \tag{5.4}$$

Changes in the limiting electrode that occur over the course of cycling, especially the onset of lithium plating, have been linked to "knee-points" behavior in capacity retention,[166,167] so identification of these shifts could serve as valuable information during diagnosis.

In this study, we compare supervised machine learning models and voltage curve transformations for the following tasks: (1) regression of the values of LLI, LAM_{PE}, and LAM_{NE} and (2) classification of the limiting electrode on charge and discharge. The details of the supervised learning approach, including the selection of the training and testing sets, processing of the low rate charge curves, and choice of models are outlined in the following section.

5.3 Supervised Learning Approach

Figure 5.2 provides an overview of the workflow for the trained models in this study. For a given input low rate charge curve, a series of processing steps is taken to extract features. These features are passed to models for prediction of two different kinds of targets. The first target is the simultaneous quantitative prediction of the values of LAM_{PE}, LAM_{NE}, and LLI that correspond to the low rate charge curve input. The second target is the label for which electrode will limit capacity when the cell is subsequently charged and discharged at higher rates. The correct labels for each low rate charge curve are identified using equations 5.1-5.4 with the values of OFS_{init} and LR_{init} provided in Reference[159]. The following subsections outline how subsets of the published data by Dubarry et al. were selected to train these models and subsequently test them, the featurization steps, and the selection of candidate models for the regression and classification tasks.

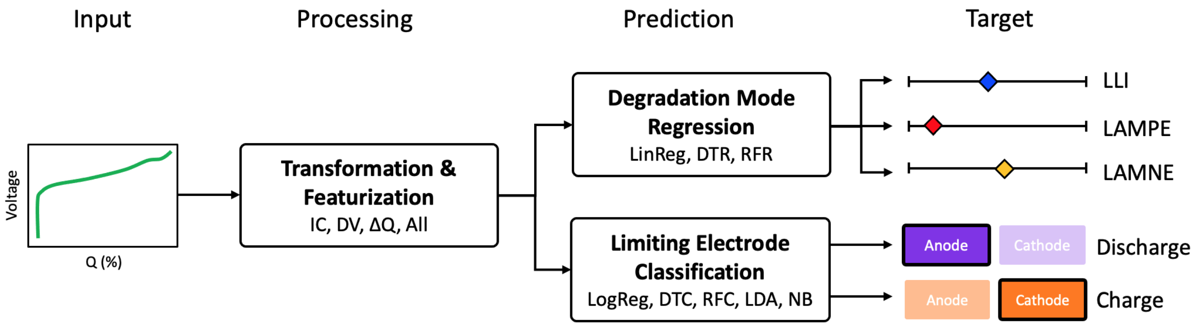

Figure 5.2: An overview of the two prediction tasks for trained models explored in this study. Low rate charge curves are taken as inputs, features are extracted, and predictions are made on the values of the three degradation modes and the limiting electrodes on charge and discharge.

5.3.1 Train and Test Set Selection

The data sets provided by Dubarry et al. include low rate charge curves generated with combinations of LLI, LAM_{NE}, and LAM_{PE} at a resolution of 0.85 % between 0 and 85 % for LFP, NMC, and NCA.[156–158] In total, the number of voltage curves provided exceeded 500,000 for each cell. To reduce times for training and testing, a more sparse subset of the provided data was chosen. The training set was chosen with a resolution of 5 % between 0 and 80 % for each degradation mode, resulting in a training set size of N_{train} = 4,096. This corresponds to 4,096 low rate charge curves and the corresponding 4,096 vectors of $[LAM_{PE}, LAM_{NE}, LLI]$. The testing set was chosen to test the interpolative ability of the models, and therefore was chosen to have a resolution of 2.5 % between 0 and 80 % for each degradation mode, resulting in a testing set size of N_{test} = 32,768.

As exact values of the three degradation modes may not be represented in these sets, the SciPy Spatial KDTree function was used to look up the nearest neighbors for the chosen grid.[169] These samples were used to represent the training and testing sets.

Notably, a validation set was not separately chosen here. These data sets are highly structured, and the training set was designed to span the whole parameter space of interest such that the trained models would be used only for interpolation and not extrapolation. As a result, we allowed our models to learn the dataset without any regularization that may require some hyperparameter tuning. This is discussed further in the model development section.

5.3.2 Featurizing low rate charge Curves

At the low rate charge condition, differential analysis of the voltage curve is known to contain signatures of degradation. Incremental capacity (IC) analysis takes the derivative of the capacity with respect to voltage, emphasizing the voltages at which phase equilibria exist.[170–175] Differential voltage (DV) analysis is the inverse of IC, taking the derivative of voltage with respect to capacity, featuring the transitions between phase equilibria.[172,176–178] Peak intensities, areas, locations can all be use as features to track degradation and for state estimation.[140,142,159,179]

Experimentally, IC/DV analyses may be complicated due to the presence of noise in the data.[161] In addition, some peaks may disappear over the course of aging.[160] An alternative approach that still emphasizes changes in the profile due to degradation was employed by Severson and Attia, calculating the difference in capacity ΔQ as a function of voltage for a degraded voltage profile and the voltage profile before degradation.[149,153]

All three approaches were employed to featurize low rate charge curves, and are shown in Figure 5.3. Figure 5.3a shows the no degradation curve and a degraded low rate charge curve. In Figure 5.3b, the ΔQ curve is extracted by subtracting the two curves in Figure 5.3a at each voltage. Figure 5.3c and 5.3d show the IC and DV curves, respectively.

To translate these curves into a set of features that can be used for machine learning models, 20 evenly spaced points are taken from each curve. For the IC and ΔQ curves, the 20 points are

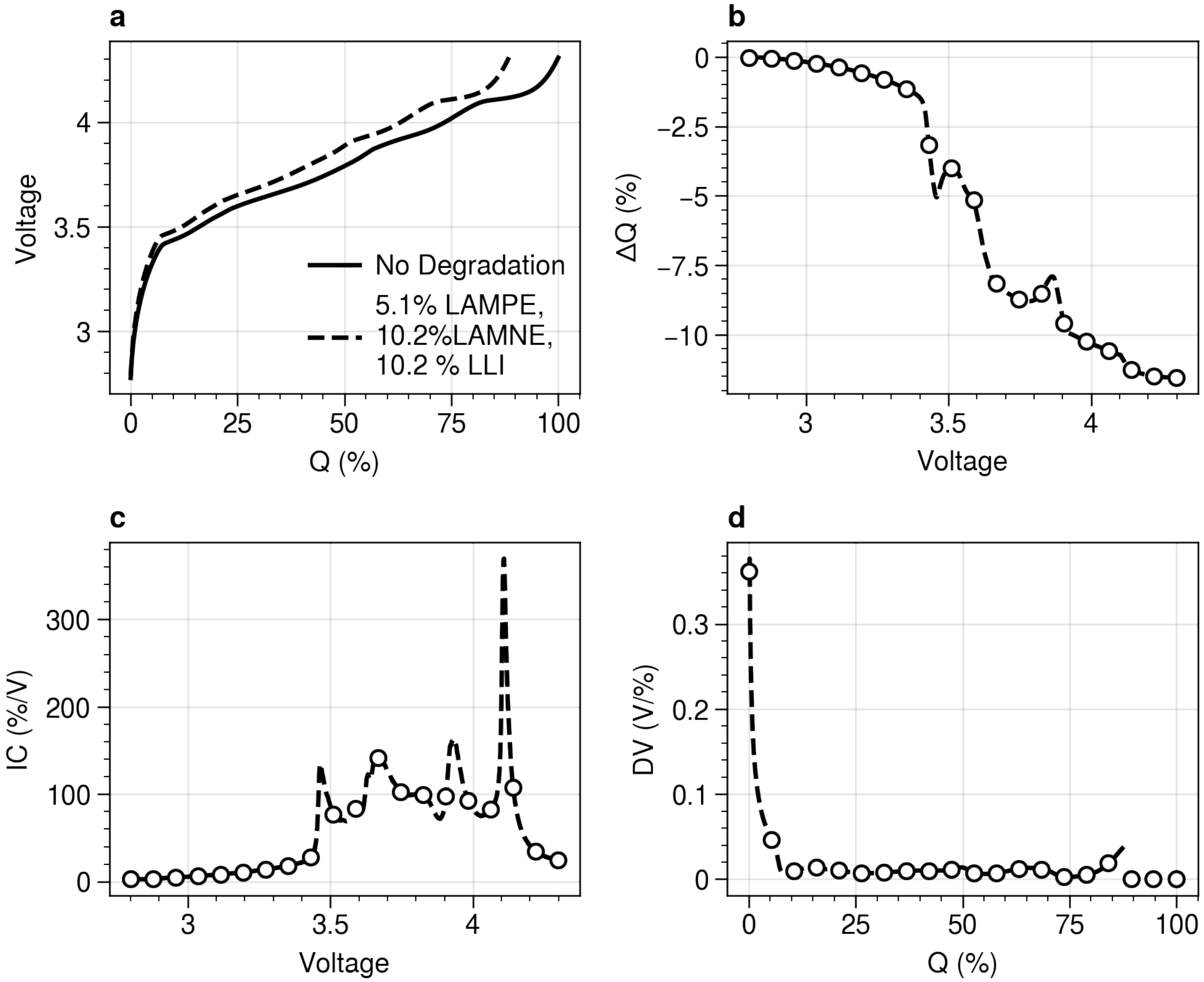

Figure 5.3: Low rate charge curves before and after degradation (a). The processing steps calculating ΔQ, IC, and DV are shown in b, c, and d, respectively. In c and d, the transformations shown are for the low rate charge curve after degradation. The open circles in b-d correspond to the 20 evenly spaced points chosen as features from each curve.

chosen at evenly spaced voltages between the lower and upper cutoff voltages. For the DV curve, the 20 points are chosen at 5 % SOC increments, where the SOC scale goes from 0 to 100 (the maximum capacity delivered before any degradation). One challenge with the DV curve is that when capacity is lost due to degradation, the value of the DV curve at high SOC is undefined. These features are set to 0. Some information is clearly lost in choosing these 20 points, especially in the IC curve in Figure 5.3c.

One key advantage to the approach described here is the automation of discovery of important features from the IC, DV, and ΔQ curves. Expert identification of features from these curves have shown highly accurate results in terms of regressing values of the three degradation modes and for estimating state of health.[159,179] However, extracting these features requires some subjectivity, such as choice of a voltage window to detect a specific peak from which an intensity is extracted. In the present study, if the voltage window is too small, significant degradation may cause the peak to move out of the chosen window. If the window is too large, it may capture multiple peaks. While some have automated peak identification from these differential analyses,[175] allowing the most important features to be determined from the values of these three curves by fitting to the training data offers a simple alternative that removes the need for predefined featurization. An example of this is shown in Figure 5.9, where one peak in the IC curve after degradation disappears entirely, and significant shifts of the other peaks are observed.

Each of these three processing steps was explored individually to determine which gave the most accurate results. In addition to three different types of processing steps, a fourth was included that combines the 20 features from each curve to yield 60 features. This was done by joining the three 20x1 vectors of features into a new 60x1 feature vector. The feature normalization step was done before this concatenation. This was included since a sensitivity analysis on the Dubarry data sets revealed that both IC and DV peaks were correlated with degradation.[159] Discussion on potential overfitting is provided in the results section.

To ensure all features were on the same order of magnitude, the features were rescaled based on the distribution of the feature across all the training samples, a standard practice in feature processing for machine learning. In this case, the MinMaxScaler from the preprocessing module in scikit-learn was used.[180]

5.3.3 Interpretable Models

In the choice of a data-driven model for a supervised learning task, there is often a trade off between model performance and model interpretability.[181] Many machine learning models, such as neural networks, are able to achieve excellent accuracies in regression and classification, but lack the ability to explain the relationship between the input features and the target being predicted. To this end, we specifically consider machine learning models that are inherently interpretable, and look to establish the baseline performance of these models relative to the state of the art. As pointed out by Attia et al., who applied interpretability-focused statistical learning approaches to remaining useful lifetime prediction, these simpler models can serve as a baseline to more powerful but less interpretable techniques like deep learning.[153]

In order to regress values of the three degradation modes, we employ linear regression and two tree-based models - decision tree and random forest regressors. In linear regression, a weight is assigned to each feature such that the linear sum of the products of each feature and corresponding weight predicts the target. The weight for each of the features is readily interpreted to provide information about the degree of correlation of its feature with the target.

Tree-based methods often outperform linear models when features are highly correlated and the relationship between features and the target is nonlinear.[181] Decision trees take the approach of segmenting the feature space into regions based on threshold values, an approach that is analogous to human decision making and is therefore useful for interpretation. Feature importances can be assigned during fitting based on the improvement in predictive performance for a segmentation of the features. Random forests take subsets of the available features and subsets of the training samples, fit individual decision trees to each subset, and average the results. This process, known as bagging, reduces the high variance of an individual decision tree.[135]

Classification of the limiting electrode is a multilabel task, with two labels that have two classes each (discharge and charge, positive or negative electrode limiting). The same tree-based models that are used for regression are capable of multilabel classification as well, and are used. In addition, several other interpretable classification models are used, including logistic regression, linear discriminant analysis, and Naive Bayes.[181] The reader is referred to references[135] and[180] for more detailed descriptions of these models.

We do not include regularization in these models. Regularization, or shrinkage, involves including a penalty during the fitting of a model that excludes or reduces the effect of redundant features. Regularization helps ensure that models do not overfit to the training data, especially when there are many features of the model. Regularization can also help with interpretability by identifying the most important features. However, because of the highly structured nature of the synthetic data set and the interpolation-only objective, we did not include any regularization in our models. For linear models such as linear regression, logistic regression, and LDA, L1/L2-norm penalties were not applied. For the tree-based methods, minimum depth or tree pruning were not considered.[135]

All models in this study were implemented via scikit-learn in python.[180] A full table of the models used in this study is provided in Table 5.1. For the random forests, the default settings in the scikit-learn implementation (e.g., 100 trees) were used. For the interpretation of model weights in linear regression and logistic regression, standard errors for the feature weights are not returned by scikit-learn. These standard errors are required for determination of feature importance, and are calculated using the linear and logistic regression implementations in statsmodels python module.[182]

5.4 Results

5.4.1 *Degradation Mode Regression*

The results of the regression using the different models and processing conditions are shown for each degradation mode and material in Figure 5.4. The results are provided as root mean

Table 5.1: Summary of regression and classification models used. All models were implemented using scikit-learn.[180]

Algorithm	**Abbreviation**	**Notes**
Linear Regression	LinReg	Multioutput Regression
Decision Tree Regressor	DTR	Regression
Random forest Regressor	RFR	Regression
Decision Tree Classifier	DTC	Multilabel Classification
Random forest Classifier	RFC	Multilabel Classification
Logistic Regression	LogReg	Multilabel Classification via Binary Relevance
Linear Discriminant Analysis	LDA	Multilabel Classification via Binary Relevance
Naive Bayes	NB	Multilabel Classification via Binary Relevance

square errors (RMSE), in units of %. RMSE is chosen here as a more conservative metric since it penalizes larger errors more.

The model-processing combination that yields the lowest RMSE in each heatmap in Figure 5.4 is outlined in red. Across the board, linear regression models appear to underperform relative to the tree-based models, likely because the latter are better suited to handle the nonlinear relationship between the features and the degradation modes.[135,181] For most cases, random forests trained on IC features perform the best. These results indicate that random forests improve on the generalizeability of the decision trees. This can be seen in Figure 5.10, which compare testing and training errors. The random forest results consistently have slightly higher training error but a lower test error. Amongst the linear models, the inclusion of DV features leads to overfitting in LFP, but for the other materials and featurization steps, the poor performance can be attributed to the use of a linear model itself. Regularization would likely not improve performance.

Other than the case described above, models trained on DV features tend to not perform as well. This is because the valuable information in DV curves include features like the distance between peaks,[159,176,183] which cannot be captured in our simple featurization methodology. As discussed in the example of incremental capacity analysis, knowledge of which peaks to choose to calculate peak differences requires some knowledge of which peaks are informative a priori, as many local maxima can be found (see Figure 1 in Reference[159]). Our approach forgoes this process entirely by taking 20 evenly spaced features from each DV curve, and is able to achieve accuracies on the order of 10% RMSE. A more nuanced featurization approach that takes into account distance

Figure 5.4: RMSE results, in units of %, for each degradation mode (columns) and each active material (rows). Within each heatmap, regression results are compared for each model (y-axis) and processing condition (x-axis). The model-processing combination that yields the lowest RMSE in each heatmap is outlined in red.

between DV peaks will achieve better accuracies at the cost of more expert knowledge. Also of note is the performance of models trained on ΔQ features, which are often second best to the IC features. While some accuracy is forfeited, the avoidance of having to calculate derivatives and deal with disappearing peaks may render this approach useful in practice.

Compared to the results from the models and features proposed by Dubarry et al.,[159,179] which are able to diagnose the degradation modes to within 1 % using a lookup table, the best interpretable models used here can only diagnose degradation modes to within 2 to 7 %, depending on the degradation mode and material. While the expert-defined features predetermined to be correlated with the degradation modes can be expected to be more predictive, a direct comparison cannot be made because a much larger training set was used to build the lookup table used for diagnosis in Ref.[159]. The accuracies achieved here without having to calculate peak areas of convoluted peaks or specify voltage or capacity ranges for identifying peaks are notable.

5.4.2 Limiting Electrode Classification

The results of the evaluation of the various classification models and the processing conditions for the detection of the limiting electrode on (dis)charge in the test set are shown in Figure 5.5. The *x*-axis shows the accuracy for predicting the limiting electrode on charge, and the *y*-axis shows the accuracy for predicting the limiting electrode for discharge.

Some key takeaways emerge from Figure 5.5. It appears that most of the models and processing conditions can achieve accuracies as high as 90 %. Because the training set spanned such a wide space of low rate charge curves and extrapolation was not a concern on the test set, it appears that with enough training data, several models will perform well. The results for all the models are provided in Figure 5.11.

As with regression of the degradation modes, the best performing model-processing combination across all materials is the random forest trained on the IC features. The results for this model for each cell is shown in Table 5.2. In addition to the classification models considered, classification based on the regression estimates were also performed, as a baseline to test the need for

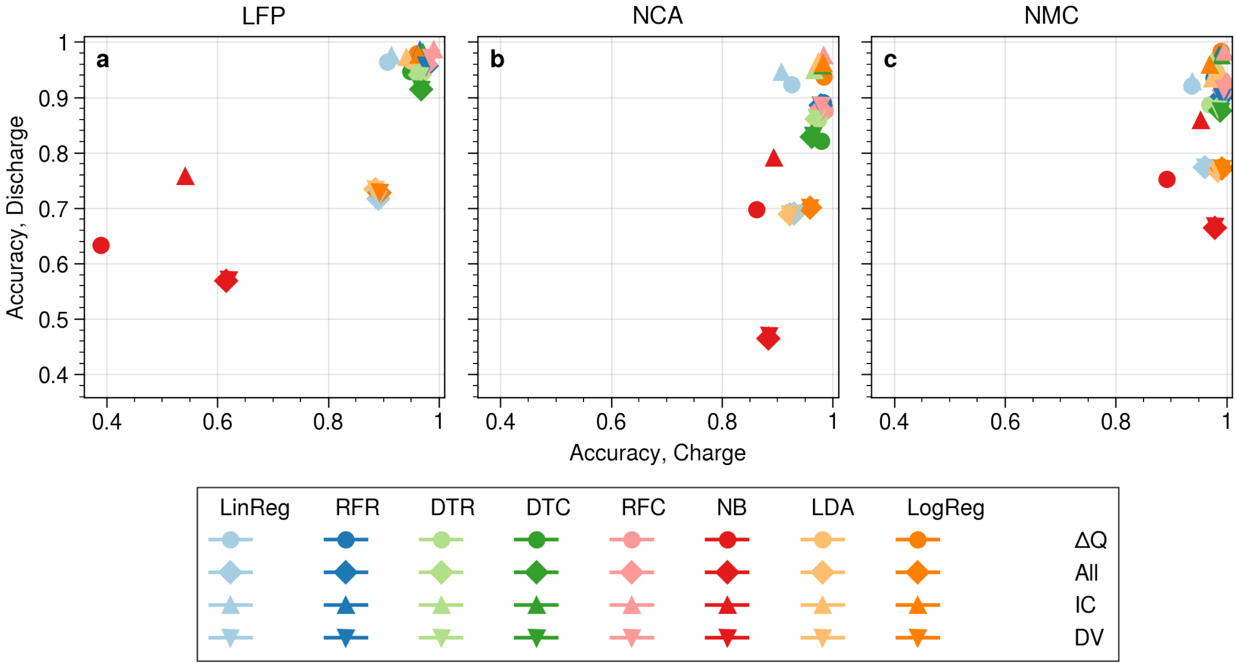

Figure 5.5: Limiting electrode classification accuracies for charge and discharge for LFP (a), NCA (b), and NMC (c).

classification at all. If LAM_{PE}, LAM_{NE}, and LLI can be estimated with high accuracy, Equations 5.1-5.4 can be used to classify the limiting electrodes. The random forest classifier trained on the IC features slightly outperforms the regression models for the limiting electrode classification task.

Table 5.2: Classification results for the Random Forest Classifier trained on incremental capacity features.

	Discharge	Charge
LFP	99.1%	98.6%
NCA	98.4%	97.6%
NMC	99.6%	98.3%

5.4.3 Interpretation of Trained Models

In this section, we look to interpret the trained models to gain some understanding of the learnings of these models.

First, we look at the weights from linear regression, as they are the easiest to understand. Since the linear regression models do not perform very well compared to the tree-based methods, the identified features should be taken with caution. To illustrate an example of feature importance

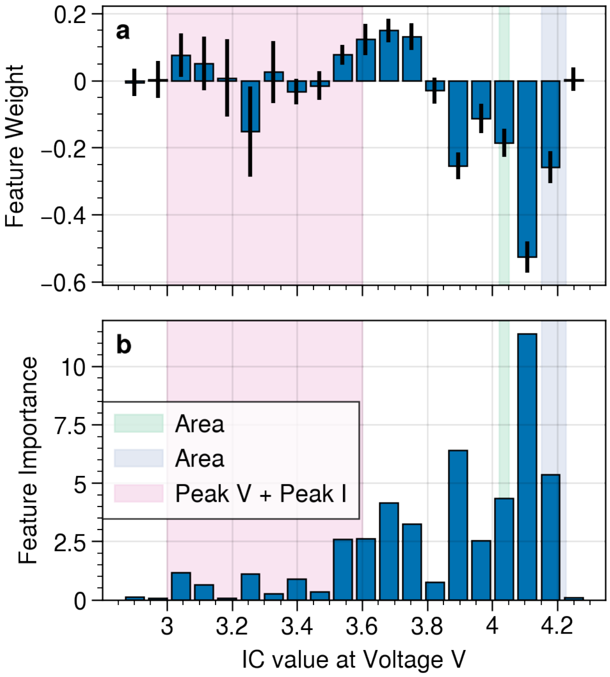

Figure 5.6: Coefficients and feature importances for a linear regression model trained on IC features to predict LAM_{PE} in NCA, which yielded an RMSE of 7.35 % on the test set. The shaded regions indicate the specified voltage window over which features were calculated from the IC curve in reference[159]. The legend indicates what feature was calculated in that voltage window, e.g. area under the IC curve (Area) in the voltage window, intensity of the IC peak in the voltage window (Peak I), or the voltage at which an IC peak is observed in the voltage window (Peak V).

from linear regression, we look at the linear model used to regress LAM_{PE} in NCA using IC features, which yielded an RMSE of 7.35 %.

Figure 5.6a shows the weights of each feature in the linear model, which indicates the correlation of the IC value at each of the 20 voltages to the value of LAM_{PE} in NCA. Each estimated weight also has an associated standard error, given by the error bars. The feature importance of a linear model can be calculated by dividing the magnitude of the weight by its standard error. Therefore, weights that are known more precisely are given more importance while weights that are not known precisely are rendered less important. The results of this transformation are shown in Figure 5.6b.

Also on Figure 5.6 are the features from the IC curve used by Dubarry et al., delineated in Reference[159]. These features include peak locations, peak intensities, valley (local minima) locations, valley intensities, and peak areas in predefined voltage windows. Specifically, the authors find that three features are predictive of LAM_{PE} in NCA: (1) the intensity and voltage location of the IC peak between 3.0 and 3.6 V (Peak V + Peak I, pink), (2) the area underneath the IC peak between 4.02 and 4.05 V (area, green), and the area underneath the IC peak between 4.15 and 4.225 V (area, blue). These voltage windows and quantities are shown in the background of Figure 5.6.

The direct comparison between the feature importance identified here and by Dubarry et al. can only be made qualitatively, since these features are merely intensity values at discrete voltages. Some notable alignments are observed with the peak intensity features above 4 V. The two corresponding area features in Dubarry et al.'s approach are the two most correlated to LAM_{PE}. Instead of the peak intensity and location between 3 and 3.6V, our analysis identifies peak intensities between 3.5 and 3.8 V as predictive features for LAM_{PE}.

Next, we examine feature importance from the random forest regressors trained on IC features, which performed the best at regressing the three degradation modes. Feature importance is determined by the total improvement in training error due to segmentation of each feature averaged over each tree in the random forest.[135]

The feature importances for the best trained model for each cell are shown in Figure 5.7. As

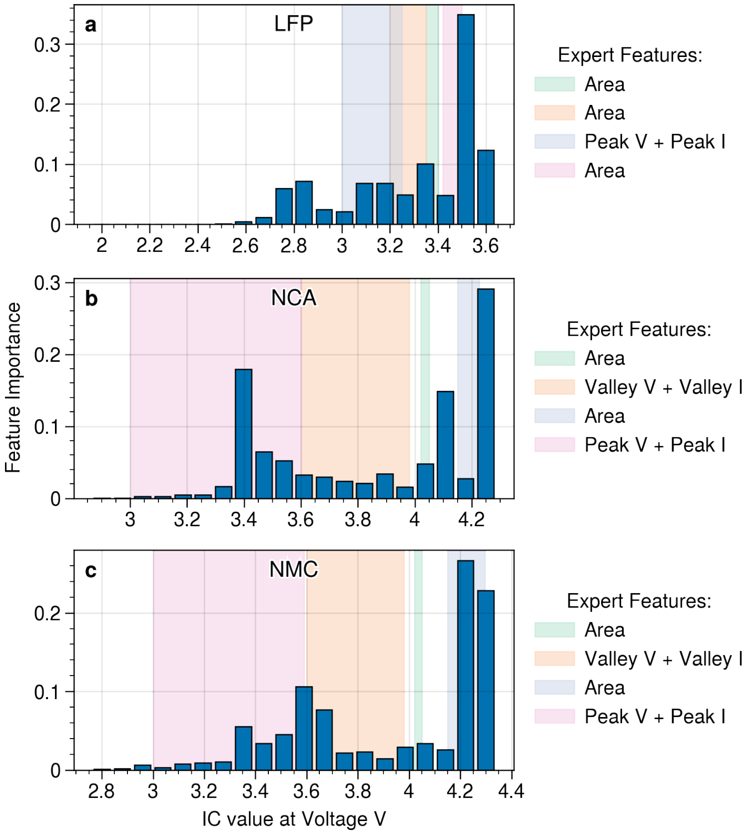

Figure 5.7: Feature importance for random forest regressors trained on IC curves for LFP (a), NCA (b), and NMC (c).The shaded regions indicate the specified voltage window over which features were calculated from the IC curve in reference[159]. The legend indicates what feature was calculated in that voltage window, e.g. area under the IC curve (Area) in the voltage window, intensity of the IC peak or minimum in the voltage window (Peak I, Valley I), or the voltage at which an IC peak or minimum is observed in the voltage window (Peak V, Valley V).

with the linear regression results, the voltage windows and IC curve features in those voltage windows as defined by Dubarry et al. are shaded in the background of Figures 5.7a-c and labeled to the side of each subplot. Unlike linear regression, random forest regression allows for simultaneous prediction of all three degradation modes, so we cannot correlate a feature with a degradation mode. Rather, we can see which features are most important in determining the specific combination of $[LLI, LAM_{PE}, LAM_{NE}]$. In some cases, the features determined to be important in this analysis are consistent with the expert analysis. For example, the IC features at the higher voltages are most important in our analysis, and the peak area at these voltages were chosen as features by Dubarry et al. However, at voltages where the published analyses identified IC valley intensities and locations as important features (i.e. between 3.6 and 3.98 V for NMC), our analyses did not identify important features.

Finally, we look at an example of feature importance from the classification task. We take the example of detection of the limiting electrode on charge. This task is related to the detection of reversible plating as described in Reference[159]. The results of the logistic regression model trained on IC features to predict the limiting electrode on charge in NMC are shown in Figure 5.8 as an example. The logistic regression model achieved an accuracy of 94 % for this classification task (Figure 5.11f).

As with the linear regression example in Figure 5.6, we have the feature weights in panel a and the importances, calculated by dividing the magnitude of the weight by its standard error, in panel b. The shading corresponds to the voltage window in which the IC peak area is expected to correlate with reversible lithium plating in Reference[159]. The logistic regression model also identifies the IC intensity features in this voltage window as important, along with some other features in the lower voltages. Figure 5.6 also offers an example of an important caution when interpreting weights in linear models. A larger weight does not necessarily mean a larger feature importance. In Figure 5.6a we see a large negative weight followed by two smaller positive weights at higher voltages. However, the standard error on the positive weights are much smaller than that of the negative weight, so their feature importance is much more.

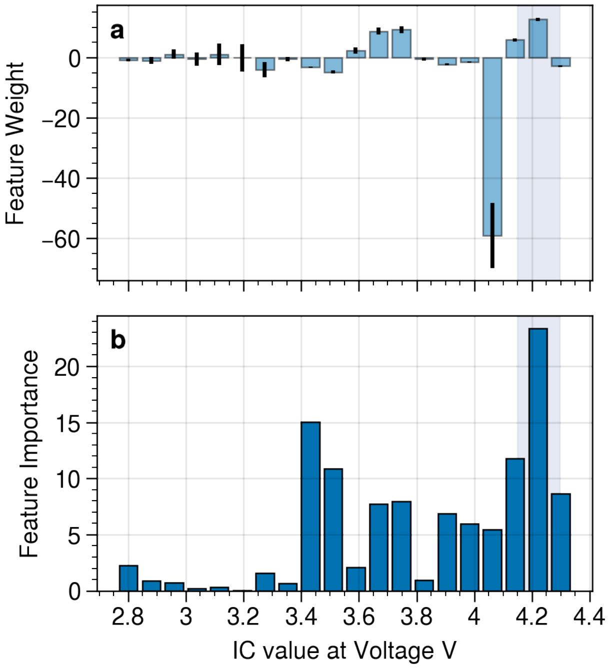

Figure 5.8: Weights and feature importances for a logistic regression model trained on IC features to predict the limiting electrode on charge in NMC. The shading corresponds to the voltage window in which the IC peak area is expected to correlate with reversible lithium plating in Reference[159].

5.5 Outlook

The results presented here, while promising, can likely be improved through method optimization. A larger training set could be used, and preliminary analysis shows that the featurization of IC, DV, and ΔQ curves into more than 20 features can provide some marginal improvements as well. However, results seem to indicate that the random forests trained on IC show the most promise for both regression of the degradation modes and the limiting electrode classification problem.

The utility of the methodology presented in this study will depend on knowledge of the cell specifications, the variability in cell-to-cell behavior, and experience with certain active materials. For example, if the offset and loading ratio are known initially, fitting an OCV model that is parameterized by the three degradation modes may be sufficient.[161] If the expected voltage or capacity windows for IC or DV peaks are well known, then more nuanced features can be defined and selected to give better predictive performance than is shown here.[159,179] The value of the approach presented here is that without any knowledge of the behavior of the system other than the post-formation loading ratio and offset, decent performance can be achieved alongside some interpretability of the features that are most predictive of changes in the cell.

One limitation of this approach and other similar near OCV estimation approaches is that the results are highly dependent on the initial loading ratio and offset value being known. To make these approaches more robust from a cell-to-cell variance perspective (all cells will of course not lose the same amount of material and lithium inventory during formation, for example) some of this sample to sample variance could be incorporated into the training data by including a distribution of OFS_{init} and LR_{init} values from which to choose for a specific simulated low rate charge curve. This would then better replicate cell to cell variance, and with some regularization, important features that stand out over this variation could be identified.

Finally, only thermodynamic degradation modes are explored in the data set used for model development here, but increase of resistances in cells can also be explored using this type of analysis.[140] Expanding the design space for synthetic voltage curves to include different experimental conditions that go beyond the C/25 charge will be informative in diagnosing resistance increase in addition to loss of active material and loss of lithium inventory.

5.6 Conclusions

The above study provides the detailed implementation of a machine learning analysis of a synthetic big data set containing low rate charge curves generated from different combinations of thermodynamic degradation modes. Synthetic voltage curves allow for a faster exploration of the entire range of outcomes due to all the different combinations of degradation modes, a space that may be too large to explore experimentally. Training machine learning models to learn the relationships between the outputs from a physics based or mechanistic model, which mirror experimental observations, and the physical parameters used to generate that synthetic data can enable more physically relevant state estimators that provide a better understanding of the evolution of the system.

Here, we report performance of interpretable machine learning models for regression of degradation modes and classification of the limiting electrode on charge and discharge. Random forests are shown to outperform linear regression for estimation of the degradation modes. Based on the comparison of different featurizations of the low rate charge curves, we find intensities of incremental capacity analysis to be informative. The performance of the models reported here can serve as benchmarks for more complex machine learning models such as neural networks. Finally, the understanding gained from the trained models is analyzed, and compared to expert-identified features, some of which are recovered in our machine learning analysis. The code to reproduce the results of this study is available in a github repository online.

5.7 Supporting Information

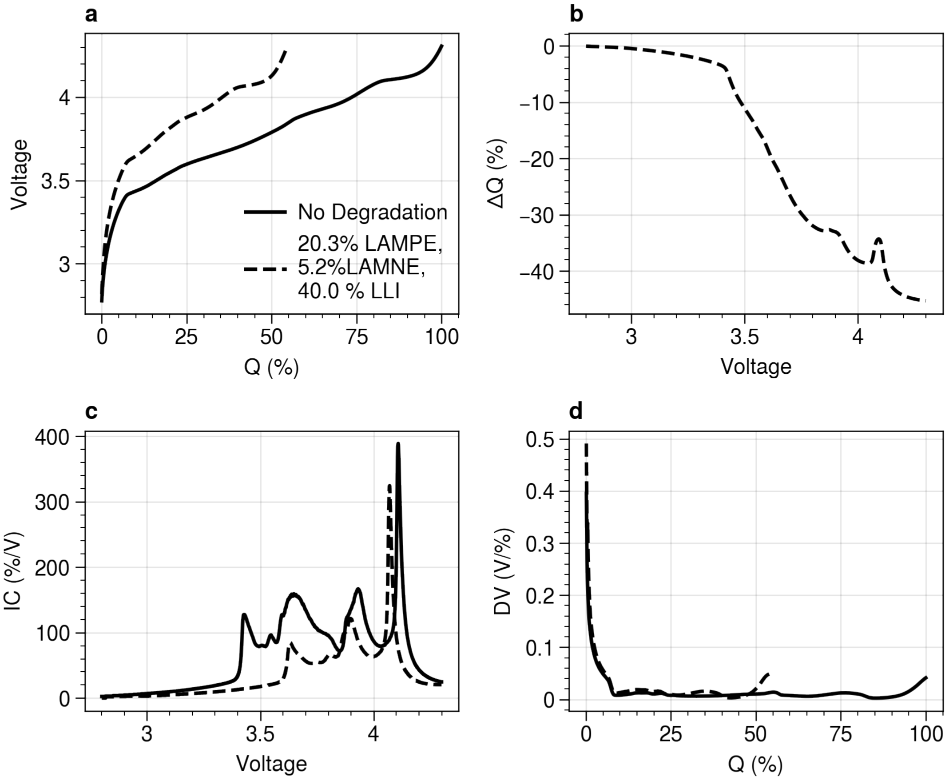

Figure 5.9: Exemplary low rate charge curves before and after degradation (a). The processing steps calculating ΔQ, IC (dQ/dV), and DV (dV/dQ) are shown in b, c, and d, respectively.

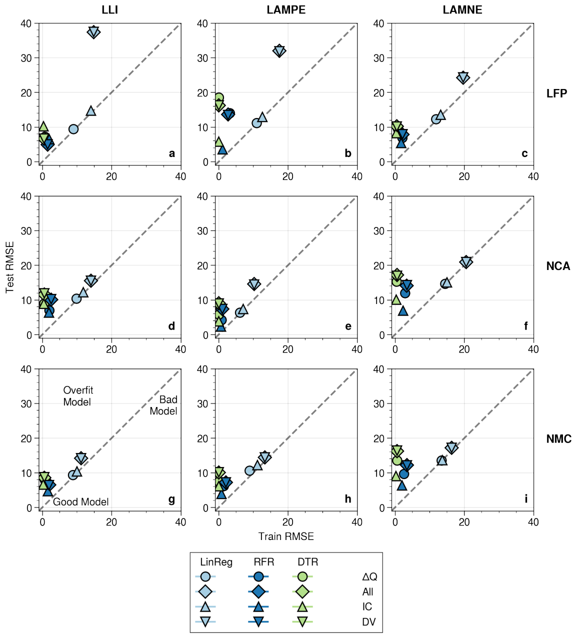

Figure 5.10: RMSE, in units of %, for each degradation mode (columns) and each active material (rows). Within each plot, the test set results are plotted against the training set results, with a diagonal line indicating equal performance.

Figure 5.11: Classification accuracies for limiting electrode detection. The columns represent limiting electrode detection results for discharge (left, greens) and charge (right, yellows), and each of the three rows is for a specific cell. Within each heatmap, classification accuracies are compared for each model (y-axis) and processing condition (x-axis). The model-processing combination that yields the lowest MAE in each heatmap is outlined in red.

Chapter 6

Parameter Estimation for Electrode Degradation: Learning in the Face of Model-Experiment Discrepancies[*]

---

[*] This Chapter has been published: Karthik. S. Mayilvahanan, Jwal. R. Soni, Kenneth. J. Takeuchi, Esther. S. Takeuchi, Amy. C. Marschilok, and Alan. C. West, “Parameter Estimation for Electrode Degradation: Learning in the Face of Model-Experiment Discrepancies,” *Journal of the Electrochemical Society*, vol. 169, no. 5, p. 050517, May 2022.
The thesis writer’s contribution was ideation, implementation of ML models, analysis and writing.

6.1 Introduction

Developing an understanding of degradation in Li-ion batteries is essential for diagnosing poor cells before catastrophic failure, developing safer usage protocols, and designing materials with the aim to minimize degradation rates. Approaches to gain this understanding vary widely in both physical insight and ease of implementation. Those focused on state of health estimation in onboard applications prioritize fast algorithms to estimate capacity and internal resistance.[184] Research and development teams less concerned with speed and more interested in detailed physical insight may turn to *operando* materials characterization or even destructive postmortem cell tear downs.[163,185,186]

One approach presented in the literature that balances these two ends of the spectrum is to fit physics-based electrochemical models, such as the single particle model (SPM) or the pseudo-2D model (P2D), to cycling data. This is done by refitting parameters in a model that describes the physics of a battery before any cycling to describe the physics at later cycles. This approach has been used to estimate the evolution of the initial states of charge of the cathode and anode over the course of cycling from discharge curves.[130,131] Similar analyses have been reported that also track the change in parameters describing transport in the active material and electrolyte domains as well as those describing the kinetics of charge transfer.[132,133] A criticism of this approach may focus on an over-reliance of imperfect models to extract information from simple but nonideal measurements.

In efforts to make these analyses more useful in terms of speed and ease of implementation, the combination of physics-based models with machine learning (ML) has been proposed.[154] One approach could be to replace a physics-based model with a faster surrogate ML model that can take inputs and generate the same outputs as a traditional physics-based model like voltage and concentration distributions. If the forward surrogate ML model is fast enough, it can be wrapped in traditional optimization algorithms to return parameter estimates quickly. However, this type of model can be challenging because it may be difficult to ensure constraints like monotonically changing outputs.[187] Instead, inverse surrogate ML models, which map a physics-based model output like voltage to parameters used to generate those outputs, offer an approach to leverage the power of ML in fitting physics-based models.[187–189] These inverse ML models are trained on synthetic, physics-based model-generated data offline and then used to optimize parameters of the model for new sets of experimental data.[159,160,190] A schematic of the inverse surrogate ML model approach is shown in Figure 6.1.

However, the performance of these ML models is constrained by the training data. While some ML models have better extrapolative ability (i.e. the ability to make predictions outside the scope of the training data), most models are most effective at interpolating between the training data.[13] To ensure that inverse surrogate ML models are interpolating, an expansive training set that covers a wide parameter space is best.[155] Still, if the underlying physics-based model itself is not able to explain the experimental data, the ML models trained offline on synthetic data may remain inaccurate when applied to experimental data.

In this paper, we explore the degree to which ML approaches can reduce the impact of discrepancies between physics-based models and experiments in the context of physical state estimation. We build on our previous model development and degradation analysis of lithium trivandate (LVO), a mid-voltage cathode that incorporates a phase change and simultaneous Li-ion intercalation into both phases.[32,42,64,165] Featurization of synthetic data, training of neural networks as inverse surrogate ML models, and a data augmentation strategy to improve the robustness of these neural networks are discussed. Two cases of model-experiment discrepancy show how ML models perform relative to a maximum likelihood approach in the face of these discrepancies.

6.2 Methods

6.2.1 *Generating and Featurizing Synthetic Training Data*

This study follows a previous study on degradation of half cells with LVO cathodes cycling at 0.2C. Based on published studies of LVO cathodes, the space of parameters that evolve with

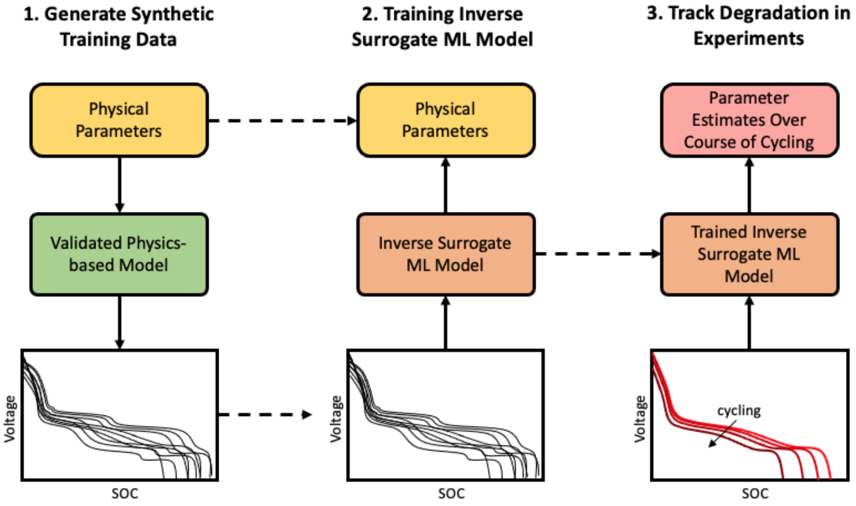

Figure 6.1: Schematic of an inverse surrogate ML model trained on synthetic voltage curves generated by a physics-based model.

Table 6.1: Model parameters considered and the range of sampling.

Model Parameter	Symbol	Range	Units
% of nominal amount of active LVO	%AM	[0.5,1.0]	%
Li diffusivity in α phase	$log_{10}D_{\alpha}$	[-14.0,-11.0]	cm^2s^{-1}
Li insertion rate constant in α phase	$log_{10}k_{rxn,\alpha}$	[-8.0,-6.0]	$cm^{-5/2}mol^{-1/2}s^{-1}$
Li diffusivity in β phase	$log_{10}D_{\beta}$	[-15.5, -13.0]	cm^2s^{-1}
Li insertion rate constant in β phase	$log_{10}k_{rxn,\beta}$	[-9.5, -7.0]	$cm^{-5/2}mol^{-1/2}s^{-1}$

cycling at this rate was narrowed to five parameters, summarized in Table 7.1.[55,58,70,124,129,165] These parameters are known to be identifiable at this discharge rate and within these bounds.[165]

Sobol sampling was used to efficiently sample the five dimensional parameter space, implemented using Scipy.[191] A total of 1,024 unique combinations of the five parameters were created and passed to the physics based model to create the corresponding discharge voltage curves. The 1,024 simulations were filtered for simulations that did not run into numerical issues and were lithiated to at least 10 % depth of discharge by the time the lower cutoff voltage was hit, yielding 710 simulations. It should be noted that this is a relatively small training set size compared to our previous work and the amount of synthetic data generated by others for inverse surrogate model training.[155,159] The resulting accuracy metrics are not an upper bound, but rather should be considered in relation to different estimation approaches using the same data set.

To convert a continuous curve to a set of features that can be passed into a ML model, we take an approach used by Severson and Attia.[149,153] Most curve-fitting studies fit voltage curves to minimize the error in voltage. However, in this study, curves are fit to minimize error on the x-axis (i.e. time, state of charge, or capacity). In standard experiments within the scope of this study, the voltage window for cycling is fixed. We can take advantage of this by discretizing a voltage curve using values of the time at voltages evenly spaced by 1 mV between the upper and lower voltage cutoff limits. The time values are multiplied by the c-rate (C_r), resulting in feature values (tC_r) on the order unity. This transformation is done for simplicity, in preparation for future work extending this approach to multiple c-rates, and because features of order unity are preferred in certain ML models.[192] The impact of the feature resolution on the model accuracy was also considered,[153] since lower feature resolution (i.e. features spaced out by 100 mV as opposed to 1mV) could be a way of acknowledging some nuance in the experiments is not captured by a physics based model. This feature resolution did not significantly impact results when testing against the synthetic data in this study. Details of this analysis are provided in the Supporting information (Figure 6.10 and Figure 6.11).

6.2.2 ML Model Training

A deep neural network (NN) was used as the inverse surrogate ML model. Other ML models such as multi-output linear regression and random forest regression have been used as inverse models and can be trained much faster than NNs.[187,190] NNs were chosen for their superior ability to learn the training data and interpolate between them.[192] Training of NNs was implemented using keras, a python-based deep learning interface.[193] Features passed into the NNs were already on the order of one, but as the parameters being regressed were not, the MinMaxScaler from scikitlearn was used to scale these parameters.[**scikit-learn**] The KerasTuner tool was used to optimize the number of hidden layers and the number of nodes per layer in the NN. The optimized network was then trained for 1200 epochs with a batch size of 128, with a 20% validation split. An adaptive learning rate was also applied such that when learning stagnated during training, the learning rate was reduced to further improve model performance. The NN trained on the original training set with no feature engineering is referred to throughout the text as NN_{base}. Further details about the implementation can be found in the accompanying code on github.

In some case studies, we found that NN_{base} would output physical parameters with unrealistic values. An example of this is shown in Figure 6.2, where the NN_{base} trained on an imperfect physics-based model is used to estimate physical parameters from a synthetic experimental voltage curve. The parameter predictions are passed back through the physics-based model and the resulting voltage curve (gold) clearly differs significantly from the synthetic experiment. Examples like the one in Figure 6.2 motivated us to pursue strategies to improve the robustness of NNs for parameter estimation, namely data augmentation.

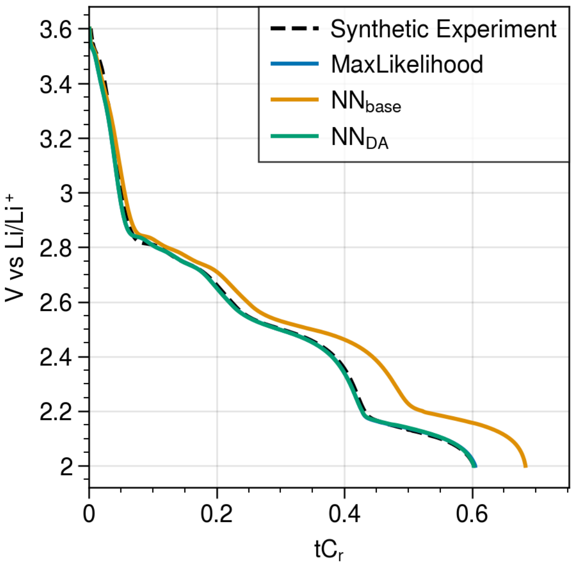

Figure 6.2: Voltage curves for an exemplary synthetic experiment and the resultant voltage curves that correspond to parameter estimates from estimators that are trained on an imperfect physics-based model (see Simulating Experiments with Discrepancies and Figure 6.4).

Data augmentation is the addition of different amounts of noise to the training data to increase the size of the training set, and is illustrated graphically in Figure 6.3. In most use cases, data augmentation is implemented by adding random noise to the features, combatting overlearning of the training data. However, adding random noise to the current set of features would create unrealistic discharge curves that would not decrease monotonically. Instead, a systematic shift is introduced. A random value of tC_r is sampled from a uniform distribution between 0 and 0.15. This number is added to all the features in the curve, effectively shifting the curve forward in time by some amount. This type of shift could replicate cases where the model is unable to capture physics at the beginning of a discharge.

For a set of training data that includes M discharge curves, M different numbers are sampled from the uniform distribution and are added to the M discharge curves. This procedure can be repeated multiple times, choosing a new set of M random shifts each time and thus multiplying the training set size. By adding this systematic noise, NNs are taught not to overly rely on the absolute value of the features in predicting the output parameters, but rather to use relative values of the features (i.e. the shape of the discharge curve). By adding different shifts to the same original discharge curve, the training set size can be inflated to much larger sizes without having to do any more evaluations of the physics based model. Both benefits improve the robustness of the NNs.

In our results, we compare the performance of NNs trained on the original synthetic data set (NN_{base}) to NNs trained on an augmented synthetic data set (NN_{DA}). We also quantify the performance improvement for different degrees of data augmentation in the Supporting Information (Figure 6.12). In the main text of this paper, we present results for a training set that has been increased to 8x the original size using the data augmentation approach. A feature resolution of 100 mV is used for this model to reduce training time. For the specific synthetic experiment in Figure 6.2, it is clear that the estimated parameters by NN_{DA} are more accurate than that of NN_{base}, as the resulting voltage curve falls on top of the synthetic experiment voltage curve. While this is only one specific example chosen to illustrate the potential of inaccuracy of NN_{base}, results are presented that show that over a large and diverse set of testing data, NN_{DA} is more accurate than NN_{base} (Figure 6.8).

In addition to this comparison, both models are compared to a baseline maximum likelihood analysis using the training data, the details of which are provided in the Supporting Information.[71] It is important to note that while the physics based model could have been wrapped in an optimization algorithm which would yield more accurate estimates than those reported in the Results section for this maximum likelihood analysis, it would involve several evaluations of the physics-based model for each new set of experimental data for which parameters need to be estimated. Instead, we provide a baseline that uses the exact same set of data used to train ML to estimate parameters, and aim to show that the ML models are able to make better use of simulations generated by a fixed number of evaluations of a physics-based model.

An independent test set was used to test accuracies of the ML models. The simulations were in the same parameter bounds listed in Table 7.1, and therefore specifically tested the interpolative ability of the models.

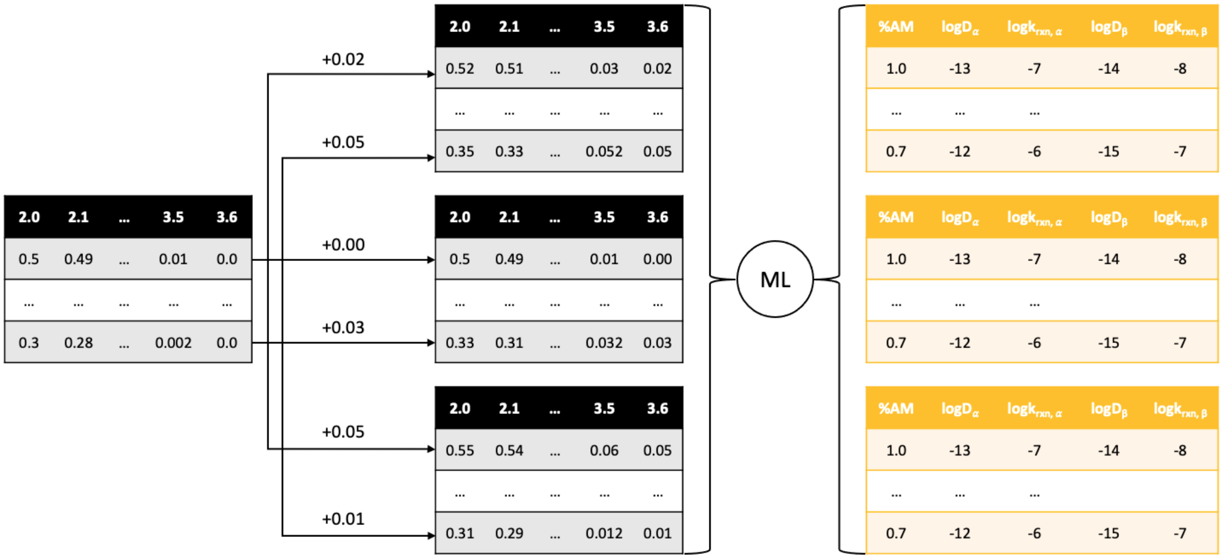

2.0	2.1	...	3.5	3.6
0.5	0.49	...	0.01	0.0
...	...	...	...	...
0.3	0.28	...	0.002	0.0

2.0	2.1	...	3.5	3.6
0.52	0.51	...	0.03	0.02
...	...	...	...	...
0.35	0.33	...	0.052	0.05

2.0	2.1	...	3.5	3.6
0.5	0.49	...	0.01	0.00
...	...	...	...	...
0.33	0.31	...	0.032	0.03

2.0	2.1	...	3.5	3.6
0.55	0.54	...	0.06	0.05
...	...	...	...	...
0.31	0.29	...	0.012	0.01

%AM	$\log D_{\alpha}$	$\log k_{rxn,\alpha}$	$\log D_{\beta}$	$\log k_{rxn,\beta}$
1.0	-13	-7	-14	-8
...	...	...		
0.7	-12	-6	-15	-7

%AM	$\log D_{\alpha}$	$\log k_{rxn,\alpha}$	$\log D_{\beta}$	$\log k_{rxn,\beta}$
1.0	-13	-7	-14	-8
...	...	...		
0.7	-12	-6	-15	-7

%AM	$\log D_{\alpha}$	$\log k_{rxn,\alpha}$	$\log D_{\beta}$	$\log k_{rxn,\beta}$
1.0	-13	-7	-14	-8
...	...	...		
0.7	-12	-6	-15	-7

Figure 6.3: Graphic illustrating data augmentation implementation in this study. Each voltage curve is represented by a value in a table, where the columns correspond to the voltage at which the feature value is tabulated. A systematic shift, the value of which is chosen randomly, is applied to each curve. This process is repeated with different values of shifts for each curve (i.e., row in the training set table) to triple the training set size.

6.2.3 *Simulating Experiments with Discrepancies*

We consider two possible cases of discrepancies between experiment and physics-based model. The first is a situation where the assumptions required for the model analysis are not met by the experimental protocol. In the current analysis, we look at discharge curves to estimate parameters that describe the physical state of the system. Ideally, all other parameters in the system are known and remain unchanged. While some experimentation and dimensional analysis can identify these parameters precisely and render other parameters insensitive to the experiment,[189] others may meaningfully impact the discharge voltage curve, and assuming incorrect values for them could lead to inaccurate estimates of the desired parameters.

The state of lithiation in the cathode at the beginning of a discharge is explored as one of these parameters. In standard cycling experiments, it is often practice to include a constant voltage hold at the top of charge to fully delithiate the cathode before the subsequent discharge. A rest (current turned off) step after this constant voltage hold can be used to track the open circuit voltage of the cathode before each discharge, which can be mapped to a state of lithiation (SoL) using the equilibrium voltage curve. However, these steps will extend the time required for the testing procedure, which may be detrimental in resource limited settings, and could also alter the degradation trajectory by causing the cell to spend more time at a higher voltage.[194] Therefore, in experiments where these measures are not taken, uncertainty in the initial state of lithiation of the cathode could impact estimates of the physical state parameters of interest. To simulate this case, 722 simulations where the five parameters in Table 1 are varied simultaneously with the initial state of lithiation (SoL_0) in the cathode were used. SoL_0 was varied from 0 to 10% in this data set.

The second case of model-experiment disagreement arises from the model itself being an incorrect descriptor of the cathode material's inherent properties. We consider a case where the open circuit voltage curve, a requirement for any physics-based battery model, differs from that of the material being analyzed. To do this, we modified the curve from that used in the physics based model that generated the synthetic training set for the NNs. A 50 mV shift upwards was applied to the original curve in the high-slope region, above 2.9V. The original and modified curve are shown in Figure 6.4.

In both of the above case studies, the simulated voltage curves were passed into the pre-trained ML models, and the predictions of the physical parameters were compared to the true values. We

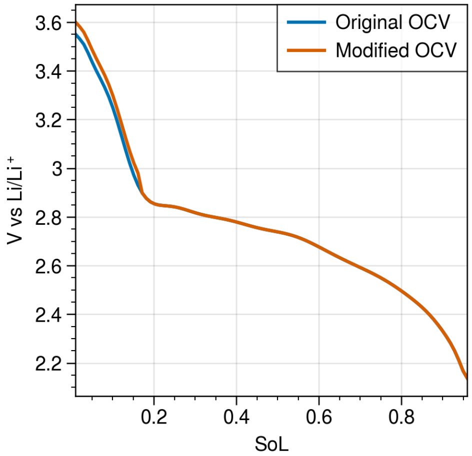

Figure 6.4: Original OCV-SoL (state of lithiation) curve used to generate the training set for the inverse ML models in this study, and the modified curve used to evaluate the ML models' performance in the face of an inherent discrepancy between the data used to train the ML and the data being evaluated by the ML.

explore the accuracy and precision of the estimates to evaluate the robustness of the maximum likelihood analysis and two ML models towards these two different kinds of discrepancies.

6.3 Results

The accuracies of the three estimation procedures for the five parameters are presented in Figure 6.5, evaluated on an independent test set and presented as mean absolute percent errors (MAPEs). The Maximum Likelihood analysis was performed using the same data that were used to train NN_{base} and NN_{DA}. The comparatively poor accuracy can be attributed to sparse samples in a five dimensional parameter space. The NN_{base} model is able to take better advantage of the training data to return more accurate predictions. The NN_{DA} model leverages the data augmentation procedure to improve on the accuracy of the NN_{base} model. Parameters that are more accurately estimated in the Maximum likelihood analysis are also more accurately estimated by the two NNs. Scatter plots of the predictions plotted against the true values for this test set (Figure 6.13), show that the estimates are not systematically overestimates or underestimates for any of the parameters.

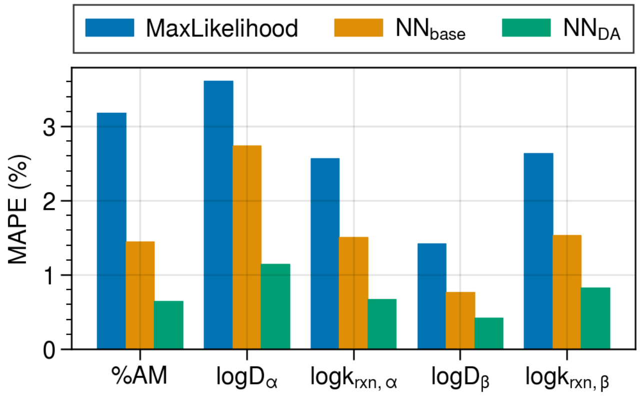

Figure 6.5: Mean absolute percent error (MAPE) for each of the five parameters, designated by color for each estimation approach.

6.3.1 Nonideal Experiments: Initial State of Lithiation

Next, we consider the case of discrepancy between physics based model and experiment where the experiment does not meet the assumptions of the training set used to train the ML offline. The NNs, trained on simulations where the initial state of lithiation (SoL) is always assumed to be 0 at the beginning of a discharge, are evaluated on a data set where SoL is varied from 0 to 10%, along with the five other parameters. The results for all three estimation approaches are shown in Figure 6.6. Scatter plots show the estimates compared to the true values, with a dashed black line that indicates a perfectly accurate estimate. The color of the points on the plots indicate the initial state of lithiation, and can be used to gauge whether inaccuracy can be attributed to a higher initial state of lithiation.

The Maximum Likelihood estimates lose accuracy compared to the base test set in which SOL_0 was maintained at 0 (Table 6.15). The NN_{base} model, which had improved on the accuracy of the Maximum Likelihood estimates in the case of $SOL_0 = 0$ (Figure 6.5), now returns highly biased estimates. As SOL_0 increases from 0 towards 10% (from indigo points to yellow points in Figure 6.6), the parameters are systematically overestimated or underestimated. For $\%AM$ and D_β, the inaccuracies are modest, whereas for the other parameters, a higher initial state of lithiation exacerbates the inaccuracy. These results indicate that the predictions of certain physical states are sensitive to the initial state of lithiation, and failure to include a constant voltage hold at the top of charge in experiments may lead to inaccurate estimates using a neural network trained on physics-based model simulations that do not account for this nonideality.

However, the results in the bottom row of Figure 6.6 indicate that the data augmentation procedure can mitigate these inaccuracies to some degree. Though the same trends of higher SoL_0 leading to more inaccuracy are maintained for all parameters, the degree of the inaccuracy is reduced when data augmentation is applied. The only exception is that when SoL_0 exceeds 6%, D_α is overestimated by up to three orders of magnitude. Based on these results, on average, data augmentation can be seen as a strategy to improve robustness of surrogate inverse neural networks towards nonideal charge.

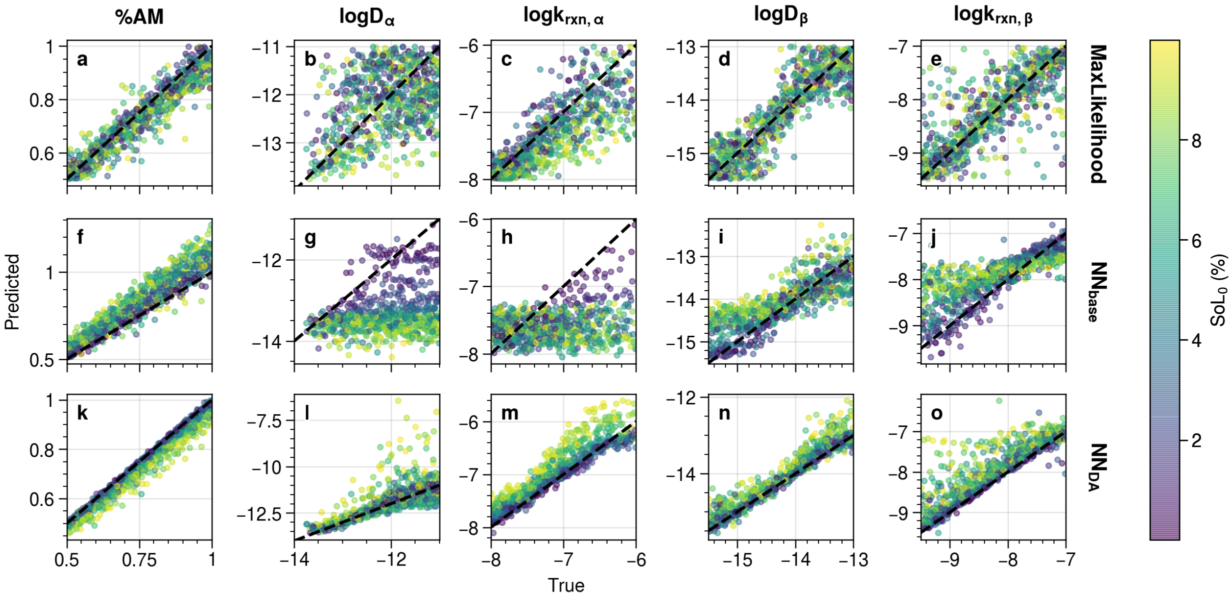

Figure 6.6: Estimates versus true values of parameters (columns) using different estimation approaches (rows), colored by the initial state of lithiation SoL_0 (%). This is quantified by the mean absolute percent errors in Figure 6.15.

6.3.2 Imperfect Physics-based Model: OCV

We next examine the case where the physics based model is an imperfect descriptor of the cathode, described in the last portion of the Methods section. The results of the Maximum Likelihood estimates and the two neural network predictions are shown in the form of residual histograms in Figure 6.7. The residual (difference between estimate and truth) is calculated for each sample in the test set. Visualization of the residual distribution clarifies both the accuracy (how close the peak of the distribution is to 0, dashed vertical line) as well as the precision, i.e. the width of the distribution. Scatter plots of the predictions as a function of the true values, which contain more detailed information like the dependency of accuracy on the true value, are provided in Figure 6.14.

We again find that the Maximum Likelihood estimates are less accurate than the case where the model is a perfect descriptor of the experiments (Table 6.15), which is of course expected. However, there does not appear to be any bias to the estimates, unlike the predictions from the NN_{base} model, which are clearly biased. The $\%AM$ is underestimated, and all other parameters are overestimated, as evidenced by predictions falling to the right of the dashed line indicating a perfect estimate. However, moving to the neural network trained on the simulations with data augmentation, these biases are rectified to some extent. The residuals move closer to zero and are also less spread out, meaning that the estimates are both more accurate and more precise.

This cast study indicates the danger in using neural networks for parameter estimation with an imperfect physics-based model. If the physics-based model does not adequately describe the experiments, predictions from an inverse surrogate ML model trained on this physics-based model could lead to highly inaccurate results. Strategies like data augmentation may be required to mitigate this kind of bias.

Figure 6.8 summarizes the results presented above, comparing performance of each of the estimators for the base test set and for the cases of nonideal experiment and imperfect model. Results are shown for three of the five parameters that describe the thermodynamics, transport, and kinetics in LVO particles. For each of the estimators, model-experiment discrepancy leads to a larger inaccuracy in the estimate. Comparing the NN_{DA} to the NN_{base}, it is clear that in both cases of model-experiment discrepancy, data augmentation limits the loss in accuracy relative to the base case.

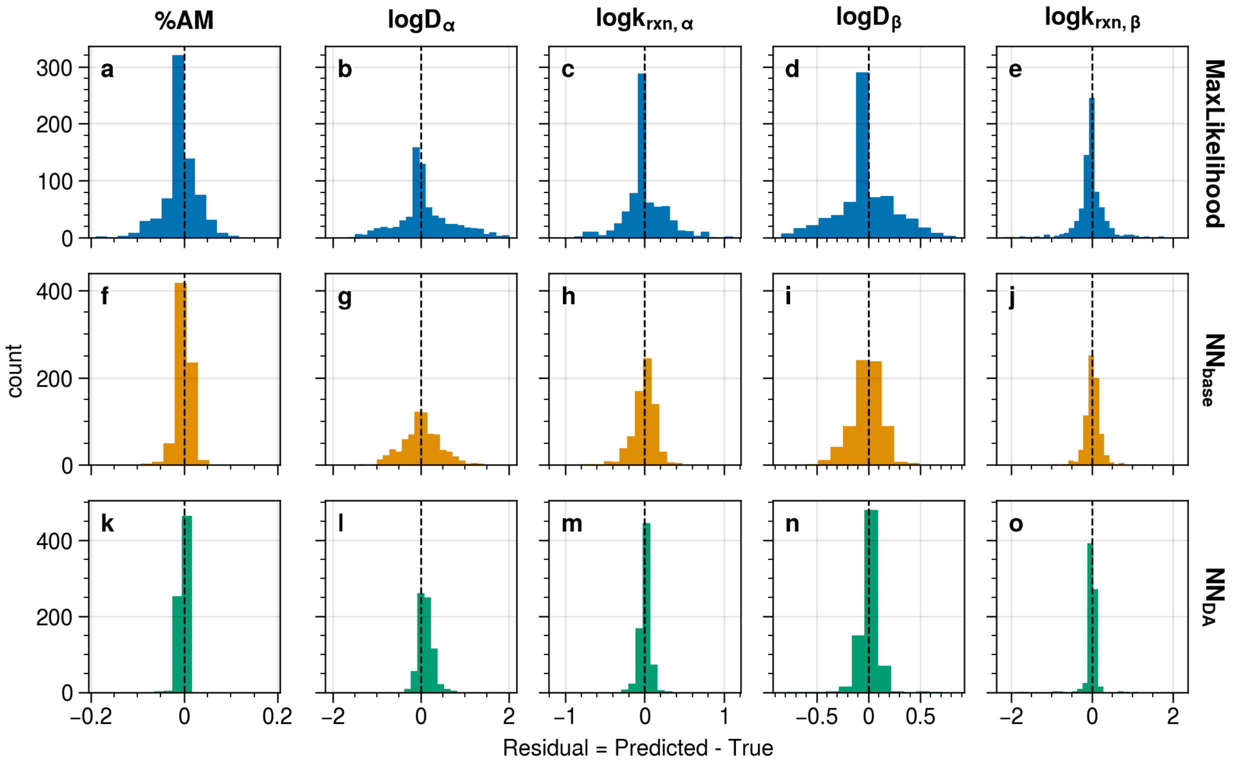

Figure 6.7: Histograms of the residuals of the predictions using different estimation approaches (rows) for the data set using the modified (orange) OCV curve from Figure 6.4, where NN_{base} and NN_{DA} were trained on a data set using the original (blue) curve from Figure 6.4.

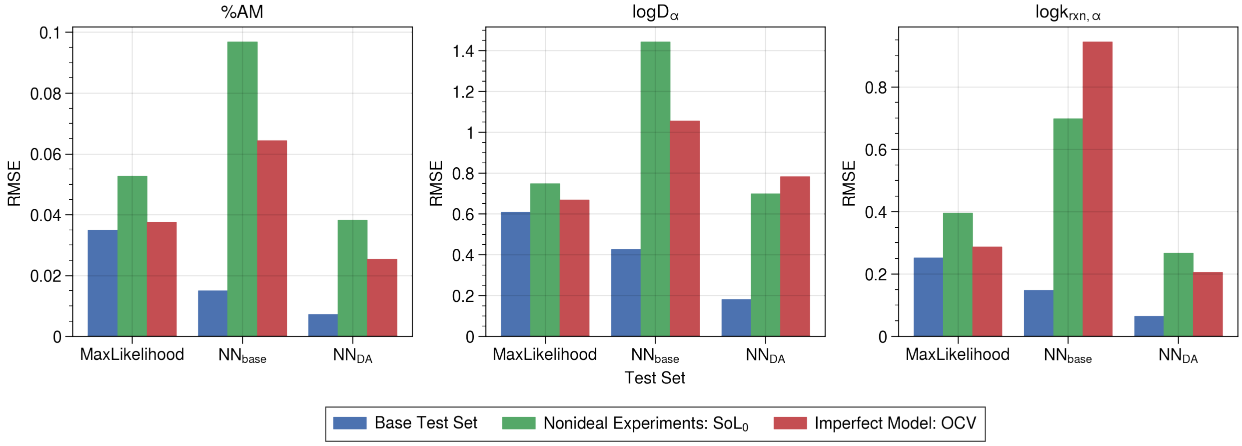

Figure 6.8: Root mean squared errors (RMSEs) for three of the five parameters of interest, grouped by the estimator and colored by the evaluation set.

6.3.3 Evaluation on Experiments

Given the above analysis that compares the robustness of the maximum likelihood estimation to that of the two neural networks, we take each of these estimators and apply them to experimental cycling data, published previously.[165] The results are shown in Figure 6.9. Estimates are provided as points for each cycle, with a line representing the five cycle rolling average passing through the points. The reader is referred to Ref.[165] for more discussion on the physical meaning of the evolution of these parameters.

Maximum Likelihood estimates are qualitatively consistent with the results that were fit to voltage as opposed to time in our previous work.[165] Discontinuous predictions from the Maximum Likelihood analysis are present because the estimate accuracy is limited by the sparsity of the data set used to perform the maximum likelihood analysis. As mentioned earlier, if a larger number of parameter combinations in the five parameter space were simulated (as was done in Ref.[165]), the maximum likelihood estimates would be more accurate and the estimates on the experimental data would thus be more continuous.

Based on the conclusion that the NN_{DA} model is the most robust, we put the most faith in these estimates. For D_α, $k_{rxn,\alpha}$, and D_β, we see that the NN_{base} model, while predicting similar trends in evolution of the parameter to the NN_{DA} model, returns values that are orders of magnitude above the NN_{DA} estimates and are outside of the expected parameter range based on the training data (Table 7.1). These results indicate that the NN_{DA} model is able to interpolate between the training data effectively, without succumbing to the significant bias that the NN_{base} model suffers from in the face of discrepancies between the physics-based model and experiment.

6.4 Conclusions

A detailed procedure for implementing robust neural networks to estimate parameters from discharge curves is presented. Neural networks show strong interpolative ability in a five dimensional parameter space when trained on fewer than 1000 simulations, returning more accurate estimates

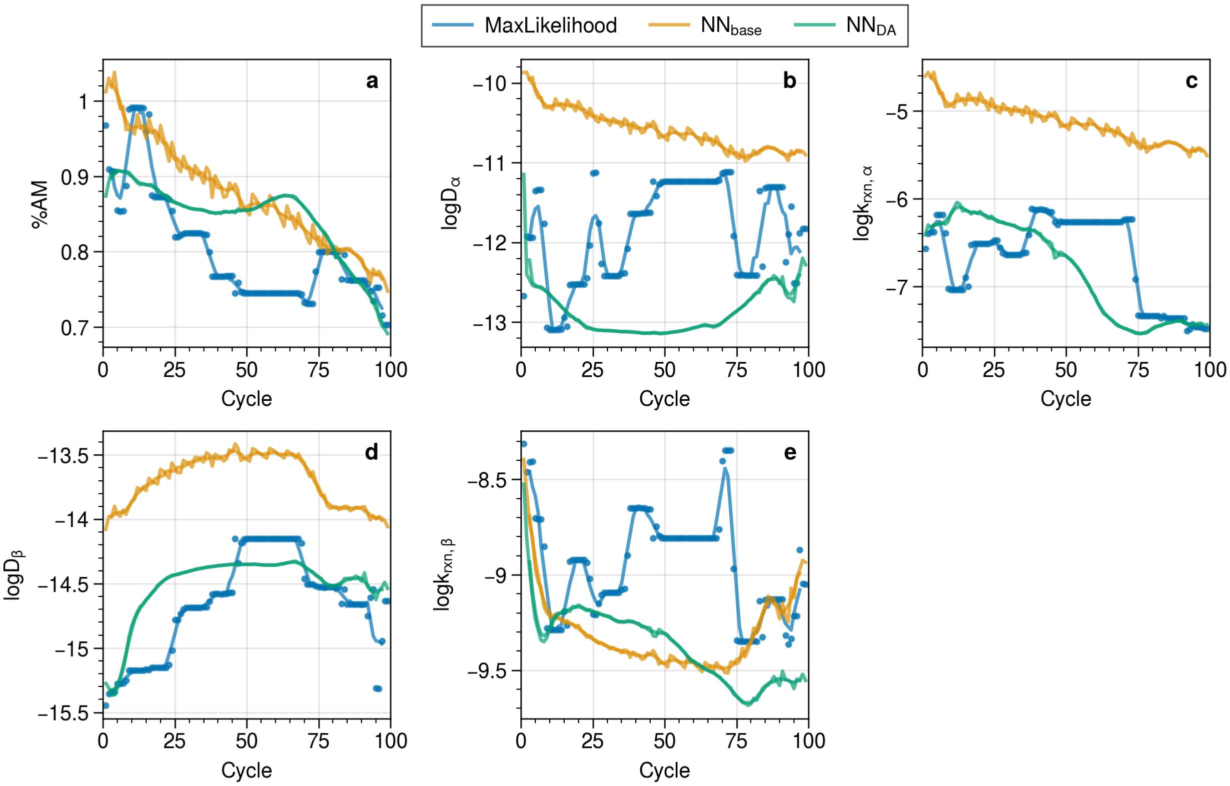

Figure 6.9: Predicted values of five parameters in Table 7.1 for experimental data published in Reference[165] using different estimation approaches. Estimates are shown as points, and the line passing through the points represents a five cycle rolling average.

than a maximum likelihood analysis using the same number of simulations. Neural networks trained on the same set of simulations but augmented with random shifts that increase the number of curves for training to eight times the original amount show even better performance. Data augmented neural networks are more robust when trained on an imperfect physics-based model or when estimating parameters for nonideal experiments. The application of a neural network without data augmentation can lead to highly biased, inaccurate parameter estimates.

Though presented in the context of tracking degradation, this approach is relevant to parameter optimization of physics-based models more generally. The choice of optimization approach will depend on the complexity of the physics-based model, the number of parameters to optimize, and the data being fit.[189] If one chooses the inverse ML surrogate model approach, the implementation details and discussion on robustness presented in this paper are all relevant. The two case studies testing the robustness of neural networks are specific examples of possible model-experiment discrepancy relevant to the use case of physics-based models to track degradation.

6.5 Supporting Information

6.5.1 Maximum Likelihood Estimation

The maximum likelihood estimate are derived from Bayes Theorem. Consider a vector of k parameters X.

$$X = [p_1, p_2, ...p_k]$$

Given a set of observations, in this case a set of features $\{tC_r^{exp}\}$ representing a discharge profile (see Methods in main text for a detailed description of converting a voltage curve to tC_r features), the posterior distribution for the parameters in X that best describe the data can be written as follows.

$$prob(X|\{tC_r^{exp}\}) = \frac{prob(\{tC_r^{exp}\}|X)prob(X)}{prob(\{tC_r^{exp}\})}$$

The first term in the numerator is the likelihood of observing the voltage curve represented by $\{tC_r^{exp}\}$ given the parameters X. The second term in the numerator contains prior knowledge of the parameters X. In this study, we use uniform priors for the five parameters, listed in Table 7.1. The denominator is referred to as the evidence, and can be taken as a scaling factor independent of the parameters X. Therefore, the posterior distribution is proportional to the likelihood function.

$$prob(X|\{tC_r^{exp}\}) \sim prob(\{tC_r^{exp}\}|X)$$

If the voltage curve is discretized into N features (see Methods), the right hand side can be expanded as

$$prob(X|\{tC_r\}) \sim \prod_{j}^{N} \frac{1}{\sigma_{exp}\sqrt{2\pi}} exp\left(\frac{(tC_{r,j}^{sim}(X) - tC_{r,j}^{exp})^2}{-2\sigma_{exp}^2}\right)$$

which can be simplified to

$$prob(X|\{tC_r\}) \sim \left(\frac{1}{\sigma_{exp}\sqrt{2\pi}}\right)^N exp\left(\frac{\sum_j^N (tC_{r,j}^{sim}(X) - tC_{r,j}^{exp})^2}{-2\sigma_{exp}^2}\right)$$

The feature values simulated by the physics based model for a set of parameters X are indicated by superscript sim. The term multiplying the exponential is a constant. The summation in the numerator of th exponential is the residual sum of squares, or RSS, describing the goodness of fit of a simulation with the experimental data. Written simply, the posterior distribution is related to the RSS by

$$prob(X|\{tC_r\}) \sim exp\left(\frac{RSS}{-2\sigma_{exp}^2}\right)$$

The experimental uncertainty σ_{exp} is assumed to be 0.02, or a two percent state of lithiation. This assumption does not impact the mean predicted estimates. After performing M simulations for a set of M Sobol points in the parameter space of X (see Methods), the relative probabilities of each set of parameters is given by the above equation, and can be used to calculate the maximum likelihood estimate μ_p for a parameter p, given below.

$$\mu_p = \frac{\sum_i^M p_i exp\left(\frac{RSS_i}{-2\sigma_{exp}^2}\right)}{\sum_i^M exp\left(\frac{RSS_i}{-2\sigma_{exp}^2}\right)}$$

6.5.2 *Feature Resolution*

Voltage versus time discharge curves are converted to a vector of features. The time values at a set of voltages spanning the upper and lower cutoff voltage (3.6V and 2.0V for LVO) are scaled by the C-rate (C_r) to create a set of tC_r values. The voltages at which these features are taken is determined by the feature resolution. For example, a 10 mV resolution results in 160 tC_r features to represent a curve. The figures presented below analyze the effect of feature resolution on Maximum Likelihood estimates as well as estimates from a neural network.

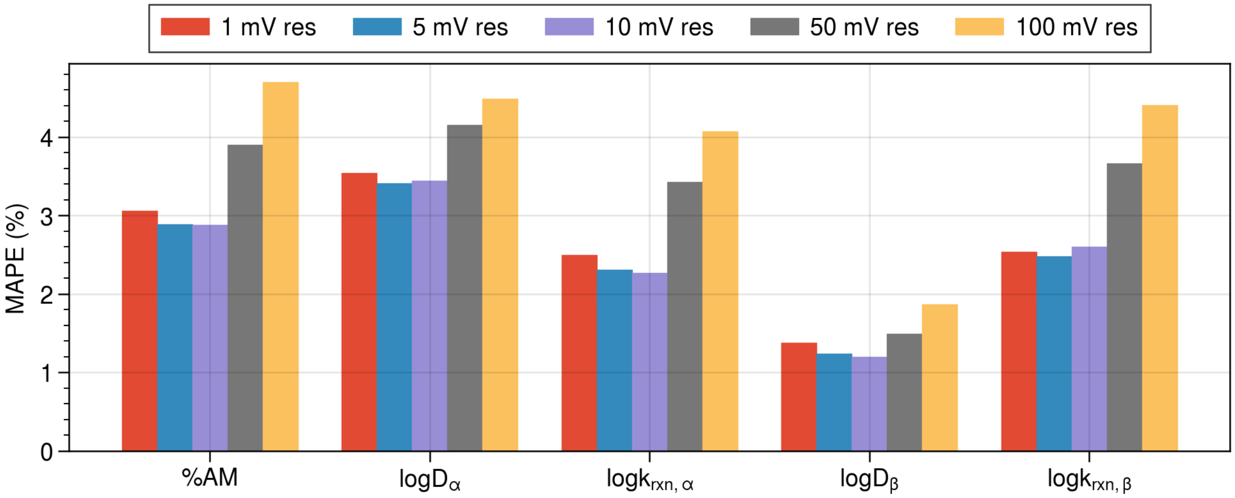

Figure 6.10: Accuracies of the Maximum Likelihood estimates, given as mean absolute percent errors (MAPEs), for voltage curves featurized at different resolutions. There appears to be a drop in accuracy above 50 mV resolution.

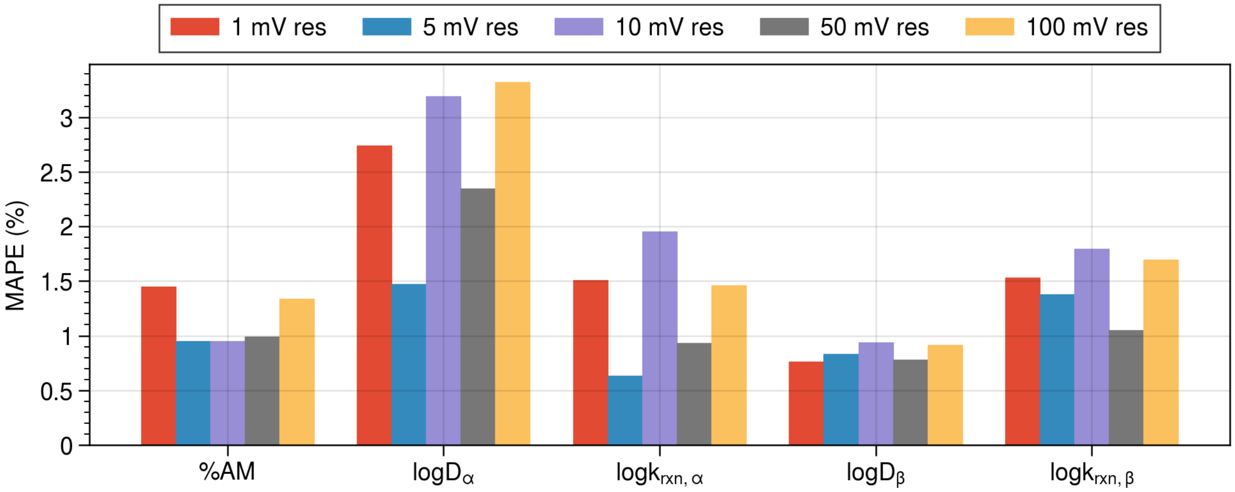

Figure 6.11: Accuracies of the NN_{base} model estimates, given as mean absolute percent errors (MAPEs), for voltage curves featurized at different resolutions. The accuracy does not appear to follow any trend with resolution.

6.5.3 Data Augmentation

This section is provided to demonstrate the impact of increasing degrees of data augmentation on prediction accuracy. The data augmentation procedure is outlined in the Methods section in the main text.

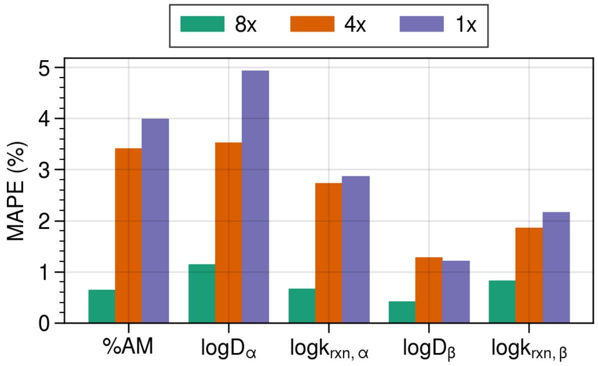

Figure 6.12: Accuracies of NN_{DA} models trained on different amounts of augmented training data, given as mean absolute percent errors (MAPEs). 1x refers to a single set of random shifts added to the original training set, whereas 8x refers to 8 different sets of random shifts added to the same original training set to create 8 different data sets that can be combined into one large training set.

6.5.4 *Estimation Accuracy*

In this section, we provide scatter plots of predictions versus truth for the Maximum likelihood estimates accuracies in Figure 6.5 and for the residual histograms in Figure 6.7. In addition to these, mean absolute percent errors (MAPEs) for all three estimators applied to the three evaluation sets (base test set, case of imperfect experiments, and case of imperfect model) are provided.

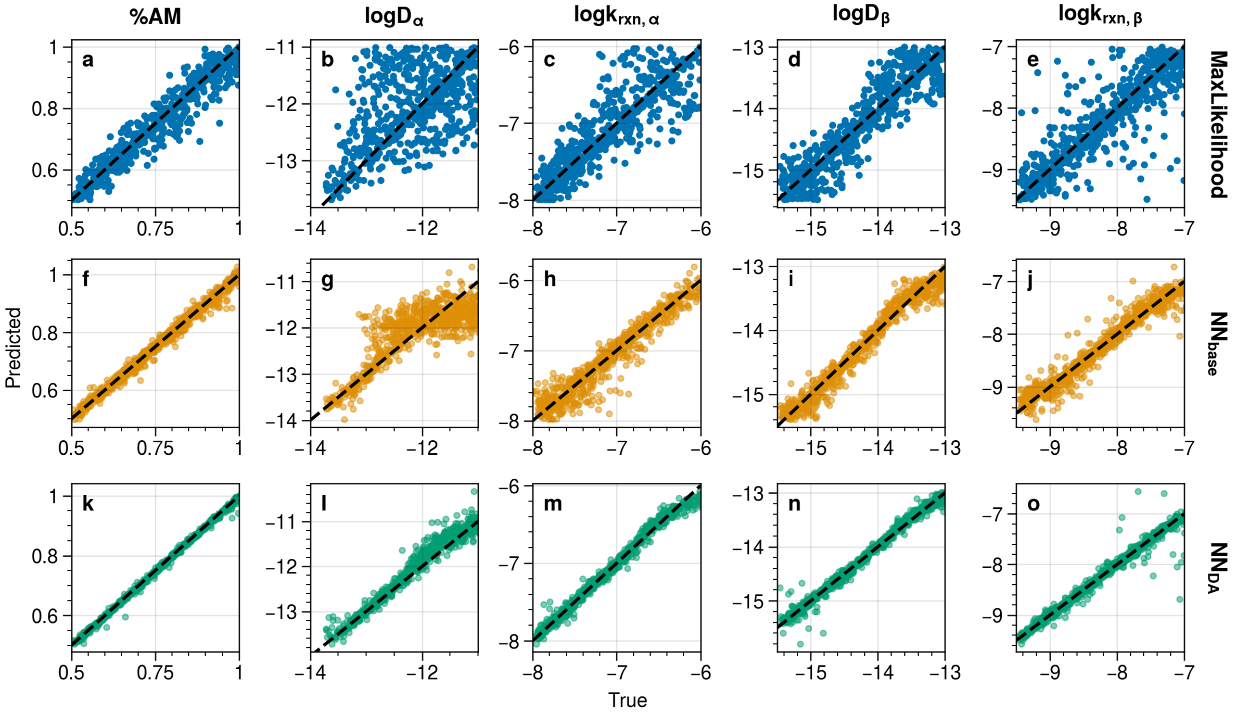

Figure 6.13: Predicted versus true values of parameters (columns) using different estimation approaches (rows) for the base test set that contained no model-experiment discrepancies were introduced.

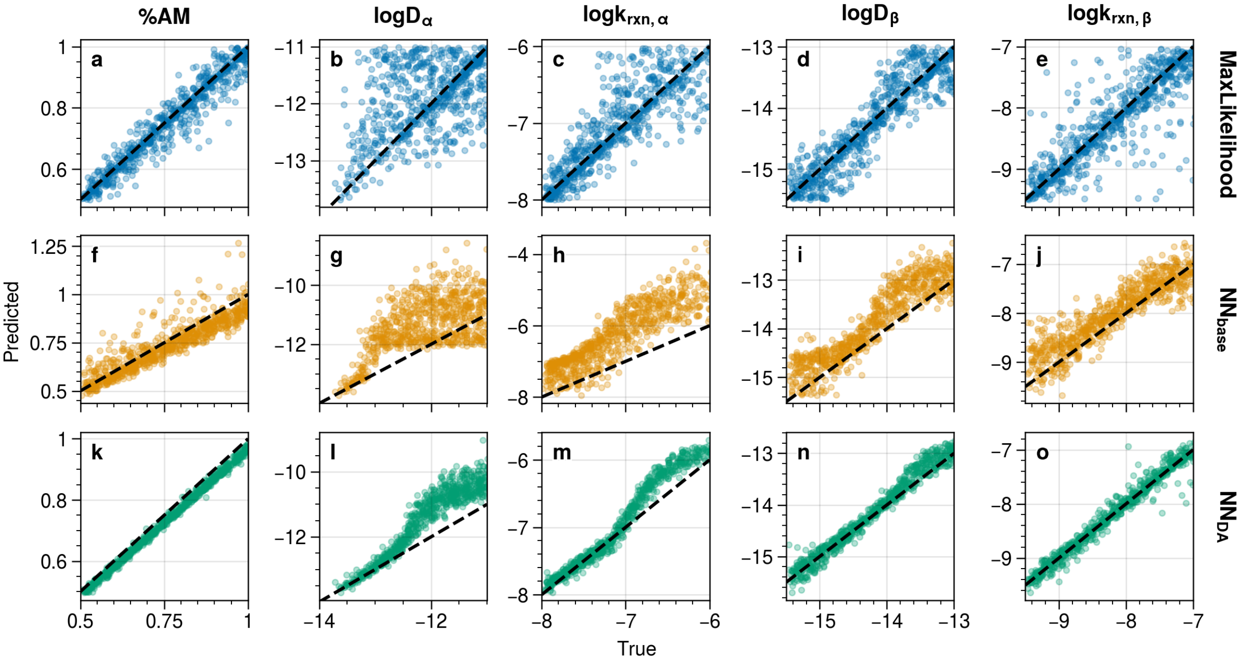

Figure 6.14: Predicted versus true values of parameters (columns) using different estimation approaches (rows) for the data set using the modified (orange) OCV curve from Figure 6.4, where NN_{base} and NN_{DA} were trained on a data set using the original (blue) curve from Figure 6.4.

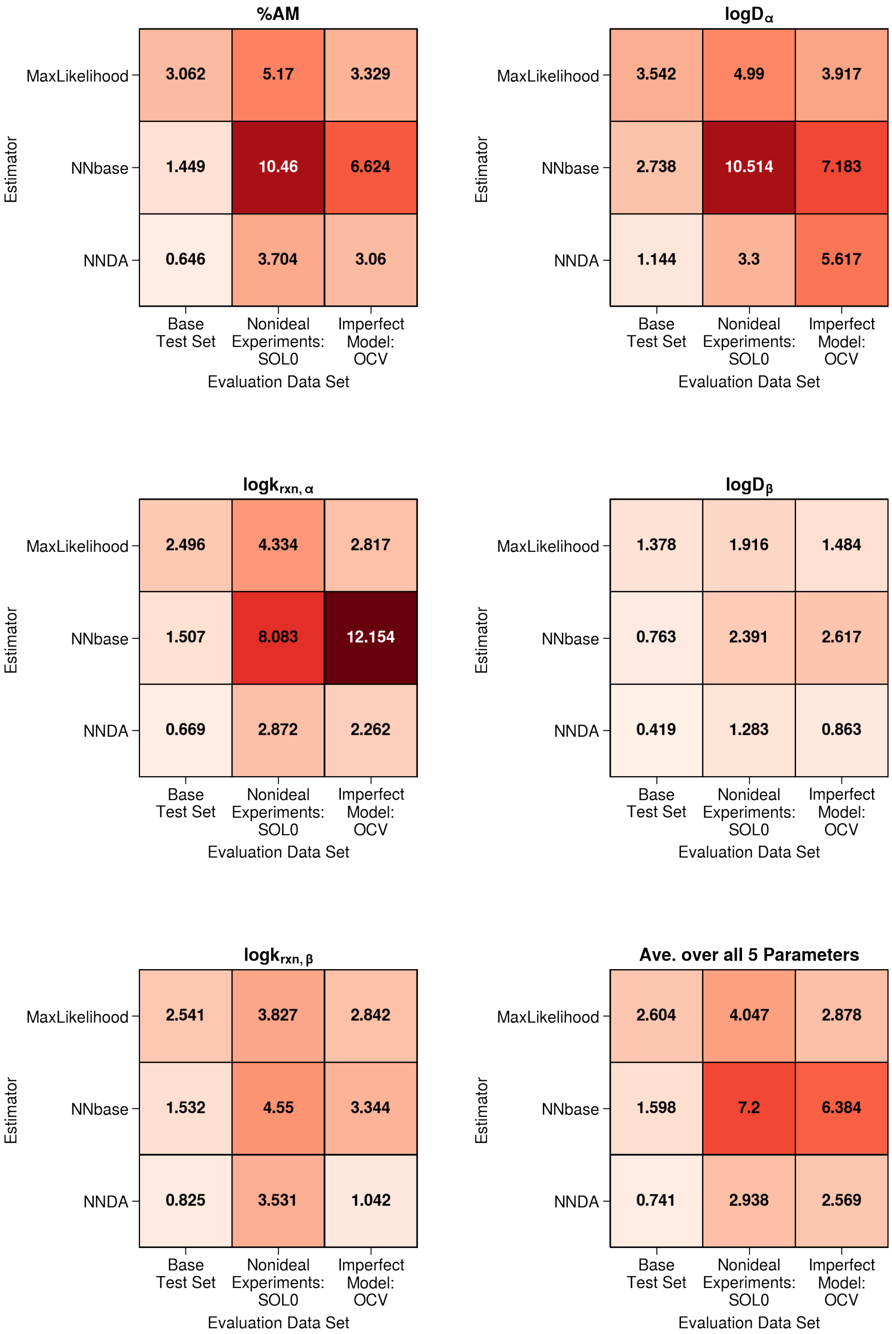

Figure 6.15: Table of mean absolute percent errors (MAPEs, units of %) for each parameter (a-e), with rows containing results for the three estimators applied to three different evaluation sets (columns).

Chapter 7

Physics-based Models, Machine Learning, and Experiment: Towards Understanding Complex Electrode Degradation*

---

[*] This Chapter is in preparation to be submitted for publication: Karthik. S. Mayilvahanan, Andrew Nicoll, Jwal. R. Soni, Kenneth. J. Takeuchi, Esther. S. Takeuchi, Amy. C. Marschilok, and Alan. C. West, "Physics-based Models, Machine Learning, and Experiment: Towards Understanding Complex Electrode Degradation."
The thesis writer's contribution was ideation, implementation of ML models, analysis and writing. The electrochemical observations and characterization were provided by Andrew Nicoll from the Marschilok-Takeuchi Research Group at Stony Brook University.

7.1 Introduction

Understanding degradation for a battery chemistry can be essential in both the cell and materials design process as well as diagnosis and prognosis over the course of the battery's use. Current approaches to develop mechanistic understanding span a range of length and time scales, including everything from highly accessible materials and electrochemical characterization to more powerful but less accessible synchotron characterization.

Model-based approaches to understanding degradation offer a rapid alternative to experiment for diagnosis and mechanistic hypothesis testing. Many have used physics-based models to simulate cycling and consequent degradation behavior, such as parasitic reactions, surface layer growth, Li plating, or particle cracking.[44–49,139,195,196] This approach can be powerful in exploring how different degradation mechanisms depend on conditions and usage, and in predicting future performance. However, this approach of explicitly defining degradation mechanisms and simulating long-term usage can be difficult because there are multiple possible ways of coupling mechanisms, and models for these mechanisms often include rate constants or fitting parameters that must be calibrated to experiments.[48,49] More work is required to parameterize models for degradation mechanisms and select between competing models for the same phenomena.

Models can also be useful in the context of diagnosis, i.e. estimating the state of the system. In real-time applications, this is often referred to as state of health estimation, and involves estimating the available capacity of a cell and its internal resistance. The models best suited for these applications tend to be reduced order representations of cells, such as equivalent circuit models or even data driven state estimators.[184] When speed, resource efficiency, and accuracy are less of a priority than mechanistic understanding, models that are more detailed in their description of cell and particle level physics may be of interest. Physics-based, continuum level electrochemical models can be used to describe the state of a cell over the course of cycling by refitting model parameters to data over the lifetime of the cell. Tracking the changes in model parameters describing transport in the active material and electrolyte domains as well as those describing the kinetics of charge transfer can provide insight into the evolution of different kinds of internal impedances in the cell.[132,133,165,197] Similarly, tracking evolution of the amount of active material in each electrode, or the lithium inventory in the cell is essential to quantify sources of capacity loss.[131,133,197]

In this paper, we apply the parameter estimation approach to lithium trivandate (LVO) cathodes cycling at different current rates. Electrodes are cycled under currents much higher than typically reported in the literature, activating degradation mechanisms that lead to different observed degradation trajectories. We track parameter evolution over the course of cycling at these different rates using an ML model trained offline on synthetic data (i.e., data derived from validated physics-based models that have been reformulated to account for model parameter changes representative of degradation), and provide commentary on how to enhance the analysis of capacity fade curves with this procedure. Through analysis of exemplary cells and their parameter estimates, we show how insights from this type of analysis can be used to narrow the scope of possible mechanisms. We proceed to provide parameter estimates for a larger data set of LVO cells, and conclude with thoughts on the value of this approach in the context of degradation analysis.

7.2 Methods

7.2.1 Experimental

LVO electrodes were prepared according to procedure outlined in Reference[129]. The electrodes are composed $Li_{1.1}V_3O_8$ and carbon nanotubes (CNTs) in a weight ratio of 7:3, and are punched into 0.5 inch diameter electrodes. Cells were assembled with Li metal anodes, polypropylene separators, and 1M $LiPF_6$ in ethylene carbonate/ dimethyl carbonate (volume ratio of 3:7) electrolyte. It has been verified via modeling that these electrodes contain sufficient porosity that electrode-scale concentration gradients under the experimental conditions considered are not important.[129]

Cells were cycled under constant current, at C-rates between 0.2C and 2C (1C = 362 mAh/g) and between 3.75V and 2.0V at a fixed temperature of 30degC. Some cells underwent a "revival" procedure, where the cycled cell was disassembled and the cathode was reassembled into a new cell with a fresh Li metal anode, separator, and electrolyte.

7.2.2 Physics-Based Model and Parameter Estimation

The model being fit to experiments is outlined in Reference[32]. The model describes simultaneous phase change and lithiation of the layered α-phase and rock-salt type β-phase on the particle scale. This model, like most physics-based electrochemical models, has several parameters that could evolve, and some domain knowledge was used to reduce the parameter space. McCarthy et. al. showed via location-dependent energy dispersive x-ray diffraction (EDXRD) experiments before and after cycling that degradation is not a heterogeneous effect along the length of the electrode.[129] Based on this result, model parameters describing physics on the particle scale were estimated. These parameters include those describing intercalation kinetics in each phase, Li transport within each phase, and the amount of ionically and electronically connected active material in the cathode.

It is important to note that the parameters being estimated are representations of multiple physical processes. For instance, evolution of an estimated diffusion coefficient does not necessarily mean that the true diffusivity is changing. Rather, it is an indication that the time scale for the diffusion process is changing. This nuance is important because the diffusivity cannot be decoupled from the length scale for diffusion. Therefore, a change in an effective length scale for diffusion could explain a change in the estimated diffusivity.[189,198] Similarly, changes in kinetic parameters result in state of charge independent shifts of the voltage curve in the model. Therefore, decreases in these parameters are proxies for increases in electronic resistances in the cell. The kinetic parameters such as exchange current density cannot be decoupled from surface area, so increases in surface area will appear as increases in the kinetic parameter.

The parameter estimation procedure follows the development outlined in Reference[199], with some slight modifications. The general framework is to generate a training set of pairs of parameters, pass these parameters through a validated physics-based model to generate the corresponding electrochemical data, and train a machine learning model to map the electrochemical data to the parameters.[154,159,187,188,190,199]

Samples were taken using Sobol sampling in a seven parameter space, including the five parameters described above, C-rate, and initial state of lithiation. The bounds for the parameters are provided in Table 7.1. The initial state of lithiation at the start of a discharge half-cycle could be nonzero if the previous charge did not remove all the Li in the particle, and was included to introduce some physically motivated noise into the training set. These samples were passed through the physics-based model to create discharge curves for training.

A feed forward neural network (NN) was trained to take a discharge curve and the operating C-rate as an input and regress a vector of five parameters that correspond to that discharge curve. The data augmentation procedure outlined in Reference[199] was employed prior to training, leading to an 8x increase in training set size. During the training, samples in the training set that have C-rates closer to C-rates used in experiment are weighted more when computing the loss. Uncertainties in the parameter estimates are calculated using Monte Carlo dropout. Full details of the data generation, featurization, data augmentation, network specifications, training procedure, uncertainty quantification, and model accuracy are outlined in the Supplementary section 7.5.2.

The RMSEs are provided in Table 7.1. The reported RMSEs of the transport and kinetic parameters in the β-phase are higher than their α-phase counterparts. This is because, at higher C-rates, little to no phase transformation occurs, so the discharge curves are relatively insensitive to the β-phase parameters. This is made clear in Supplementary Figure 7.9, where the predictions are colored by C-rate. The larger RMSEs of the β-phase parameters is driven by errors at higher rates. Also of note is that the reported uncertainties reflect the physical sensitivity of the system to the model parameters. At higher C-rates, α-phase parameters can be determined with greater certainty because the model is more sensitive to transport and kinetics at higher rate. The β-phase parameters go through a minima due to competition between this effect and the phenomena where less β-phase is formed at higher rates.

Table 7.1: Model parameters and test set estimation accuracies.

Model Parameter	**Symbol**	**Range**	**Units**	**RMSE**
% of nominal amount of active LVO	%AM	[0.5,1.0]	%	0.023
Li diffusivity in α phase	$log_{10}D_{\alpha}$	[-14.0,-11.0]	$cm^2 s^{-1}$	0.131
Li insertion rate constant in α phase	$log_{10}k_{rxn,\alpha}$	[-8.0,-6.0]	$cm^{-5/2}mol^{-1/2}s^{-1}$	0.057
Li diffusivity in β phase	$log_{10}D_{\beta}$	[-15.5, -13.0]	$cm^2 s^{-1}$	0.380
Li insertion rate constant in β phase	$log_{10}k_{rxn,\beta}$	[-9.5, -7.0]	$cm^{-5/2}mol^{-1/2}s^{-1}$	0.371
C-rate	C_r	[0.2, 2]	h^{-1}	-
Initial state of lithiation	SoL_0	[0, 0.25]	-	-

7.3 Results and Discussion

7.3.1 Degradation hypotheses for LVO

As with most chemistries, degradation of LVO is highly dependent on choices made through each step from materials synthesis to cell assembly and experimentation. Even when considering cathodes prepared using a sol-gel synthesis, there is a wide range of reported outcomes due to sintering temperature and time, cutoff voltages, C-rates, and carbon and binder content in the electrode, not to mention the expected sample-to-sample variation on the lab scale.[55,58,70,121–125]

A map of hypothesized degradation mechanisms, the stress factors that influence them, and the resulting degradation modes is presented in Figure 7.1,[55,58,70] inspired by a similar framework presented by Birkl et. al. for a Li-ion full cell's thermodynamic behavior.[161] This diagram is helpful in framing how different mechanisms respond to different stress factors, how mechanisms may be coupled, and how these mechanisms present themselves in the parameters we estimate (emphasized in blue). This map is not an exhaustive list of all possible mechanisms, as one could supplement it with more detailed hypotheses. It is a reflection of current hypotheses in the literature as well as our knowledge of the materials system.

Degradation modes in full cells can be bucketed into loss of active material in either electrode, loss of lithium inventory, and resistance increase.[140] The latter describes the kinetic evolution of the cell, while the others describe changes in the thermodynamic quantities. Two key differences are presented due to our cell structure and our framework. First, because we are considering half cells with lithium metal anodes, we need only consider loss of active material in the cathode, and can assume there is enough excess Li in the cell to neglect loss of lithium inventory and loss of anode active material. The loss of active material in the cathode is therefore directly represented by $AM\%$. Second, we make a delineation in the cell resistance increase between resistance increase associated with ions and resistance increase associated with electrons. These two phenomena correspond to D and k_{rxn}, and have different implications based on the time and length scales being considered. Knowledge of which of these phenomena is responsible for cell impedance increase could be valuable from both a battery management and material design perspective.

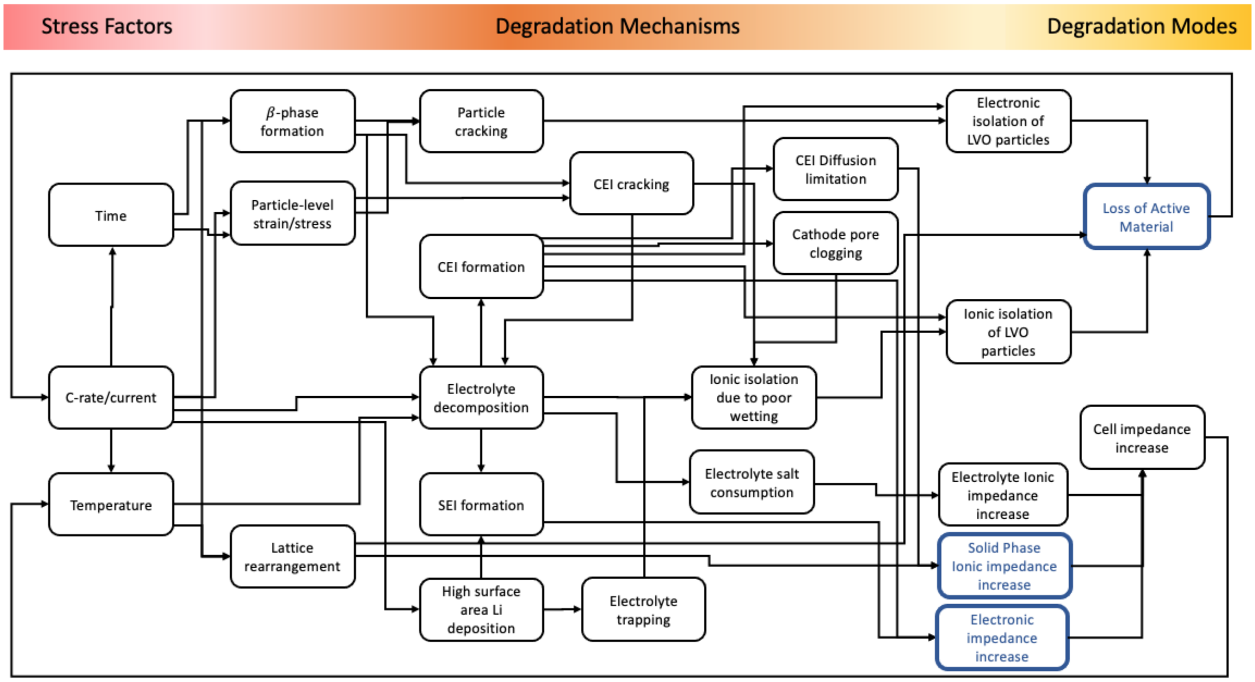

Figure 7.1: Map of stress factors, hypothesized degradation mechanisms, and degradation modes for the LVO system, similar to the framework presented by Birkl et. al.[161] The parameters that are estimated over the course of cycling correspond to the boxes highlighted in blue. Solid lines indicate expected connections, whereas dashed lines represent possible connections.

7.3.2 *Parameter Estimation Results*

Before looking at the entire data set and commenting on degradation mechanisms across multiple C-rates, we will walk through the parameter estimation results and their interpretation for two exemplary cells.

Figure 7.2 shows the experimentally observed capacity fade and corresponding parameter estimates for a cell cycled at 0.5C. The capacity is reported as specific discharge capacity normalized by specific theoretical capacity in subplot a, and parameter estimates are reported in subplots b-f. After 100 cycles, the cathode undergoes revival where it is placed in a new cell with fresh Li metal anode and electrolyte, as described in the Methods section.

In the first 100 cycles, we observe loss of active material up to 50% and impedance increase for Li diffusion and for electrons, as evidenced by degradation of the α-phase parameters. There appears to be a "breaking in" effect in the first five cycles, as the α-phase parameters go through a maximum. Since these cells did not undergo a formation process, this evolution could be associated with formation of surface layers on either electrode, or some reduction in particle size that slows.

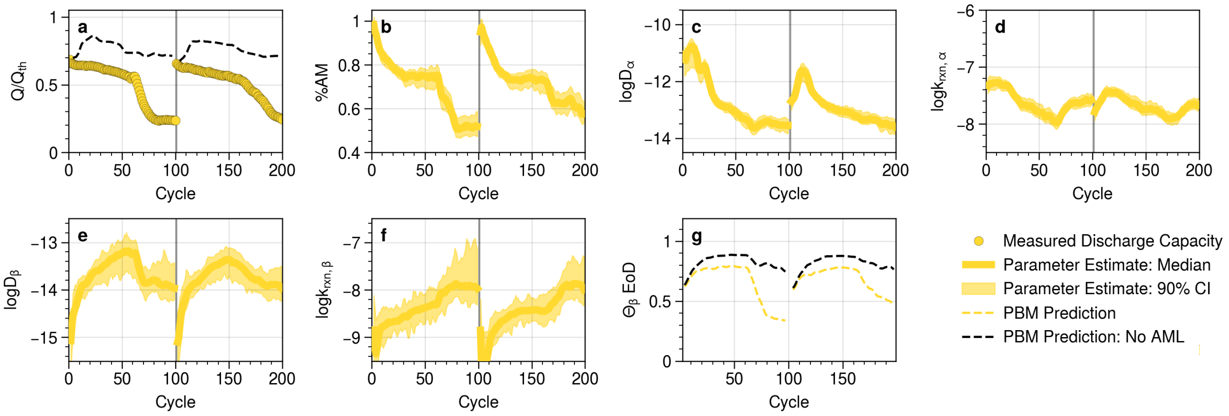

Figure 7.2: (a) Capacity fade of an LVO cell cycled at 0.5C for 100 cycles, followed by a cell revival and cycling for another 100 cycles. Capacity is reported as a specific capacity normalized by the theoretical specific capacity (Q/Q_{th}). (b-f) Parameter estimates based on discharge curve at each cycle, presented as a 3 cycle rolling average. Shaded regions show 90% confidence interval in the estimate. (g) Based on the parameter estimates in (b-f), the model-predicted volume fraction of the β-phase at end of discharge (Θ_β EoD) is presented. Dashed black lines indicate model-predictions for discharge capacity (a) and Θ_β EoD (g) if all LVO particles are ionically and electronically accessible (i.e. no active material loss).

The dotted line in Figure 7.2a shows the expected capacity fade when assuming there is no loss in active material, which can be determined by passing the parameter estimates back into the physics-based model and turning off active material loss ($\%AM = 1$). An increase in capacity is predicted in the first 20 cycles before decreasing. This can be explained by the competing effects between accumulation of α-phase impedances and reduction of β-phase impedances. Diffusion of Li in the β-phase is a key limiting factor in the inability of LVO to achieve its theoretical specific capacity, and an order of magnitude improvement in Li diffusion can unlock inaccessible capacity. After cycle 20, the impedance increase in the α-phase out competes gains from improvement of β-phase transport, resulting in a capacity drop even in the absence of active material loss.

As the cathode is cycled and material becomes inaccessible for lithiation, the same current density is being passed to the cell, so the active particles effectively experience a higher C-rate. By the end of cycling, where there is roughly half the material lost, the active particles are experiencing a current density that is approximately 1C. This effect, combined with the build up of α-phase impedances, results in the lower cutoff voltage being reached sooner, preventing the material from undergoing as much phase change at the end of discharge as was achieved in the earlier cycles (Figure 7.2g).

These parameter estimates serve as an example of why, for the purposes of understanding degradation, it is more meaningful to look at loss of accessible active material as opposed to just the discharge capacity. When just looking at the discharge capacity, there is only an 8% loss over the first 20 cycles. However, there is a 20% loss in active material in these 20 cycles. This difference is explained by more capacity becoming accessible as β-phase transport improves in these first 20 cycles.

The amount of "bounce back" in $\%AM$ when the cell undergoes revival is an important metric in understanding the cause of active material loss. In this cell the $\%AM$ returns to 100% after revival (Figure 7.2b). This indicates that the estimated active material loss in the first 100 cycles can be further specified as active material loss due to ionic isolation of LVO particles from poor electrolyte wetting. If the $\%AM$ had not returned to 100%, the active material loss would be attributed to electronic isolation of particles, or ionic isolation not due to wetting (e.g. an ionically blocking CEI). Poor wetting could be traced back to parasitic reactions that consume the electrolyte.

On revival, the estimated D_α does not recover to its initial value, indicating that some irreversible change to diffusion of Li in the particles occurred in the first 100 cycles. The immediate increase in D_α on revival could be explained by shorter length scales for diffusion if LVO particles are fully wetted by electrolyte as opposed to partially wetted. The fact that both D_α and $k_{rxn,\alpha}$ appear to have the same "breaking in" on revival and then degrade further indicate that they may represent a superposition of cathode side effects and some anode/electrolyte interphase formation.

Based on the analysis of the capacity fade curves and parameter estimates in the first 100 cycles and after revival, some mechanisms delineated in Figure 7.1 can be eliminated. A reduced version of this diagram is shown in Figure 7.3. The stress factors are removed from the diagram because we are interpreting results from only one cell uner one set of conditions. Based on the observations of fully recoverable material loss on cell revival, all pathways leading to active material loss that do not pass through ionic isolation due to poor wetting can be eliminated. We observe some degree of solid phase ionic impedance increase and electronic impedance increase that cannot be recovered on revival, indicating some irreversible evolution of the cathode. The root cause of these impedance growths cannot be specified without further experimentation. Still, the space of possible degradation mechanisms is greatly reduced and can guide further resources towards distinguishing between the remaining possible pathways.

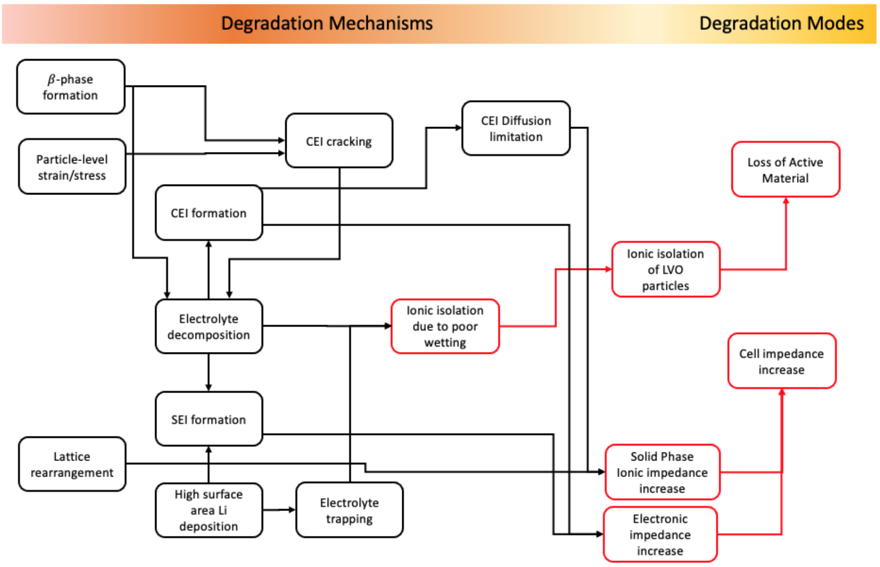

Figure 7.3: A map of possible degradation mechanisms, eliminating some and placing more confidence in others, based on the original space of hypothesized mechanisms in Figure 7.1 and interpretation of parameter estimates in Figure 7.2.

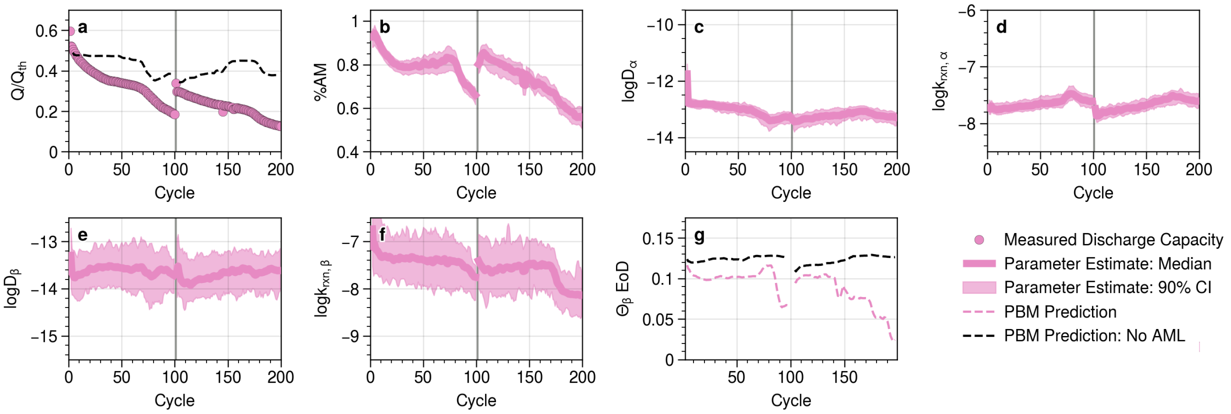

Figure 7.4: (a) Capacity fade of an LVO cell cycled at 2C for 100 cycles, followed by a cell revival and cycling for another 100 cycles. Capacity is reported as a specific capacity normalized by the theoretical specific capacity (Q/Q_{th}). (b-f) Parameter estimates based on discharge curve at each cycle, presented as a 3 cycle rolling average. Shaded regions show 90% confidence interval in the estimate. (g) Based on the parameter estimates in (b-f), the model-predicted volume fraction of the β-phase at end of discharge (Θ_β EoD) is presented. Dashed black lines indicate model-predictions for discharge capacity (a) and Θ_β EoD (g) if all LVO particles are ionically and electronically accessible (i.e. no active material loss).

Figure 7.4 shows a similar analysis for an exemplary cell cycled at 2C. After 100 cycles, roughly 35% of the particles have lost ionic and/or electronic contact, since $\%AM$ is estimated to be 65%. After a large estimated drop in the first cycle, D_α appears to remain the same until about cycle 60, where it starts to decrease. D_α remains the same as its estimated cycle 100 value after revival, indicating that on the particle level something has changed that is slowing the diffusion process. $k_{rxn,\alpha}$ appears to slightly increase with cycling, resets after revival, and increases again. This effect could be attributed to electrolyte and/or anode effects. The β-phase parameters are estimated to be constant with large uncertainties, consistent with the expectation that little β-phase is formed at 2C (Figure 7.4g).

The predicted degradation in the absence of material loss follows the trajectory of decreasing D_α (dashed line, Figure 7.4a), and predicts that 40% of the theoretical capacity would be delivered if all the particles were connected. However, on revival, we see that the $\%AM$ does not return to 100%, as was observed in the 0.5C cell in Figure 7.2b. This means that not all of the active material loss can be explained by poor wetting that would be resolved when the cell was revived.

Since the $\%AM$ returns to 80% on revival, of the estimated 35% active material loss after 100 cycles, 15% can be explained by the wetting effect. In this case, one must consider electronic isolation of particles or ionic isolation not due to electrolyte contact with particles.

The reduced degradation diagram for this cell is presented in Figure 7.5. β-phase formation is eliminated as a possible mechanism because little β-phase formation occurs at this rate. Unlike the cell cycled at 0.5C in Figure 7.2, the estimated active material loss in the first 100 cycles cannot be entirely attributed to poor wetting, so other sources of active material loss remain in the diagram. We do know based on the revival experiment that some material becomes inaccessible due to the wetting issue, so that pathway is highlighted. We see evidence of slower Li diffusion processes in the particles that is not recoverable upon cell revival, so the solid phase ionic impedance increase leading to a cell impedance increase is highlighted as well.

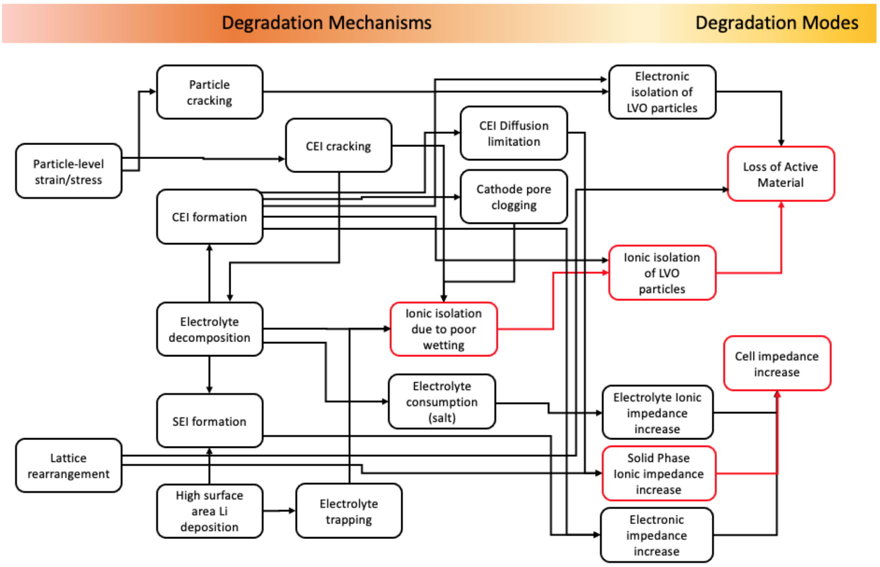

Figure 7.5: A map of possible degradation mechanisms, eliminating some and placing more confidence in others, based on the original space of hypothesized mechanisms in Figure 7.1 and interpretation of parameter estimates in Figure 7.4.

Table 7.2 provides a more general framework for interpreting parameter estimates as it pertains to various hypothesized degradation mechanisms in these cells. For each mechanism, the expectation for the estimated $\%AM$, as well as an estimated particle diffusivity D and reaction rate constant k_{rxn} is suggested both over the course of cycling and on cell revival. However, since these mechanisms are not mutually exclusive and we have not yet quantified, for example, how much of a decrease in k_{rxn} corresponds to a given CEI thickness, further experimentation is needed to extract more quantitative insight out of the analysis.

Mechanism	$\%AM$	D	k_{rxn}
Electrolyte consumption and poor wetting	Decrease when electrolyte volume falls below pore volume. Bounce back on revival.	Decrease if particles are not uniformly wetted because of longer diffusion length scale, and subsequent increase if particles are re-wetted on revival.	Possible changes that would reset on revival if electrolyte composition changes.
SEI			Decrease due to anode side impedance increase that should recover on revival.
CEI	Decrease if particles become ionically isolated by CEI which cannot be recovered on revival.	Increase if CEI limits Li diffusion.	Change if CEI affects electronic (charge transfer) impedance.
Lattice rearrangement	Irreversible decrease if Li is trapped in regions of the particle.	Change (decrease or increase) that would be unaffected by revival.	Possible effect if occuring on particle surfaces. Coupled with CEI.
Particle Fracture	Decrease from electronic isolation that likely would not be able to be recovered on revival.	Increase in effective diffusivity because of decrease in length scale if cracking occurs in a way that exposes more surface area for (de)lithiation.	Decrease if cracking occurs in a way that exposes more surface area.

Table 7.2: Qualitative description of expectations for different parameter estimates if different degradation mechanisms are active. The mechanisms are, however, not mutually exclusive so a superposition of these expectations is likely observed.

Figure 7.6 shows the parameter estimates for all the cells explored in our study. Some cells underwent the revival process, while others did not. No cells cycled at 0.2C underwent revival. The first row shows the discharge capacity measurements as well as the model-predicted capacity measurements based on the parameter estimates but in the absence of any active material loss.

Examining the entire data set, what is immediately apparent is that cell-to-cell variation is non-negligible. Though the trajectory of capacity fade and the parameter estimates is repeatable for cells cycled at each C-rate, the absolute values of the parameter estimates (e.g. the cycle 1 starting value, the peak value in the first 100 cycles, or the cycle at which a parameter passes through a minima or maxima) vary. The variation in cell performance, and subsequent variation in parameter estimates on cell revival makes commenting on degradation mechanisms from Figure

7.1 and Table 7.2 at a specific C-rate especially difficult. For instance, in the three cells cycled at 1C that underwent a cell revival (third column in Figure 7.6), we see one cell that improves its capacity on revival, while two others appear to lose capacity after the revival process. When examining the $\%AM$ parameter estimates for these three cells, we see that the blue colored cell that recovered some capacity recovers some of the active material, while the green colored cell maintains the same value and the pink colored cell is estimated to have less active material on revival. Based on these results, a much larger data set would be required to overcome the lab-scale cell to cell variation and comment on degradation mechanisms at different C-rates. This type of analysis on a larger data set could provide meaningful insight on how manufacturing variation impacts variation in degradation behavior.

The extent of active material loss does not appear to depend too strongly on C-rate given the variance in the data. Cells at all the rates appear to contain between 60% and 80% of their active material still ionically and electronically accessible after 100 cycles.

When considering D_j and $k_{rxn,j}$, there seems to be a clear delineation between cells cycled at 1C and above and cells cycled at 0.5C and below. These parameter estimates for the cells cycled at the higher rates appear not to change significantly over the course of cycling, though even small changes will have a larger impact in observed capacity at these rates. However, the cells cycled at lower rates undergo much more drastic changes in these parameters. The α-phase parameters degrade anywhere from one to two orders of magnitude, while the β-phase parameters improve by roughly the same amount. In the case of the two 0.5C cells that underwent revival, the changes in the α-phase parameters are not entirely reversible when new electrolyte and anode are added, indicated that some structural rearrangement could be occurring in the particles. That the α and β-phase diffusivities seem to converge on a similar value ($10^{-14}\ cm^2\ s^{-1}$) could be indicative of lattice rearrangement and convergence of transport pathways for Li in either phase.

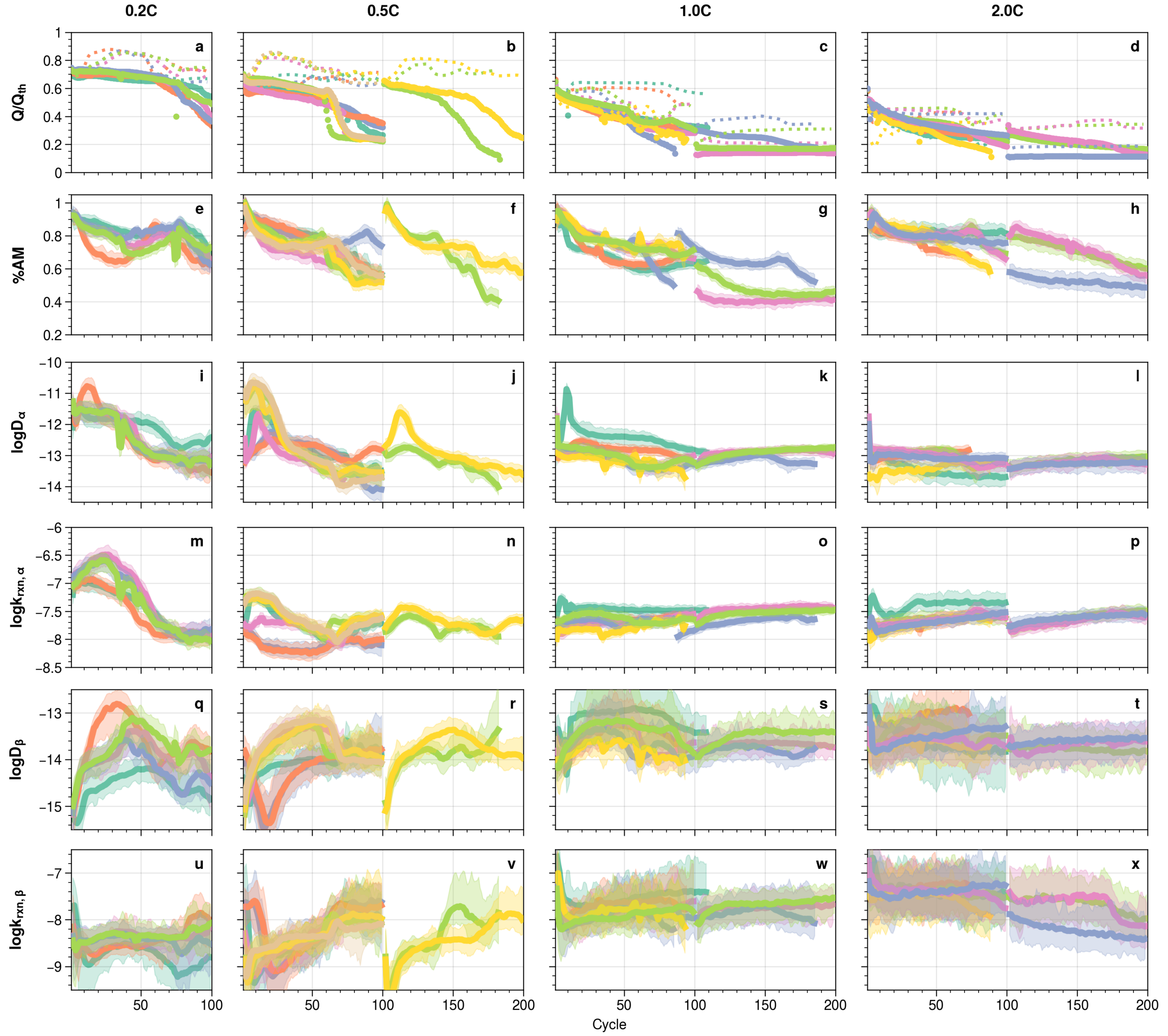

Figure 7.6: Parameter estimates for cells cycled at rates between 0.2C and 2C. Each column represents a group of cells cycled under the same conditions. The top row (a-d) show the experimentally observed discharge capacity as points and the model-predicted discharge capacity in the absence of active material loss as a dotted line, as was done in Figures 7.2 and 7.4. (e-x) Parameter estimates based on discharge curve at each cycle, presented as a 3 cycle rolling average. Shaded regions show 90% confidence interval in the estimate.

7.4 Conclusions

In this paper, we introduce an example of degradation analysis by refitting a physics-based electrochemical model to experimental data over the course of cycling. We show how to interpret parameter estimates, which are connected to degradation modes, in the context of different hypotheses for degradation mechanisms. By passing the parameter estimates back into the physics-based model, the amount of capacity fade that is attributed to inaccessibility of active material versus ionic or electronic impedance increase can be quantified. We also demonstrate that a simple cell revival procedure can be helpful in attributing the amount of active material loss that is due to electrolyte consumption and consequent poor wetting, and can separate observed impedance increases in the original cell between the anode and cathode. Based on all this information, a large space of possible degradation mechanisms can be narrowed, helping further focus resource utilization to better understand degradation. Though the variation in this data set was too large to be able to definitively describe degradation mechanisms for LVO under the C-rates studied, the insights derived from this study will be useful towards understanding the complex degradation behavior of these cathodes in future studies.

7.5 Supporting Information

7.5.1 Data Generation

A validated physics-based model,[32,165] was used to generate training data for the neural network that is described in this study. 3072 samples were chosen in a seven parameter space, with the bounds described in Table 7.1. These parameter samples were each used to parameterize the physics-based model and simulate a discharge. Of these simulations, 2170 simulations returned physically representative discharge curves (i.e. simulations ran without numerical issues). 80% of this data was used for training and 20% was held as an independent test set.

7.5.2 NN training

Featurization

The discharge curves were converted into a vector of features using an approach similar to that of Attia and Severson.[149,153]. Since each discharge is always between the same upper and lower voltage limits, we take the time at a specified grid of voltages between the upper and lower cutoff voltages as the feature representation of the discharge curve. The time values are multiplied by the C-rate (C_r), resulting in feature values (tC_r) on the order unity. This transformation is done for simplicity, and because features of order unity are preferred in certain ML models.[192] Features were chosen every 50 mV between 3.75 V and 2.0 V. The C-rate was appended as a feature at the end of the vector of features representing the discharge curve.

Data Augmentation

Data augmentation is a strategy common in machine learning data preparation that adds noise to the training data to improve ML model robustness and increase the training set size. In our approach, we perform a simple data augmentation approach of shifting voltage curves by random values of tC_r, maintaining the curvature of the discharge curve but adding more training data without performing any more simulations.[199] A random value of tC_r is chosen between 0 and 0.25

eight times for each discharge curve, resulting in a data set that is 8x the size of the original data set.

Sample Weighting

Because a continuous range of C-rates was chosen in the data generation step (Section 7.5.1) but the experiments were performed on a discrete set of four C-rates which are of course known prior to experimentation, we wanted to emphasize accuracy at the C-rates that would be tested. To do this, some samples closer to 0.2C, 0.5C, 1C and 2C were valued more than others during the training. The sample weighting as a function of C-rate chosen during the NN training is shown in Figure 7.7. When calculating the loss function, a weighted average using these weights is employed.

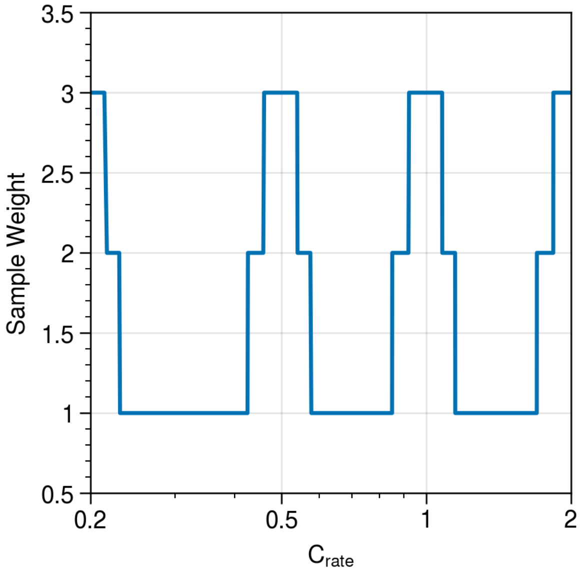

Figure 7.7: Sample weight as a function of sample C-rate for calculating a weighted average loss during training.

Training Specifics

A four layer neural network was used based on network size optimization in our previous results,[199] implemented using keras.[193] The input layer has 37 nodes (see featurization description in Section 7.5.2. There are two hidden layers with 130 nodes and 160 nodes respectively. The output layer is of size 5.

Training is performed with the Adam optimizer, relu activation functions, batch size of 64, and a mean squared error loss, weighted as described in Section 7.5.2 for 1500 epochs. 20 % of the training set is used for validation. The learning curve is shown in Figure 7.8. During training, the learning rate is reduced by a factor of two if the loss does not improve by 0.0005 in 50 epochs, implemented using ReduceLROnPleateau in Keras.[193] The learning rate starts at 0.01 and the minimum learning rate is set to 0.0001. The epochs at which the learning rate is reduced can be seen in the step changes in the loss in Figure 7.8.

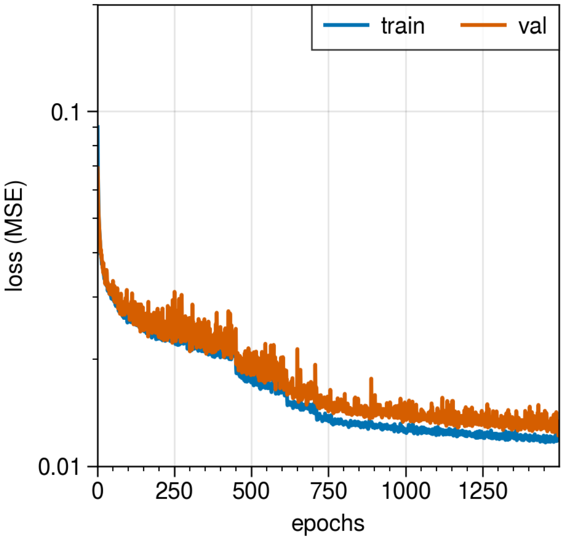

Figure 7.8: Learning curve during NN training, with mean squared error loss presented on a log scale.

To model an uncertainty in each parameter estimate, Monte Carlo dropout was applied.[200] A dropout ratio of 0.1 is applied after each hidden layer. When evaluating the trained neural network, for each test discharge curve (or experimental discharge curve), a distribution of outcomes can be predicted for the outputs based on multiple evaluations. Reported estimates in this paper are reported as representations of distributions based on 50 evaluations of the trained neural network, randomly dropping out 10% of the nodes after each hidden layer on each evaluation.

Uncertainty Calibration

We employ a post-training calibration algorithm proposed by Kuleshov et al., that essentially ensures that the 90% confidence interval of an estimate contains the true value 90% of the time (i.e. in 90% of the training set).[201] In this approach, an isotonic regression is used to map the desired empirical cumulative distribution function to the predicted cumulative distribution function. Then, if a 90% confidence interval is desired based on the 5% and 95% quantiles, the corresponding quantiles in the predicted distribution function can be determined.

Accuracy Results

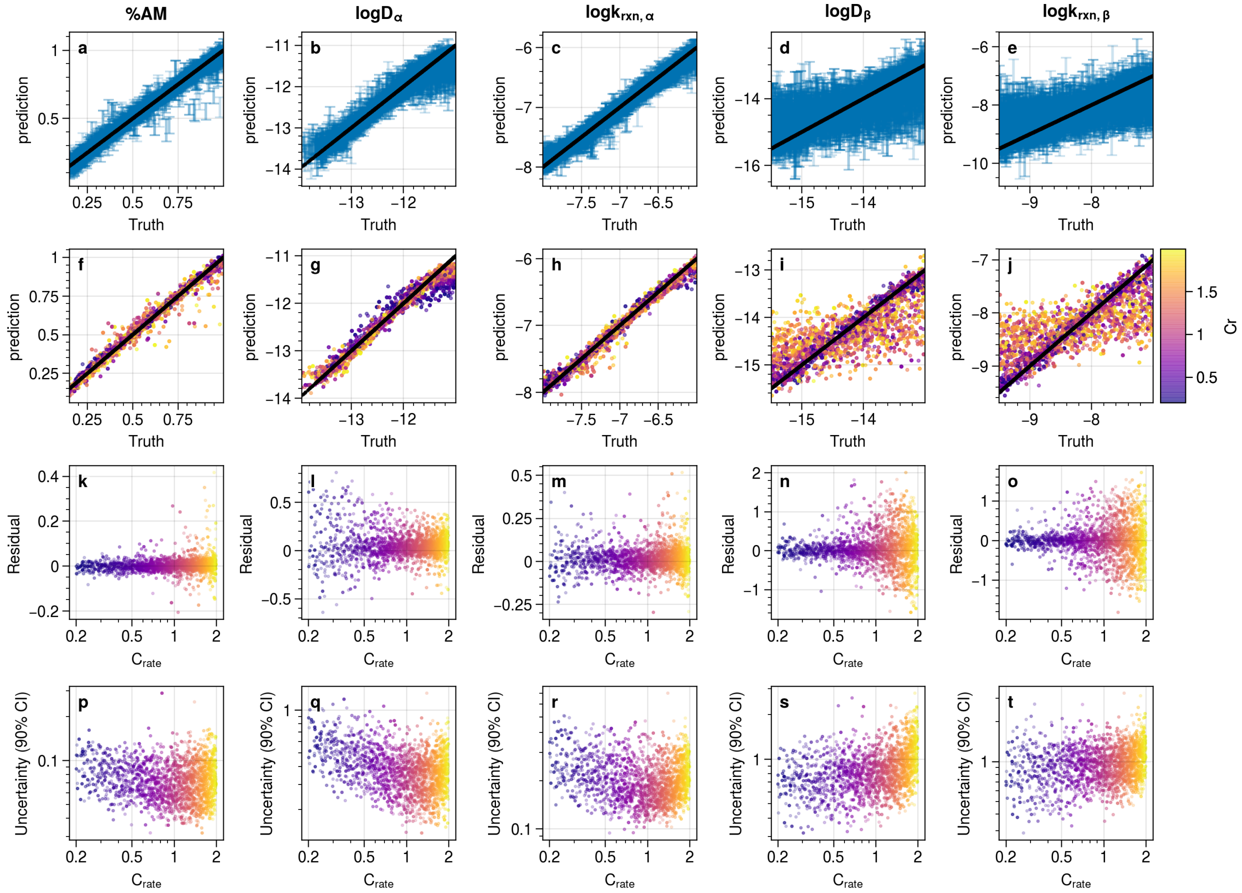

Figure 7.9: Accuracy results for the trained neural network with calibrated uncertainty as applied to the test set is shown in Figure 7.5.2. The top row shows prediction versus truth, with uncertainties (90% confidence interval). The second row shows the same information without uncertainties but colored by the C-rate. It is apparent that above 1C, estimates of the β-phase parameters are highly inaccurate. The third row shows the residuals as a function of C-rate, and the fourth row shows the uncertainty as a function of C-rate.

Chapter 8

Conclusions and Outlook

8.1 Utility of physics-based electrochemical models

This dissertation has provided multiple examples of the utility of physics-based electrochemical models in understanding the underlying physics batteries. The ability to "look under the hood" and understand how concentration and potential distributions affect observable electrochemical behavior affords scientists deeper physical insight than is readily available via experiment. Chapter 2 showed how a model could be used to probe complex particle-scale physics in LVO cathodes. Chapter 3 used physics-based models to explore the effects of tortuosity on high-rate discharge performance of LVO and NMC cathodes. Chapters 4, 6, and 7 discussed insights into degradation of the lithium trivandate cathode derived from a model-based analysis. Models are also useful for optimization of design (Chapter 2), design of experiments (Chapters 3 and 4), and parameter estimation (all chapters).

8.2 Estimating parameters directly from experiment

When model parameters can be isolated and measured independently with a high degree of confidence, good predictive ability, and low resource utilization, this approach should always be taken. However, if any of these challenges become a roadblock to model parameterization, fitting a model directly to experiment and estimating parameters is a viable alternative. Thermodynamic, kinetic, and transport parameters for lithiation of the β-phase of LVO were fit in Chapter 2. Similarly, the inconsistently measured and ambiguously defined effective electrode scale transport property, tortuosity, was fit directly to rate capability experiments in Chapter 3. When fitting parameters, it is important to independently validate fits with independent data sets if the parameterized model will be used for prediction.

Some model parameters cannot be decoupled in the model, i.e. the parameters are not structurally identifiable. This must be noted before any parameter estimation task is undertaken. Examples of this consideration were provided in Chapters 3, 5, and 7. The other important aspect of parameter estimation is to ensure that the model is sensitive to the parameter before proceeding with estimation. Higher model sensitivity will generally translate to more precise (i.e. low uncertainty) estimates. Chapters 3 and 7 explored the idea of model sensitivity and its impact on parameter uncertainty in further detail.

In general, this dissertation places more emphasis on parameter uncertainty than has typically been done in the battery modeling literature. Quantifying parameter uncertainty is helpful in interpretation and useful in prediction. The ability to predict a range of possible outcomes for electrochemical performance is valuable along all parts of the decision making processes when designing and using batteries.

8.3 Machine Learning to accelerate parameter estimation

The concept of training inverse machine learning models that map electrochemical performance to physics-based model parameters was explored extensively in Chapters 5-7. While the examples in these chapters were presented in the context of fitting parameters for degradation tracking, the concepts are more generally applicable to any parameter estimation task. It is, however, important to know the constraints of a machine learning model. These constraints were documented and explored in the relevant chapters.

Of particular interest was the susceptibility of ML models to disagreement between the physics-based model used to generate the training data and the experimental data of interest. Two case studies for these discrepancies, their impact on ML model accuracy, and strategies to mitigate inaccuracy were provided in Chapter 6. We hope this type of analysis is adopted more widely in the community as others look to implement ML solutions trained on synthetic data.

8.4 Physics-based models for degradation tracking

The largest contribution of the work in this dissertation was outlining a workflow for using physics-based models to track degradation in batteries. Through the model system of LVO cathodes in half cells, a detailed framework is provided in Chapters 4 and 7 for parameter estimation over the course of cycling and interpretation of parameter estimates to test degradation mechanism hypotheses. Chapter 7 discussed in further detail the synergistic benefit of experimental design and parameter estimation analysis in eliminating possible degradation mechanisms. Future directions for this research include more combinations of unique experimental design to isolate different degradation phenomena beyond what was done in Chapter 7.

References

[1] S. Nalley and A. LaRose, "Annual Energy Outlook 2022 (AEO2022)," *Energy Information Agency*, p. 23, Mar. 2022.

[2] J. Frith, "Lithium-Ion Batteries The Incumbent Technology," *Bloomberg New Energy Fund*, p. 21, 2018.

[3] Y. Ding, Z. P. Cano, A. Yu, J. Lu, and Z. Chen, "Automotive Li-Ion Batteries: Current Status and Future Perspectives," *Electrochem. Energ. Rev.*, vol. 2, no. 1, pp. 1–28, Mar. 2019.

[4] M. S. E. Houache, C.-H. Yim, Z. Karkar, and Y. Abu-Lebdeh, "On the Current and Future Outlook of Battery Chemistries for Electric Vehicles—Mini Review," *Batteries*, vol. 8, no. 7, p. 70, Jul. 2022.

[5] T. M. Gür, "Review of electrical energy storage technologies, materials and systems: Challenges and prospects for large-scale grid storage," *Energy & Environmental Science*, vol. 11, no. 10, pp. 2696–2767, 2018.

[6] A. Manthiram, "An Outlook on Lithium Ion Battery Technology," *ACS Cent Sci*, vol. 3, no. 10, pp. 1063–1069, Oct. 2017.

[7] J. Deng, C. Bae, J. Marcicki, A. Masias, and T. Miller, "Safety modelling and testing of lithium-ion batteries in electrified vehicles," *Nat Energy*, vol. 3, no. 4, pp. 261–266, Apr. 2018.

[8] J.-M. Tarascon and M. Armand, "Issues and challenges facing rechargeable lithium batteries," *Nature*, vol. 414, no. 6861, pp. 359–367, Nov. 2001.

[9] N. Nitta, F. Wu, J. T. Lee, and G. Yushin, "Li-ion battery materials: Present and future," *Materials Today*, vol. 18, no. 5, pp. 252–264, Jun. 2015.

[10] D. Andre, H. Hain, P. Lamp, F. Maglia, and B. Stiaszny, "Future high-energy density anode materials from an automotive application perspective," *Journal of Materials Chemistry A*, vol. 5, no. 33, pp. 17 174–17 198, 2017.

[11] K. J. Kim, M. Balaish, M. Wadaguchi, L. Kong, and J. L. M. Rupp, "Solid-State Li–Metal Batteries: Challenges and Horizons of Oxide and Sulfide Solid Electrolytes and Their Interfaces," *Adv. Energy Mater.*, vol. 11, no. 1, p. 2 002 689, Jan. 2021.

[12] K. Chayambuka, G. Mulder, D. L. Danilov, and P. H. L. Notten, “From Li-Ion Batteries toward Na-Ion Chemistries: Challenges and Opportunities,” *Advanced Energy Materials*, vol. 10, no. 38, p. 2 001 310, 2020.

[13] A. Mistry, A. A. Franco, S. J. Cooper, S. A. Roberts, and V. Viswanathan, “How Machine Learning Will Revolutionize Electrochemical Sciences,” *ACS Energy Lett.*, pp. 1422–1431, Mar. 2021.

[14] T. F. Fuller, M. Doyle, and J. Newman, “Simulation and Optimization of the Dual Lithium Ion Insertion Cell,” *Journal of The Electrochemical Society*, vol. 141, no. 1, p. 1, 1994.

[15] S. Atlung, K. West, and T. Jacobsen, “Dynamic Aspects of Solid Solution Cathodes for Electrochemical Power Sources,” *J. Electrochem. Soc.*, vol. 126, no. 8, pp. 1311–1321, Aug. 1979.

[16] E. Prada, D. Di Domenico, Y. Creff, J. Bernard, V. Sauvant-Moynot, and F. Huet, “Simplified Electrochemical and Thermal Model of LiFePO $_4$ -Graphite Li-Ion Batteries for Fast Charge Applications,” *J. Electrochem. Soc.*, vol. 159, no. 9, A1508–A1519, 2012.

[17] J. Li, N. Lotfi, R. G. Landers, and J. Park, “A Single Particle Model for Lithium-Ion Batteries with Electrolyte and Stress-Enhanced Diffusion Physics,” *Journal of The Electrochemical Society*, vol. 164, no. 4, A874–A883, 2017.

[18] S. G. Marquis, V. Sulzer, R. Timms, C. P. Please, and S. J. Chapman, “An Asymptotic Derivation of a Single Particle Model with Electrolyte,” *Journal of The Electrochemical Society*, vol. 166, no. 15, A3693–A3706, 2019.

[19] A. M. Bizeray, J. Kim, S. R. Duncan, and D. A. Howey, “Identifiability and Parameter Estimation of the Single Particle Lithium-Ion Battery Model,” *IEEE Transactions on Control Systems Technology*, vol. 27, no. 5, pp. 1862–1877, Sep. 2019.

[20] B. Yan, C. Lim, L. Yin, and L. Zhu, “Three Dimensional Simulation of Galvanostatic Discharge of LiCoO $_2$ Cathode Based on X-ray Nano-CT Images,” *J. Electrochem. Soc.*, vol. 159, no. 10, A1604–A1614, 2012.

[21] F. L. E. Usseglio-Viretta *et al.*, “Quantitative Relationships Between Pore Tortuosity, Pore Topology, and Solid Particle Morphology Using a Novel Discrete Particle Size Algorithm,” *J. Electrochem. Soc.*, vol. 167, no. 10, p. 100 513, Jun. 2020.

[22] G. G. Botte, V. R. Subramanian, and R. E. White, “Mathematical modeling of secondary lithium batteries,” *J. Electrochem. Acta*, pp. 2595–2609, 2000.

[23] W. Ai, L. Kraft, J. Sturm, A. Jossen, and B. Wu, “Electrochemical Thermal-Mechanical Modelling of Stress Inhomogeneity in Lithium-Ion Pouch Cells,” *Journal of The Electrochemical Society*, vol. 167, no. 1, p. 013 512, 2020.

[24] W. H. Woodford, Y.-M. Chiang, and W. C. Carter, "“Electrochemical Shock” of Intercalation Electrodes: A Fracture Mechanics Analysis," *Journal of The Electrochemical Society*, vol. 157, no. 10, A1052, 2010.

[25] W. Tiedemann and J. Newman, "Maximum Effective Capacity in an Ohmically Limited Porous Electrode," *J. Electrochem. Soc.*, vol. 122, no. 11, p. 1482, 1975.

[26] J. Newman, "Optimization of Porosity and Thickness of a Battery Electrode by Means of a Reaction-Zone Model," *J. Electrochem. Soc.*, vol. 142, no. 1, p. 97, 1995.

[27] V. Srinivasan and J. Newman, "Design and Optimization of a Natural Graphite/Iron Phosphate Lithium-Ion Cell," *J. Electrochem. Soc.*, vol. 151, no. 10, A1530, 2004.

[28] S. Yu, S. Kim, T. Y. Kim, J. H. Nam, and W. I. Cho, "Model Prediction and Experiments for the Electrode Design Optimization of LiFePO $_4$ /Graphite Electrodes in High Capacity Lithium-ion Batteries," *Bulletin of the Korean Chemical Society*, vol. 34, no. 1, pp. 79–88, Jan. 2013.

[29] S. De, P. W. Northrop, V. Ramadesigan, and V. R. Subramanian, "Model-based simultaneous optimization of multiple design parameters for lithium-ion batteries for maximization of energy density," *Journal of Power Sources*, vol. 227, pp. 161–170, Apr. 2013.

[30] K. G. Gallagher *et al.*, "Optimizing Areal Capacities through Understanding the Limitations of Lithium-Ion Electrodes," *J. Electrochem. Soc.*, vol. 163, no. 2, A138–A149, 2016.

[31] S. Malifarge, B. Delobel, and C. Delacourt, "Determination of Tortuosity Using Impedance Spectra Analysis of Symmetric Cell," *Journal of The Electrochemical Society*, vol. 164, no. 11, E3329–E3334, 2017.

[32] K. Mayilvahanan *et al.*, "Design Principles to Govern Electrode Fabrication for the Lithium Trivanadate Cathode," *Journal of The Electrochemical Society*, vol. 167, no. 10, p. 100 503, May 2020.

[33] Z. Hui *et al.*, "Optimal electrode-scale design of Li-ion electrodes: A general correlation," *Energy Storage Materials*, vol. 39, pp. 176–185, Aug. 2021.

[34] V. Ramadesigan, R. N. Methekar, F. Latinwo, R. D. Braatz, and V. R. Subramanian, "Optimal Porosity Distribution for Minimized Ohmic Drop across a Porous Electrode," *J. Electrochem. Soc.*, vol. 157, no. 12, A1328, 2010.

[35] Z. Hui *et al.*, "Transport In and Optimization of Aligned-Channel Li-Ion Electrode Architectures," *J. Electrochem. Soc.*, vol. 168, no. 10, p. 100 536, Oct. 2021.

[36] N. A. Chaturvedi, R. Klein, J. Christensen, J. Ahmed, and A. Kojic, “Algorithms for Advanced Battery-Management Systems,” *IEEE Control Systems Magazine*, vol. 30, no. 3, pp. 49–68, Jun. 2010.

[37] G. Fan, “Systematic parameter identification of a control-oriented electrochemical battery model and its application for state of charge estimation at various operating conditions,” *Journal of Power Sources*, vol. 470, p. 228 153, Sep. 2020.

[38] S. J. Moura, *Estimation and Control of Battery Electrochemistry Models: A Tutorial*.

[39] H. Perez, N. Shahmohammadhamedani, and S. Moura, “Enhanced Performance of Li-Ion Batteries via Modified Reference Governors and Electrochemical Models,” *IEEE/ASME Transactions on Mechatronics*, vol. 20, no. 4, pp. 1511–1520, Aug. 2015.

[40] J. Song *et al.*, “Pathways towards managing cost and degradation risk of fast charging cells with electrical and thermal controls,” *Energy Environ. Sci.*, vol. 14, no. 12, pp. 6564–6573, 2021.

[41] E. J. Dufek *et al.*, “Developing extreme fast charge battery protocols – A review spanning materials to systems,” *Journal of Power Sources*, vol. 526, p. 231 129, Apr. 2022.

[42] N. W. Brady *et al.*, “Operando Study of LiV_3O_8 Cathode: Coupling EDXRD Measurements to Simulations,” *J. Electrochem. Soc.*, vol. 165, no. 2, A371–A379, 2018.

[43] K. S. Mayilvahanan *et al.*, “Quantifying Uncertainty in Tortuosity Estimates for Porous Electrodes,” *J. Electrochem. Soc.*, vol. 168, no. 7, p. 070 537, Jul. 2021.

[44] P. Arora, “Capacity Fade Mechanisms and Side Reactions in Lithium-Ion Batteries,” *Journal of The Electrochemical Society*, vol. 145, no. 10, p. 3647, 1998.

[45] M. Safari, M. Morcrette, A. Teyssot, and C. Delacourt, “Multimodal Physics-Based Aging Model for Life Prediction of Li-Ion Batteries,” *Journal of The Electrochemical Society*, vol. 156, no. 3, A145, 2009.

[46] Y. Dai, L. Cai, and R. E. White, “Capacity Fade Model for Spinel $LiMn_2O_4$ Electrode,” *Journal of The Electrochemical Society*, vol. 160, no. 1, A182–A190, 2013.

[47] R. Narayanrao, M. M. Joglekar, and S. Inguva, “A Phenomenological Degradation Model for Cyclic Aging of Lithium Ion Cell Materials,” *J. Electrochem. Soc.*, vol. 160, no. 1, A125–A137, 2013.

[48] J. M. Reniers, G. Mulder, and D. A. Howey, “Review and Performance Comparison of Mechanical-Chemical Degradation Models for Lithium-Ion Batteries,” *Journal of The Electrochemical Society*, vol. 166, no. 14, A3189–A3200, 2019.

[49] S. E. J. O'Kane *et al.*, "Lithium-ion battery degradation: How to model it," *Phys. Chem. Chem. Phys.*, vol. 24, no. 13, pp. 7909–7922, 2022.

[50] C.-H. Chen, F. Brosa Planella, K. O'Regan, D. Gastol, W. D. Widanage, and E. Kendrick, "Development of Experimental Techniques for Parameterization of Multi-scale Lithium-ion Battery Models," *Journal of The Electrochemical Society*, vol. 167, no. 8, p. 080 534, May 2020.

[51] A. S. Tracey, G. R. Willsky, and E. S. Takeuchi, *Vanadium: Chemistry, Biochemistry, Pharmacology and Practical Applications*, First. New York: Taylor & Francis Group, 2007.

[52] G Pistoia and M. P. M. Tocci, "Li/LiI+xV308 Secondary Batteries," *J. Electrochem. Soc.*, vol. 132, no. 2, p. 4, 1985.

[53] G. Pistoia, S. Panero, M. Tocci, R. V. Moshtev, and V. Manev, "Solid solutions Li1+xV3O8 as cathodes for high rate secondary Li batteries," *Solid State Ionics*, vol. 13, no. 4, pp. 311–318, Aug. 1984.

[54] J. Garche, C. K. Dyer, P. T. Moseley, Z. Ogumi, D. A. J. Rand, and B. Scrosati, *Encyclopedia of Electrochemical Power Sources*. Newnes, May 2013, ISBN: 978-0-444-52745-5.

[55] Q. Zhang *et al.*, "Investigation of Structural Evolution of Li $_{1.1}$ V $_{3}$ O $_{8}$ by *In Situ* X-ray Diffraction and Density Functional Theory Calculations," *Chem. Mater.*, vol. 29, no. 5, pp. 2364–2373, Mar. 2017.

[56] L. A. de Picciotto, K. T. Adendorff, D. C. Liles, and M. M. Thackeray, "Structural characterization of Li1+xV3O8 insertion electrodes by single-crystal X-ray diffraction," *Solid State Ionics*, vol. 62, no. 3, pp. 297–307, Aug. 1993.

[57] J. Kawakita, T. Miura, and T. Kishi, "Lithium insertion and extraction kinetics of Li1qxV3O8," p. 5, 1999.

[58] Q. Zhang *et al.*, "Impact of Synthesis Method on Phase Transformations of Layered Lithium Vanadium Oxide upon Electrochemical (De)lithiation," *J. Electrochem. Soc.*, vol. 166, no. 4, A771–A778, 2019.

[59] J. Xu, H. Zhang, T. Zhang, Q. Pan, and Y. Gui, "Influence of heat-treatment temperature on crystal structure, morphology and electrochemical properties of LiV3O8 prepared by hydrothermal reaction," *Journal of Alloys and Compounds*, vol. 467, no. 1-2, pp. 327–331, Jan. 2009.

[60] X. Cao, L. Xie, H. Zhan, and Y. Zhou, "Large-scale synthesis of Li1.2V3O8 as a cathode material for lithium secondary battery via a soft chemistry route," *Materials Research Bulletin*, vol. 44, no. 2, pp. 472–477, Feb. 2009.

[61] S. Huang *et al.*, “Facile synthesis of cookies-shaped LiV3O8 cathode materials with good cycling performance for lithium-ion batteries,” *Journal of Alloys and Compounds*, vol. 584, pp. 41–46, Jan. 2014.

[62] Q. Zhang *et al.*, “Visualization of structural evolution and phase distribution of a lithium vanadium oxide (Li $_{1.1}$ V $_{3}$ O $_{8}$) electrode via an operando and in situ energy dispersive X-ray diffraction technique,” *Physical Chemistry Chemical Physics*, vol. 19, no. 21, pp. 14 160–14 169, 2017.

[63] S. Jouanneau, A. Verbaere, and D. Guyomard, “A combined X-ray and neutron Rietveld study of the chemically lithiated electrode materials Li2.7V3O8 and Li4.8V3O8,” *Journal of Solid State Chemistry*, vol. 178, no. 1, pp. 22–27, Jan. 2005.

[64] N. W. Brady *et al.*, “Discharge, Relaxation, and Charge Model for the Lithium Trivanadate Electrode: Reactions, Phase Change, and Transport,” *J. Electrochem. Soc.*, vol. 163, no. 14, A2890–A2898, 2016.

[65] M. Wentker, M. Greenwood, and J. Leker, “A Bottom-Up Approach to Lithium-Ion Battery Cost Modeling with a Focus on Cathode Active Materials,” *Energies*, vol. 12, no. 3, p. 504, Feb. 2019.

[66] G. Patry, A. Romagny, S. Martinet, and D. Froelich, “Cost modeling of lithium-ion battery cells for automotive applications,” *Energy Science & Engineering*, vol. 3, no. 1, pp. 71–82, 2015.

[67] Z. Du, D. L. Wood, C. Daniel, S. Kalnaus, and J. Li, “Understanding limiting factors in thick electrode performance as applied to high energy density Li-ion batteries,” *Jour. App. Electrochem.*, vol. 47, no. 3, pp. 405–415, Mar. 2017.

[68] S.-L. Wu, A. E. Javier, D. Devaux, N. P. Balsara, and V. Srinivasan, “Discharge Characteristics of Lithium Battery Electrodes with a Semiconducting Polymer Studied by Continuum Modeling and Experiment,” *J. Electrochem. Soc.*, vol. 161, no. 12, A1836–A1843, 2014.

[69] D. E. Stephenson, E. M. Hartman, J. N. Harb, and D. R. Wheeler, “Modeling of Particle-Particle Interactions in Porous Cathodes for Lithium-Ion Batteries,” *J. Electrochem. Soc.*, vol. 154, no. 12, A1146, 2007.

[70] S. Jouanneau, A. Le Gal La Salle, A. Verbaere, and D. Guyomard, “The Origin of Capacity Fading upon Lithium Cycling in Li[sub 1.1]V[sub 3]O[sub 8],” *Journal of The Electrochemical Society*, vol. 152, no. 8, A1660, 2005.

[71] N. W. Brady, C. A. Gould, and A. C. West, “Quantitative Parameter Estimation, Model Selection, and Variable Selection in Battery Science,” *Journal of The Electrochemical Society*, vol. 167, no. 1, p. 013 501, 2020.

[72] D. A. G. Bruggeman, “Berechnung verschiedener physikalischer Konstanten von heterogenen Substanzen. I. Dielektrizitätskonstanten und Leitfähigkeiten der Mischkörper aus isotropen Substanzen,” *Annalen der Physik*, vol. 416, no. 8, pp. 665–679, 1935.

[73] M. Doyle, “Comparison of Modeling Predictions with Experimental Data from Plastic Lithium Ion Cells,” *J. Electrochem. Soc.*, vol. 143, no. 6, p. 1890, 1996.

[74] J. Landesfeind, J. Hattendorff, A. Ehrl, W. A. Wall, and H. A. Gasteiger, “Tortuosity Determination of Battery Electrodes and Separators by Impedance Spectroscopy,” *J. Electrochem. Soc.*, vol. 163, no. 7, A1373, 2016.

[75] G. Cunningham, M. Lotya, N. McEvoy, G. S. Duesberg, P. van der Schoot, and J. N. Coleman, “Percolation scaling in composites of exfoliated MoS2 filled with nanotubes and graphene,” *Nanoscale*, vol. 4, no. 20, p. 6260, 2012.

[76] D. Guy, B. Lestriez, R. Bouchet, V. Gaudefroy, and D. Guyomard, “Novel architecture of composite electrode for optimization of lithium battery performance,” *Journal of Power Sources*, vol. 157, no. 1, pp. 438–442, Jun. 2006.

[77] W. Bauhofer and J. Z. Kovacs, “A review and analysis of electrical percolation in carbon nanotube polymer composites,” *Composites Science and Technology*, vol. 69, no. 10, pp. 1486–1498, Aug. 2009.

[78] B. Zhang, Y. Yu, Y. Liu, Z.-D. Huang, Y.-b. He, and J.-K. Kim, “Percolation threshold of graphene nanosheets as conductive additives in Li4Ti5O12 anodes of Li-ion batteries,” *Nanoscale*, vol. 5, no. 5, p. 2100, 2013.

[79] X.-M. Liu *et al.*, “Carbon nanotube (CNT)-based composites as electrode material for rechargeable Li-ion batteries: A review,” *Composites Science and Technology*, vol. 72, no. 2, pp. 121–144, Jan. 2012.

[80] J. Wu and D. S. McLachlan, “Percolation exponents and thresholds obtained from the nearly ideal continuum percolation system graphite-boron nitride,” *Physical Review B*, vol. 56, no. 3, pp. 1236–1248, Jul. 1997.

[81] D. Stauffer and A. Aharony, *Introduction To Percolation Theory Revised Second Edition*. Hoboken: Taylor and Francis, 2014, ISBN: 978-0-7484-0027-0 978-0-203-21159-5.

[82] J. Newman and K. E. Thomas-Alyea, *Electrochemical Systems*, 3rd. Hoboken, NJ: John Wiley & Sons, Inc., 2004.

[83] B. Tjaden, D. J. L. Brett, and P. R. Shearing, “Tortuosity in electrochemical devices: A review of calculation approaches,” *International Materials Reviews*, vol. 63, no. 2, pp. 47–67, Feb. 2018.

[84] R. B. MacMullin and G. A. Muccini, "Characteristics of porous beds and structures," *AIChE Journal*, vol. 2, no. 3, pp. 393–403, Sep. 1956.

[85] M. Ebner, F. Geldmacher, F. Marone, M. Stampanoni, and V. Wood, "X-Ray Tomography of Porous, Transition Metal Oxide Based Lithium Ion Battery Electrodes," *Advanced Energy Materials*, vol. 3, no. 7, pp. 845–850, 2013.

[86] M. Ebner and V. Wood, "Tool for Tortuosity Estimation in Lithium Ion Battery Porous Electrodes," *J. Electrochem. Soc.*, vol. 162, no. 2, A3064, 2015.

[87] S. Cooper, A. Bertei, P. Shearing, J. Kilner, and N. Brandon, "TauFactor: An open-source application for calculating tortuosity factors from tomographic data," *SoftwareX*, vol. 5, pp. 203–210, 2016.

[88] N. A. Zacharias, D. R. Nevers, C. Skelton, K. Knackstedt, D. E. Stephenson, and D. R. Wheeler, "Direct Measurements of Effective Ionic Transport in Porous Li-Ion Electrodes," *Journal of The Electrochemical Society*, vol. 160, no. 2, A306–A311, 2013.

[89] J. Landesfeind, M. Ebner, A. Eldiven, V. Wood, and H. A. Gasteiger, "Tortuosity of Battery Electrodes: Validation of Impedance-Derived Values and Critical Comparison with 3D Tomography," *Journal of The Electrochemical Society*, vol. 165, no. 3, A469–A476, 2018.

[90] J. Landesfeind, A. Eldiven, and H. A. Gasteiger, "Influence of the Binder on Lithium Ion Battery Electrode Tortuosity and Performance," *Journal of The Electrochemical Society*, vol. 165, no. 5, A1122–A1128, 2018.

[91] A. N. Mistry, K. Smith, and P. P. Mukherjee, "Secondary-Phase Stochastics in Lithium-Ion Battery Electrodes," *ACS Applied Materials & Interfaces*, vol. 10, no. 7, pp. 6317–6326, Feb. 2018.

[92] F. L. E. Usseglio-Viretta *et al.*, "Resolving the Discrepancy in Tortuosity Factor Estimation for Li-Ion Battery Electrodes through Micro-Macro Modeling and Experiment," *Journal of The Electrochemical Society*, vol. 165, no. 14, A3403–A3426, 2018.

[93] I. V. Thorat, D. E. Stephenson, N. A. Zacharias, K. Zaghib, J. N. Harb, and D. R. Wheeler, "Quantifying tortuosity in porous Li-ion battery materials," *Journal of Power Sources*, vol. 188, no. 2, pp. 592–600, Mar. 2009.

[94] A. Ehrl, J. Landesfeind, W. A. Wall, and H. A. Gasteiger, "Determination of Transport Parameters in Liquid Binary Lithium Ion Battery Electrolytes: I. Diffusion Coefficient," *Journal of The Electrochemical Society*, vol. 164, no. 4, A826–A836, 2017.

[95] J. Landesfeind and H. A. Gasteiger, "Temperature and Concentration Dependence of the Ionic Transport Properties of Lithium-Ion Battery Electrolytes," *Journal of The Electrochemical Society*, vol. 166, no. 14, A3079–A3097, 2019.

[96] R. de Levie, “On porous electrodes in electrolyte solutions,” *Electrochimica Acta*, vol. 8, no. 10, pp. 751–780, Oct. 1963.

[97] J. Huang *et al.*, “Editors’ Choice—Review—Impedance Response of Porous Electrodes: Theoretical Framework, Physical Models and Applications,” *Journal of The Electrochemical Society*, vol. 167, no. 16, p. 166 503, Nov. 2020.

[98] T.-T. Nguyen, A. Demortière, B. Fleutot, B. Delobel, C. Delacourt, and S. J. Cooper, “The electrode tortuosity factor: Why the conventional tortuosity factor is not well suited for quantifying transport in porous Li-ion battery electrodes and what to use instead,” *npj Computational Materials*, vol. 6, no. 1, Dec. 2020.

[99] W. Wang, D. Juarez-Robles, and P. P. Mukherjee, “Electroanalytical Quantification of Electrolyte Transport Resistance in Porous Electrodes,” *Journal of The Electrochemical Society*, vol. 167, no. 8, p. 080 510, Apr. 2020.

[100] F. Pouraghajan *et al.*, “Quantifying Tortuosity of Porous Li-Ion Battery Electrodes: Comparing Polarization-Interrupt and Blocking-Electrolyte Methods,” *Journal of The Electrochemical Society*, vol. 165, no. 11, A2644–A2653, 2018.

[101] M. Doyle, “Modeling of Galvanostatic Charge and Discharge of the Lithium/Polymer/Insertion Cell,” *Journal of The Electrochemical Society*, vol. 140, no. 6, p. 1526, 1993.

[102] D. P. Finegan *et al.*, “Characterising the structural properties of polymer separators for lithium-ion batteries in 3D using phase contrast X-ray microscopy,” *Journal of Power Sources*, vol. 333, pp. 184–192, Nov. 2016.

[103] S. G. Stewart and J. Newman, “The Use of UV/vis Absorption to Measure Diffusion Coefficients in LiPF[sub 6] Electrolytic Solutions,” *Journal of The Electrochemical Society*, vol. 155, no. 1, F13, 2008.

[104] K. Hayamizu, “Temperature Dependence of Self-Diffusion Coefficients of Ions and Solvents in Ethylene Carbonate, Propylene Carbonate, and Diethyl Carbonate Single Solutions and Ethylene Carbonate + Diethyl Carbonate Binary Solutions of LiPF $_6$ Studied by NMR,” *Journal of Chemical & Engineering Data*, vol. 57, no. 7, pp. 2012–2017, Jul. 2012.

[105] H. Lundgren, M. Behm, and G. Lindbergh, “Electrochemical Characterization and Temperature Dependency of Mass-Transport Properties of LiPF $_6$ in EC:DEC,” *Journal of The Electrochemical Society*, vol. 162, no. 3, A413–A420, 2015.

[106] Z. Feng, K. Higa, K. S. Han, and V. Srinivasan, “Evaluating Transport Properties and Ionic Dissociation of LiPF $_6$ in Concentrated Electrolyte,” *Journal of The Electrochemical Society*, vol. 164, no. 12, A2434–A2440, 2017.

[107] L. O. Valoøn and J. N. Reimers, “Transport Properties of LiPF[sub 6]-Based Li-Ion Battery Electrolytes,” *Journal of The Electrochemical Society*, vol. 152, no. 5, A882, 2005.

[108] Z. Hui, K. S. Mayilvahanan, Y. Yang, and A. C. West, “Determining the Length Scale of Transport Impedances in Li-Ion Electrodes: Li(Ni $_{0.33}$ Mn $_{0.33}$ Co $_{0.33}$)O $_{2}$,” *Journal of The Electrochemical Society*, vol. 167, no. 10, p. 100 542, Jun. 2020.

[109] D. S. Sivia and J. Skilling, *Data Analysis: A Bayesian Tutorial*, 2nd ed, ser. Oxford Science Publications. Oxford ; New York: Oxford University Press, 2006, ISBN: 978-0-19-856831-5.

[110] C. Heubner, M. Schneider, and A. Michaelis, “Diffusion-Limited C-Rate: A Fundamental Principle Quantifying the Intrinsic Limits of Li-Ion Batteries,” *Advanced Energy Materials*, vol. 10, no. 2, p. 1 902 523, Jan. 2020.

[111] C. Heubner *et al.*, “Semi-empirical master curve concept describing the rate capability of lithium insertion electrodes,” *Journal of Power Sources*, vol. 380, pp. 83–91, Mar. 2018.

[112] F. Jiang and P. Peng, “Elucidating the Performance Limitations of Lithium-ion Batteries due to Species and Charge Transport through Five Characteristic Parameters,” *Scientific Reports*, vol. 6, no. 1, Dec. 2016.

[113] B. Tjaden, S. J. Cooper, D. J. Brett, D. Kramer, and P. R. Shearing, “On the origin and application of the Bruggeman correlation for analysing transport phenomena in electrochemical systems,” *Current Opinion in Chemical Engineering*, vol. 12, pp. 44–51, May 2016.

[114] M. Singh, J. Kaiser, and H. Hahn, “Thick Electrodes for High Energy Lithium Ion Batteries,” *Journal of The Electrochemical Society*, vol. 162, no. 7, A1196–A1201, 2015.

[115] R. Morasch, J. Landesfeind, B. Suthar, and H. A. Gasteiger, “Detection of Binder Gradients Using Impedance Spectroscopy and Their Influence on the Tortuosity of Li-Ion Battery Graphite Electrodes,” *Journal of The Electrochemical Society*, vol. 165, no. 14, A3459–A3467, 2018.

[116] B. L. Trembacki, D. R. Noble, M. E. Ferraro, and S. A. Roberts, “Mesoscale Effects of Composition and Calendering in Lithium-Ion Battery Composite Electrodes,” *Journal of Electrochemical Energy Conversion and Storage*, vol. 17, no. 4, p. 041 001, Nov. 2020.

[117] D. C. Robertson *et al.*, “Effect of Anode Porosity and Temperature on the Performance and Lithium Plating During Fast-Charging of Lithium-Ion Cells,” *Energy Technol.*, vol. 9, no. 1, p. 2 000 666, Jan. 2021.

[118] A. Rohatgi, *Webplotdigitizer: Version 4.4*, 2020.

[119] M. D. Murbach, B. Gerwe, N. Dawson-Elli, and L. kun Tsui, “Impedance.py: A python package for electrochemical impedance analysis,” *Journal of Open Source Software*, vol. 5, no. 52, p. 2349, 2020.

[120] Q. Zhang *et al.*, “Energy Dispersive X-ray Diffraction (EDXRD) of Li1.1V3O8 Electrochemical Cell,” *MRS Advances*, vol. 2, no. 07, pp. 401–406, 2017.

[121] S. Jouanneau, A. Le Gal La Salle, A. Verbaere, M. Deschamps, S. Lascaud, and D. Guyomard, “Influence of the morphology on the Li insertion properties of Li1.1V3O8,” *Journal of Materials Chemistry*, vol. 13, no. 4, p. 921, 2003.

[122] J. Xie, J. Li, H. Zhan, and Y. Zhou, “Low-temperature sol–gel synthesis of Li1.2V3O8 from V2O5 gel,” *Materials Letters*, vol. 57, no. 18, pp. 2682–2687, May 2003.

[123] S. Y. Chew, C. Feng, S. H. Ng, J. Wang, Z. Guo, and H. Liu, “Low-Temperature Synthesis of Polypyrrole-Coated LiV[sub 3]O[sub 8] Composite with Enhanced Electrochemical Properties,” *Journal of The Electrochemical Society*, vol. 154, no. 7, A633, 2007.

[124] F. Tanguy, J. Gaubicher, and D. Guyomard, “Capacity fading on cycling nano size grains of Li1.1V3O8, electrochemical investigation,” *Electrochimica Acta*, vol. 55, no. 12, pp. 3979–3986, Apr. 2010.

[125] S. Sarkar, H. Banda, and S. Mitra, “High capacity lithium-ion battery cathode using LiV3O8 nanorods,” *Electrochimica Acta*, vol. 99, pp. 242–252, Jun. 2013.

[126] T. J. Patey *et al.*, “Electrochemistry of LiV[sub 3]O[sub 8] Nanoparticles Made by Flame Spray Pyrolysis,” *Electrochemical and Solid-State Letters*, vol. 11, no. 4, A46, 2008.

[127] H. Liu, Y. Wang, W. Yang, and H. Zhou, “A large capacity of LiV3O8 cathode material for rechargeable lithium-based batteries,” *Electrochimica Acta*, vol. 56, no. 3, pp. 1392–1398, Jan. 2011.

[128] X. Xu *et al.*, “Topotactically synthesized ultralong LiV3O8 nanowire cathode materials for high-rate and long-life rechargeable lithium batteries,” *NPG Asia Materials*, vol. 4, no. 6, e20–e20, Jun. 2012.

[129] A. H. McCarthy *et al.*, “Lithium vanadium oxide (Li $_{1.1}$ V $_{3}$ O $_{8}$) thick porous electrodes with high rate capacity: Utilization and evolution upon extended cycling elucidated *via operando* energy dispersive X-ray diffraction and continuum simulation,” *Physical Chemistry Chemical Physics*, 2020.

[130] Q. Zhang and R. E. White, “Capacity fade analysis of a lithium ion cell,” *Journal of Power Sources*, vol. 179, no. 2, pp. 793–798, May 2008.

[131] W. A. Appiah, M.-H. Ryou, and Y. M. Lee, "A Physics-Based Model Capacity Fade Analysis of LiMn $_2$ O $_4$ /Graphite Cell at Different Temperatures," *Journal of The Electrochemical Society*, vol. 166, no. 3, A5109–A5116, 2019.

[132] V. Ramadesigan, K. Chen, N. A. Burns, V. Boovaragavan, R. D. Braatz, and V. R. Subramanian, "Parameter Estimation and Capacity Fade Analysis of Lithium-Ion Batteries Using Reformulated Models," *Journal of The Electrochemical Society*, vol. 158, no. 9, A1048, 2011.

[133] J. Li *et al.*, "Aging modes analysis and physical parameter identification based on a simplified electrochemical model for lithium-ion batteries," *Journal of Energy Storage*, vol. 31, p. 101 538, Oct. 2020.

[134] R. Tibshirani, "Regression Shrinkage and Selection Via the Lasso," *Journal of the Royal Statistical Society: Series B (Methodological)*, vol. 58, no. 1, pp. 267–288, 1996.

[135] G. James, D. Witten, T. Hastie, and R. Tibshirani, *An Introduction to Statistical Learning: With Applications in R*, ser. Springer Texts in Statistics. New York: Springer-Verlag, 2013, ISBN: 978-1-4614-7137-0.

[136] H. Wang, Y.-I. Jang, B. Huang, D. R. Sadoway, and Y.-M. Chiang, "TEM Study of Electrochemical Cycling-Induced Damage and Disorder in LiCoO2 Cathodes for Rechargeable Lithium Batteries," *J. Electrochem. Soc.*, vol. 146, no. 2, pp. 473–480, Feb. 1999.

[137] Y. Itou and Y. Ukyo, "Performance of LiNiCoO2 materials for advanced lithium-ion batteries," *Journal of Power Sources*, vol. 146, no. 1-2, pp. 39–44, Aug. 2005.

[138] G. Chen, X. Song, and T. Richardson, "Electron Microscopy Study of the LiFePO[sub 4] to FePO[sub 4] Phase Transition," *Electrochemical and Solid State Letters - ELECTROCHEM SOLID STATE LETT*, vol. 9, Jun. 2006.

[139] R. Fu, S.-Y. Choe, V. Agubra, and J. Fergus, "Development of a physics-based degradation model for lithium ion polymer batteries considering side reactions," *Journal of Power Sources*, vol. 278, pp. 506–521, Mar. 2015.

[140] M. Dubarry, C. Truchot, and B. Y. Liaw, "Synthesize battery degradation modes via a diagnostic and prognostic model," *Journal of Power Sources*, vol. 219, pp. 204–216, Dec. 2012.

[141] P. Gasper, K. Gering, E. Dufek, and K. Smith, "Challenging Practices of Algebraic Battery Life Models through Statistical Validation and Model Identification via Machine-Learning," *J. Electrochem. Soc.*, vol. 168, no. 2, p. 020 502, Feb. 2021.

[142] Y. Li *et al.*, "Data-driven health estimation and lifetime prediction of lithium-ion batteries: A review," *Renewable and Sustainable Energy Reviews*, vol. 113, p. 109 254, Oct. 2019.

[143] Y. Li *et al.*, “Random forest regression for online capacity estimation of lithium-ion batteries,” *Applied Energy*, vol. 232, pp. 197–210, Dec. 2018.

[144] R. R. Richardson, C. R. Birkl, M. A. Osborne, and D. A. Howey, “Gaussian Process Regression for In Situ Capacity Estimation of Lithium-Ion Batteries,” *IEEE Transactions on Industrial Informatics*, vol. 15, no. 1, pp. 127–138, Jan. 2019.

[145] Y. Deng *et al.*, “Feature parameter extraction and intelligent estimation of the State-of-Health of lithium-ion batteries,” *Energy*, vol. 176, pp. 91–102, Jun. 2019.

[146] X. Hu, Y. Che, X. Lin, and S. Onori, “Battery health prediction using fusion-based feature selection and machine learning,” *IEEE Transactions on Transportation Electrification*, pp. 1–1, 2020.

[147] A. Ran *et al.*, “Data-Driven Fast Clustering of Second-Life Lithium-Ion Battery: Mechanism and Algorithm,” *Adv. Theory Simul.*, vol. 3, no. 8, p. 2 000 109, Aug. 2020.

[148] R. R. Richardson, M. A. Osborne, and D. A. Howey, “Gaussian process regression for forecasting battery state of health,” *Journal of Power Sources*, vol. 357, pp. 209–219, Jul. 2017.

[149] K. A. Severson *et al.*, “Data-driven prediction of battery cycle life before capacity degradation,” *Nature Energy*, Mar. 2019.

[150] P. Fermín-Cueto *et al.*, “Identification and machine learning prediction of knee-point and knee-onset in capacity degradation curves of lithium-ion cells,” *Energy and AI*, vol. 1, p. 100 006, Aug. 2020.

[151] V. Sulzer, P. Mohtat, S. Lee, J. B. Siegel, and A. G. Stefanopoulou, “Promise and Challenges of a Data-Driven Approach for Battery Lifetime Prognostics,” *arXiv:2010.07460 [cs, eess, stat]*, Oct. 2020. arXiv: `2010.07460 [cs, eess, stat]`.

[152] J. Hong, D. Lee, E.-R. Jeong, and Y. Yi, “Towards the swift prediction of the remaining useful life of lithium-ion batteries with end-to-end deep learning,” *Applied Energy*, vol. 278, p. 115 646, Nov. 2020.

[153] P. M. Attia, K. A. Severson, and J. D. Witmer, “Statistical learning for accurate and interpretable battery lifetime prediction,” *arXiv:2101.01885 [cond-mat, stat]*, Jan. 2021. arXiv: `2101.01885 [cond-mat, stat]`.

[154] M. Aykol *et al.*, “Perspective—Combining Physics and Machine Learning to Predict Battery Lifetime,” *J. Electrochem. Soc.*, vol. 168, no. 3, p. 030 525, Mar. 2021.

[155] M. Dubarry and D. Beck, “Big data training data for artificial intelligence-based Li-ion diagnosis and prognosis,” *Journal of Power Sources*, vol. 479, p. 228 806, Dec. 2020.

[156] M. Dubarry, *Graphite//LFP synthetic V vs. Q dataset (>700,000 unique curves)*, Mar. 2021.

[157] ——, *Graphite//NCA synthetic V vs. Q & duty cycle datasets*, Mar. 2021.

[158] ——, *Graphite// NMC synthetic V vs. Q & duty cycle datasets*, Mar. 2021.

[159] M. Dubarry and D. Beck, "Analysis of Synthetic Voltage vs. Capacity Datasets for Big Data Li-ion Diagnosis and Prognosis," *Energies*, p. 23, 2021.

[160] S. Lee and Y. Kim, "Li-ion Battery Electrode Health Diagnostics using Machine Learning," in *2020 American Control Conference (ACC)*, Jul. 2020, pp. 1137–1142.

[161] C. R. Birkl, M. R. Roberts, E. McTurk, P. G. Bruce, and D. A. Howey, "Degradation diagnostics for lithium ion cells," *Journal of Power Sources*, vol. 341, pp. 373–386, Feb. 2017.

[162] G. Ning, B. Haran, and B. N. Popov, "Capacity fade study of lithium-ion batteries cycled at high discharge rates," *Journal of Power Sources*, vol. 117, no. 1-2, pp. 160–169, May 2003.

[163] T. Waldmann *et al.*, "Review—Post-Mortem Analysis of Aged Lithium-Ion Batteries: Disassembly Methodology and Physico-Chemical Analysis Techniques," *Journal of The Electrochemical Society*, vol. 163, no. 10, A2149–A2164, 2016.

[164] Y. Preger *et al.*, "Degradation of Commercial Lithium-Ion Cells as a Function of Chemistry and Cycling Conditions," *Journal of The Electrochemical Society*, vol. 167, no. 12, p. 120 532, Sep. 2020.

[165] K. S. Mayilvahanan *et al.*, "Understanding Evolution of Lithium Trivanadate Cathodes During Cycling via Reformulated Physics-Based Models and Experiments," *J. Electrochem. Soc.*, vol. 168, no. 5, p. 050 525, May 2021.

[166] Y. Preger, *Degradation of Commercial Li-ion Cells Beyond 80% Capacity*, Sandia National Lab, Nov. 2019.

[167] X.-G. Yang, Y. Leng, G. Zhang, S. Ge, and C.-Y. Wang, "Modeling of lithium plating induced aging of lithium-ion batteries: Transition from linear to nonlinear aging," *Journal of Power Sources*, vol. 360, pp. 28–40, Aug. 2017.

[168] G. Baure and M. Dubarry, "Synthetic vs. Real Driving Cycles: A Comparison of Electric Vehicle Battery Degradation," *Batteries*, vol. 5, no. 2, p. 42, May 2019.

[169] P. Virtanen *et al.*, "SciPy 1.0: Fundamental Algorithms for Scientific Computing in Python," *Nature Methods*, vol. 17, pp. 261–272, 2020.

[170] M. Dubarry and B. Y. Liaw, "Identify capacity fading mechanism in a commercial LiFePO4 cell," *Journal of Power Sources*, vol. 194, no. 1, pp. 541–549, Oct. 2009.

[171] A. J. Smith, J. C. Burns, and J. R. Dahn, "High-Precision Differential Capacity Analysis of LiMn2O4/graphite Cells," *Electrochem. Solid-State Lett.*, vol. 14, no. 4, A39, 2011.

[172] E. Sarasketa-Zabala, F. Aguesse, I. Villarreal, L. M. Rodriguez-Martinez, C. M. López, and P. Kubiak, "Understanding Lithium Inventory Loss and Sudden Performance Fade in Cylindrical Cells during Cycling with Deep-Discharge Steps," *J. Phys. Chem. C*, vol. 119, no. 2, pp. 896–906, Jan. 2015.

[173] M. Berecibar, M. Dubarry, N. Omar, I. Villarreal, and J. Van Mierlo, "Degradation Mechanism Detection for NMC Batteries based on Incremental Capacity Curves," *WEVJ*, vol. 8, no. 2, pp. 350–361, Jun. 2016.

[174] D. Anseán *et al.*, "Lithium-Ion Battery Degradation Indicators Via Incremental Capacity Analysis," *IEEE Transactions on Industry Applications*, vol. 55, no. 3, pp. 2992–3002, May 2019.

[175] B. Pan *et al.*, "Aging mechanism diagnosis of lithium ion battery by open circuit voltage analysis," *Electrochimica Acta*, vol. 362, p. 137 101, Dec. 2020.

[176] I. Bloom *et al.*, "Differential voltage analyses of high-power, lithium-ion cells," *Journal of Power Sources*, vol. 139, no. 1-2, pp. 295–303, Jan. 2005.

[177] M. Safari and C. Delacourt, "Aging of a Commercial Graphite/LiFePO4 Cell," *J. Electrochem. Soc.*, vol. 158, no. 10, A1123, 2011.

[178] P. Keil *et al.*, "Calendar Aging of Lithium-Ion Batteries: I. Impact of the Graphite Anode on Capacity Fade," *Journal of The Electrochemical Society*, vol. 163, no. 9, A1872–A1880, 2016.

[179] M. Dubarry, M. Berecibar, A. Devie, D. Anseán, N. Omar, and I. Villarreal, "State of health battery estimator enabling degradation diagnosis: Model and algorithm description," *Journal of Power Sources*, vol. 360, pp. 59–69, Aug. 2017.

[180] F. Pedregosa *et al.*, "Scikit-learn: Machine Learning in Python," *MACHINE LEARNING IN PYTHON*, p. 6,

[181] C. Molnar, *Interpretable Machine Learning, A Guide for Making Black Box Models Explainable.* 2019, `https://christophm.github.io/interpretable-ml-book/`.

[182] S. Seabold and J. Perktold, "Statsmodels: Econometric and statistical modeling with python," in *9th Python in Science Conference*, 2010.

[183] W. M. Dose, C. Xu, C. P. Grey, and M. F. De Volder, "Effect of Anode Slippage on Cathode Cutoff Potential and Degradation Mechanisms in Ni-Rich Li-Ion Batteries," *Cell Reports Physical Science*, vol. 1, no. 11, p. 100 253, Nov. 2020.

[184] M. Berecibar, I. Gandiaga, I. Villarreal, N. Omar, J. Van Mierlo, and P. Van den Bossche, "Critical review of state of health estimation methods of Li-ion batteries for real applications," *Renewable and Sustainable Energy Reviews*, vol. 56, pp. 572–587, Apr. 2016.

[185] M. G. Boebinger, J. A. Lewis, S. E. Sandoval, and M. T. McDowell, "Understanding Transformations in Battery Materials Using in Situ and Operando Experiments: Progress and Outlook," *ACS Energy Lett.*, vol. 5, no. 1, pp. 335–345, Jan. 2020.

[186] C. D. Quilty *et al.*, "Impact of Charge Voltage on Factors Influencing Capacity Fade in Layered NMC622: Multimodal X-ray and Electrochemical Characterization," *ACS Appl. Mater. Interfaces*, vol. 13, no. 43, pp. 50 920–50 935, Nov. 2021.

[187] N. Dawson-Elli, S. B. Lee, M. Pathak, K. Mitra, and V. R. Subramanian, "Data Science Approaches for Electrochemical Engineers: An Introduction through Surrogate Model Development for Lithium-Ion Batteries," *Journal of The Electrochemical Society*, vol. 165, no. 2, A1–A15, 2018.

[188] N. Dawson-Elli, S. Kolluri, K. Mitra, and V. R. Subramanian, "On the Creation of a Chess-AI-Inspired Problem-Specific Optimizer for the Pseudo Two-Dimensional Battery Model Using Neural Networks," *Journal of The Electrochemical Society*, vol. 166, no. 6, A886–A896, 2019.

[189] M. Andersson *et al.*, "Parametrization of physics-based battery models from input–output data: A review of methodology and current research," *Journal of Power Sources*, vol. 521, p. 230 859, Feb. 2022.

[190] K. S. Mayilvahanan, K. J. Takeuchi, E. S. Takeuchi, A. C. Marschilok, and A. West, "Supervised Learning of Synthetic Big Data for Li-ion Battery Degradation Diagnosis," *Batteries & Supercaps*, batt.202100166, Aug. 2021.

[191] P. Virtanen *et al.*, "SciPy 1.0: Fundamental algorithms for scientific computing in Python," *Nat Methods*, vol. 17, no. 3, pp. 261–272, Mar. 2020.

[192] F. Chollet, *Deep Learning with Python*. Shelter Island, New York: Manning Publications Co, 2018, ISBN: 978-1-61729-443-3.

[193] F. Chollet *et al.*, *Keras*, `https://keras.io`, 2015.

[194] W. Li, B. Song, and A. Manthiram, "High-voltage positive electrode materials for lithium-ion batteries," *Chem. Soc. Rev.*, vol. 46, no. 10, pp. 3006–3059, 2017.

[195] I. Laresgoiti, S. Käbitz, M. Ecker, and D. U. Sauer, “Modeling mechanical degradation in lithium ion batteries during cycling: Solid electrolyte interphase fracture,” *Journal of Power Sources*, vol. 300, pp. 112–122, Dec. 2015.

[196] P. Barai, K. Smith, C.-F. Chen, G.-H. Kim, and P. P. Mukherjee, “Reduced Order Modeling of Mechanical Degradation Induced Performance Decay in Lithium-Ion Battery Porous Electrodes,” *J. Electrochem. Soc.*, vol. 162, no. 9, A1751–A1771, 2015.

[197] A. P. Schmidt, M. Bitzer, Á. W. Imre, and L. Guzzella, “Model-based distinction and quantification of capacity loss and rate capability fade in Li-ion batteries,” *Journal of Power Sources*, vol. 195, no. 22, pp. 7634–7638, Nov. 2010.

[198] R. Drummond and S. R. Duncan, “Structural Identifiability of a Pseudo-2D Li-ion Battery Electrochemical Model,” *IFAC-PapersOnLine*, vol. 53, no. 2, pp. 12 452–12 458, 2020.

[199] K. S. Mayilvahanan, J. R. Soni, K. J. Takeuchi, E. S. Takeuchi, A. C. Marschilok, and A. C. West, “Parameter Estimation for Electrode Degradation: Learning in the Face of Model-Experiment Discrepancies,” *J. Electrochem. Soc.*, vol. 169, no. 5, p. 050 517, May 2022.

[200] Y. Gal and Z. Ghahramani, *Dropout as a Bayesian Approximation: Representing Model Uncertainty in Deep Learning*, Oct. 2016. arXiv: `1506.02142 [cs, stat]`.

[201] V. Kuleshov, N. Fenner, and S. Ermon, “Accurate Uncertainties for Deep Learning Using Calibrated Regression,” *arXiv:1807.00263 [cs, stat]*, Jun. 2018. arXiv: `1807.00263 [cs, stat]`.